An investigation into the performance of Plasma and Laser coatings under rolling contact

By: Mark Gilpin

(2008)

Submitted in fulfilment of the academic requirements for the degree of Masters in Science and Engineering in the School of Mechanical Engineering at the University of KwaZulu-Natal

Abstract

Rolling contact is experienced by a large number of components in mechanical designs. Examples include roller bearings and ink distribution rollers in the printing industry. Rolling contact results in surface wear. It is however possible to reduce rolling contact wear rates and surface fatigue by performing a surface modification such as powdered metal coating [35]. Powder coating methods such as Laser cladding and Plasma coating are two application processes that are completely different in method and therefore create different coating microstructures and bonding mechanisms between the coating and substrate.

The aim of the research was to investigate the comparative rolling contact performance of two coating processes and two separate metal powder compositions. The coatings were applied to British standard En 9 steel test specimens. En 9 was selected due to its popular use in the manufacture of shafts, cylinders and rollers. Under rolling contact, material is removed from the surface as a result of wear and surface fatigue.

Through testing and evaluation, the performance of the coating application processes were evaluated relative to one another and relative to the uncoated steel under rolling contact. The performance of the coating compositions were also evaluated against one another for a given coating application process. Results used to determine the performance of the coatings and coating processes were, the number of cycles to failure and the wear rates of the coated surface. Microstructure pictures of the coated surface were taken prior to testing and following testing. The pictures were used to qualitatively determine the effects of the rolling contact on the surfaces.

Through the study of rolling contact, an explanation of the stresses induced in the contact area and the position of the maximum values were determined. The boundaries for the deformation regimes were identified through the understanding of the position of first yield and the shakedown limit under rolling contact. The theories of rolling contact fatigue are covered briefly as part of a better understanding of the failure mechanism however the experimentation is largely comparative based.

Acknowledgements

Table of contents

List of figures

List of symbols:

a	- Half the contact width
P	- Force per unit length
P_0	- Peak Hertz contact pressure
R_1	- Radius of curvature of body 1
R_2	- Radius of curvature of body 2
σ_x	- The stress in the x direction
σ_z	- The stress in the z direction
σ_y	- The stress in the y direction
τ_{zx}	- Shear stress zx (orthogonal shear stress)
τ_s	- Shear stress
E_1	- Young's modulus of elasticity for contacting body 1
E_2	- Young's modulus of elasticity for contacting body 2
υ_1	- Poisson's ratio for body 1
υ_2	- Poisson's ratio for body 2
R	- Relative curvature of the 2 contacting bodies
x	- Position of the element on the x axis
z	- Position of the element on the z axis
U_{X1}	- Circumferential velocity of cylinder 1 in the x direction
U_{X2}	- Circumferential velocity of cylinder 2 in the x direction
T	- Tangential traction
μ	- Coefficient of friction
U	- Linear velocity of the surface
μR	- Coefficient of rolling resistance
Po/k	- Load factor ratio / relative hertz contact stress
$\sigma_1, \sigma_2, \sigma_3$	- Principle stresses
k	- Yield stress in simple shear
Y	- Yield stress in tension or compression
$\rho xx, \rho yy$	- Residual stresses in the x and y directions
Rr	- Rolling resistance
L	- Applied load (N)
g	- Gravitational acceleration

Synopsis

The aim and scope of the research was to investigate the rolling contact performance of two coating processes and two separate powder compositions applied to British standard En 9 steel. En 9 test specimens were manufactured and coated using both laser and plasma coating methods. Two different powdered metal compositions were used for each of the coating processes. Rolling contact fatigue tests were performed to obtain comparative results between the coated and un-coated test specimens and between the coating compositions for a given coating process. The tests were conducted under non-lubricated 2 dimensional pure rolling contact conditions, at various Hertz contact stresses. The contact stresses under which the tests were conducted were approximately 300MPa, 500MPa, 700MPa and 900MPa. The resulting relative Hertz contact stress or load factor ratios were then 1.5, 2.5, 3.5 and 4.5 respectively. The En 9 specimens were tested within three deformation regimes, while the coated test specimen were tested within two of these regimes. The three deformation regimes in order of stress magnitude were; elastic material response, elastic material shakedown and plastic/ratchetting material response. A total of 12 coated and uncoated specimens were tested under rolling contact.

All the rolling contact fatigue tests conducted in the research were performed using a specifically designed and manufactured test machine. The effect of the increase in contact stress affected all the tested specimens. Differences between specimens wear rates, surface hardness, contact width and failure modes were observed.

The plasma coated specimens did not perform significantly compared with either the En 9 benchmark specimens of the laser clad samples for the tested conditions. However; Laser cladding offered greater wear resistance compared to the benchmark En 9 specimens for the same tested contact stress. Furthermore; specimens laser clad with composition 2 showed less overall wear (change in diameter) than specimens coated with composition 1. Specimens coated with composition 2 however showed visible porosity after cladding compared to specimens coated with composition 1. The visible porosity of the specimens coated using composition 2 may be illuminated by adjusting the process parameters in future research into the laser cladding process.

It is concluded that, Laser cladding is a more suitable surface modification method than plasma coating for En9 under rolling contact conditions. Furthermore, of the 2 compositions tested, composition 2 offered greater wear resistance to En 9 under rolling contact.

1. Introduction

Almost all mechanical machines that have parts moving against one another, experience wear in some form or other. This is a phenomenon that has seen much study and much investment in terms of prolonging component life. A few examples of elastic bodies in contact can be found in the contact between the following components: gears in mesh, rolling ball bearings, contacting rollers, cams and followers and railway wheels on rails [15], [1]. Due to the limited area of contact, stresses are generated within each of the contacting bodies. As the contact stresses are cycled during rolling contact the stresses play a significant role in surface failures. Pitting and spalling are both examples of such surface fatigue failures [1]. One method of altering wear and surface fatigue characteristics is the application of a surface coating. A coating may be re-applied several times during the life of the component and is usually a much cheaper option than total component replacement. The following research is an investigation into the performance of both plasma and laser coatings under non lubricated rolling contact.

Laser cladding and plasma spraying are both surface coating methods. The processes use powdered metal with the addition of heat to form a surface coating. However the application methods are distinctly different and as a result produce different coating properties. The differences are that of bonding mechanism and coating microstructure. Plasma spraying is a thermal spray application method while laser cladding is a fusion or welding process. As a result laser cladding creates a metallurgical bond between coating and substrate while plasma spraying produces a mechanical bond.

The effect of both wear and corrosion may be decreased by the addition of a plasma sprayed surface. The surface may also present sought-after thermal or electrical properties. Dimensional control and surface restoration may also be achieved [59]. The number of applications into which modified surfaces may prove useful are varied and numerous both in contact and non-contact applications.

The plasma spray process generates a coating using molten material. Powdered material is injected through a plasma flame where it is melted and accelerated towards the components surface. As the molten material contacts the surface it swiftly cools and solidifies forming a coated layer. The process is referred to as "cold" as the temperature of the substrate is cool in comparison to the coating material. The relatively cool temperatures maintained during coating prevent distortion and metallurgical changes of the substrate [62].

Laser cladding, in contrast to plasma coating uses substantial heat and energy to metallurgically fuse an alloy to a substrate, the transfer of heat is rapid and localized to one specific area on a surface at any one time [65]. The energy and heat required is generated using a LASER, the definition of which is a **L**ight **A**mplification by **S**timulated **E**mission of **R**adiation [66]. A detailed discussion of each coating process (Laser and plasma) is presented in chapter 8.

Each of the coating methods have a wide variety of coating parameters which can vary. General variable processes parameters are; the composition of the substrate, powder composition and characteristics, feed rate of the powdered metal, application speed, component manipulation and gas flow rates. More specific process parameters for plasma spraying are, heat generated in the plasma gun and application distance [60]. While for laser cladding, beam energy and powder application method are significant [61]. As a result of the large variation of parameters for both application methods, the optimization of either plasma coating or laser cladding for any specific application can be viewed as a research field in itself. However, for consistency in the current research, the process parameters for each of the application methods (plasma and laser) are to be kept the same for each of the compositions used.

Two dimensional line contact is experienced in the contact between cylindrical bodies. Following the interfacial defection of the cylinders, the contact area formed is rectangular in shape. Material within the contact region is deformed as a result of the deflection, Complex stresses are formed within the deformed material [11]. The magnitude of the stresses will vary depending on the elemental position within the contact region. These stresses at any point in the contact region can be calculated as a system of complex stresses applied to an element at that point. Due to the significance of the contact stresses to the present research, a detailed explanation of the stress distribution (position and magnitude) and resulting deformation regimes are discussed [9].

As a brief introduction; the material within the contact region responds differently under increased contact loading. The material response is dependent on the material property (k) and the applied Hertz contact stress (Po). The load factor or relative Hertz contact pressure (Po/k) can then be calculated for any specific rolling contact condition. The magnitude of the ratio will determine the response of the material in the contact region. Material response under rolling contact has been divided into four deformation regimes. The four contact deformation regimes (material responses) are as follows: elastic material response, elastic material shakedown, plastic shakedown and rachetting [21]. The restrictive load factor (Po/k) for elastic material response is identified as the elastic limit (Po/k = 3.1), while the limiting load factor for the material shakedown is the shakedown limit (Po/k = 4). As most of the testing in the present

2

research is to be conducted within the elastic and elastic shakedown deformation regimes, a detailed discussion and of both are explained [9].

For coated surfaces the microstructure, bonding mechanism, coating thickness and differences in mechanical properties affect the contact stresses predicted by Hertz contact stress theory [47]. However most published research and experimentation conducted for coated rolling contact either neglects the effect or predict only small differences through calculation. It is assumed therefore in the present research, that the calculated stresses are the same for both coated and uncoated test specimens.

The Hertz contact stress analysis is theoretical and for actual contact applications does not calculate the variation of stress at the edges of contact. Due to the finite length of actual contacting cylinders stress concentration occur at the edges. The contact stresses calculate using Hertz theory determine the stress accurately over the majority of the contacting length however not at the edges [9]. The magnitude of edges deformation of the test specimens is also to be investigated.

Under rolling contact conditions, contacting surfaces experience wear. Wear may be defined in one of two ways; "The progressive loss of substance from the surface of a body brought on by mechanical action, or the destruction of material produced as a result of repeated disturbances of the frictional bonds [17]". Rolling contact is a detailed field of study and the material behavior and wear mechanisms are complex. The quantity and types of wear are determined by the specific rolling contact conditions. Due to the variable nature of the conditions and material responses, calculation and prediction of wear is difficult. However an overview of rolling contact literature indicates that three main types of wear are predominant: Adhesive, abrasive and fatigue [44],[31].

Under pure/free rolling contact the predominant wear mechanism is fatigue. Fatigue is a result of contact stress formed between rolling bodies in contact. Fatigue operates on both a macroscopic and microscopic scale, resulting in surface wear on both scales [52].

Pitting and spalling are both identifying characteristics of microscopic fatigue failures. The failures are the result of Hertz contact stress acting on surface and subsurface layers of contacting bodies. Microscopic fatigue wear on the other hand is characterized by considerably smaller wear particles, formed as a result of contact stresses fatiguing and fracturing surface asperities [52]. Any defects present in any of the coated specimen will experience cyclic contact stress and be subject to fatigue and crack propagation which may lead to failure of a coating.

3

Microscopic fatigue results in surface wear and changes in specimen diameter during testing and can be measured.

A free or pure rolling condition is defined as rolling without shear surface tractions [19], however in actual applications of rolling contact, resistance to rolling motion is experienced. As the contact stresses are responsible for wear and surface fatigue, the magnitude of the rolling resistance affects the surface wear rates [52]. Testing in the present research is conducted under free rolling contact conditions. Measurements are to be taken during testing to confirm that a free rolling contact condition is maintained.

The aim and scope of the research is to investigate the rolling contact performance of two coating processes and two separate powder compositions applied to British standard En 9 steel. En 9 test specimens will be manufactured and coated using laser and plasma coating methods. Two different powdered metal compositions will be used for each of the coating processes. And, rolling contact fatigue tests will then performed to obtain comparative results between the coated and uncoated test specimens and between the coating compositions for a given coating process. The tests will be conducted under non-lubricated 2 dimensional pure rolling contact conditions, at various contact stresses. The contact stresses under which the tests are to be conducted are approximately 300MPa, 500MPa, 700MPa and 900MPa. The contact stresses under investigation fall within three of the deformation regimes.

Four En 9 test specimens or bench mark specimens are to be tested at approximate Hertz contact stresses of 300, 500, 700 and 900MPa respectively. The En 9 substrate is tested first to create a benchmark for the coated specimens to be tested against. Four specimens are to be coated using each of the application processes, two specimens with metal powder composition 1 and two with composition 2. The coated specimens will then be tested under similar hertz contact stresses to that of the uncoated specimens.

The plasma coated test specimens will be tested at Hertz contact stresses of 300MPa and 500MPa, while the laser clad specimens are to be tested at 500MPa and 700MPa. Both separate powdered metal compositions will then be tested at these stress levels for each of the coating application methods. The common contact stress between the laser and plasma tests is therefore 500MPa. The plasma tests specimens are tested at a slightly lower contact stress of 300MPa as the bonding mechanism between coating and substrate is mechanical in nature and is suspected to be less durable than the laser clad test specimens tested at 700MPa.

The testing of the uncoated and coated tests specimens at a contact stress of 500MPa results in an overlapping rolling contact conditions which allows for direct performance comparisons to be made. No coated test specimens are to be tested at 900MPa contact stress, only one En 9 specimen is to be tested at this stress to observe the effect of the high contact stress on the specimen. This particular specimen is to be tested in the ratchetting and plastic deformation regime.

During testing, changes in diameter of the test specimens will be measured to determine the rate of surface wear (graphs of wear rate will be plotted). Prior to and following testing, the contact width of the test specimen is measured to observe the effect of the increase in the contact stress at the edges of contact. The measurements are to be taken for all test specimens and form the basis for a comparative performance between test specimens coated and uncoated. Following testing, the coating microstructure will be examined to observe the effect of the rolling contact.

2. Three Dimensional Elliptical contact
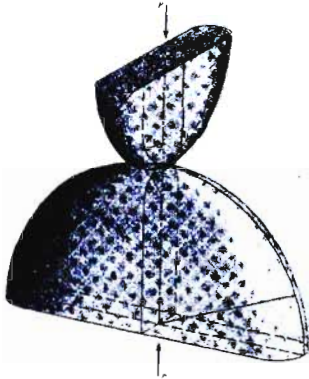
Figure 2. 1 Two curved surfaces of different radii in contact

A few examples of elastic bodies in contact can be found in the contact between the following components: gears in mesh, rolling ball bearings, contacting rollers, cams and followers and railway wheels on rails [15], [1]. Due to the limited area of contact, stresses are generated within each of the contacting bodies. As the contact stresses are cycled during rolling contact the stresses play a significant role in surface failures. Pitting and spalling are both examples of such surface fatigue failures [1].

Three dimensional or elliptical contact is the general contact case. The contact is formed when two bodies each having two principle radii of curvature (toroids) are brought into contact. As a result of the contact an area of contact and stresses are created. Early researchers derived mathematical equations to determine both the area of contact and the stresses generated. Later experiments were conducted to highlight the accuracy of the mathematical derivations [2].

Elliptical contact is beyond the scope of the research as the testing and experimentation is conducted under line contact (2 dimensional contact). However the equations for line contact are derived as a limiting condition of the elliptical contact case.

In the late nineteenth century, Hertz conducted an analysis of contact between elastic bodies. The published papers formed the beginnings of later contact stress analysis. The contact analyzed was that of three dimensional or elliptical contact in which mathematical equations were derived for both the general contact shape and stresses generated [9],[2].

A number of assumptions are made about the contact. The assumptions are as follows [1],[9]:

6

- The contacting bodies are both elastic and nonconforming. Nonconforming meaning that on initial contact, prior to deformation the surfaces will first contact on either a point or a line.
- The surfaces of the contacting bodies have no surface roughness and no tangential traction is present during contact.
- The contact area is elliptical in shape and the size of the area is significantly smaller in comparison with the size of the contacting bodies.
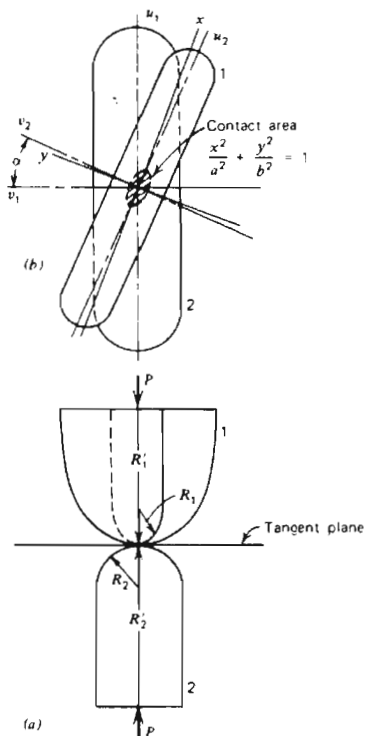
Figure 2. 2 The area of contact formed under elliptical contact [1]

Figure 2.2 illustrates the top and side view of a nonconforming elliptical contact. The two principle radii of curvature for each of the contacting bodies are shown in Figure 2.2 (a). The radii of curvature of body 1 and 2 are identified as R_1 R'_1 and R_2 R'_2 respectively. The tangential plane is the interface at which the surfaces of both bodies deform flat against one another. Figure 2.2 (b) illustrates; the plan sections about which the contacting bodies are curved and the elliptical contact area. The lines v1 and u1 are the plane sections which contain the radii of curvature $(R_1 R'_1)$ for body one. Lines v2 and u2 represent the same for body 2. The angle between two of the plane sections v1 and v2 containing one of the radii of curvature for each of the contact bodies is denoted by α. The area of contact is assumed to be elliptical in shape having a semi minor axis y and a semi major axis x [1].

7

It is from the aforementioned assumptions and geometric considerations of the contact that the contacting stresses were mathematically determined. Following the initial observations by Hertz a substantial amount of research into the stress distribution within the contact region continued [1]. While the general solution for contact stresses obtained by Hertz were expressed in terms of Newtonian potential functions, in 1930 researches Thomas and Hoersch converted the equations into expressions containing standard elliptical integrals. The limitations of the equations were that only the stresses falling along the axis of symmetry could be calculated [2]. Solutions for elliptical integrals may be found in most mathematical text books [3].

It was only later in 1953 that equations for the stress distribution and magnitude anywhere in the contact region could be determined. These equations derived by Smith and Liu combined the effect of both normal and tangential forces on the contact stresses generated and further indicated that the largest variation of shear stress may not occur on the axis of symmetry [2]. As the range of shear stress is believed to be responsible for rolling contact fatigue the observation was significant [1]. Text by A.P Borosi and O.M Sidebottom (1985) [1] describe the equations derived by both Thomas and Hoersch (1930) and Smith and Liu (1953) for the determination of contact stresses.

A widespread application of three dimensional contact is found in the railway industry. The contact is that of wheel on rail. J.J Kalker (1991) [4] examined rolling contact theory over the preceding 60 years and highlighted the significance of Hertz theory in predicting both the size and shape of the contact area formed.

In 1997 J.A Greenwood [5] compared three approximate methods for deriving the area of contact generated in elliptical contact and concluded that very little difference in results was observed. This indicated the accuracy of Hertz and other researchers' work in contact analysis.

H. Fessler and E. Ollerton, (1957) [2] conducted experiments on toroids. The contact area and resulting stresses on the plane of symmetry were measured and calculated. In addition to the size and shape of the shape of the measured contact area been equal to that predicted by Hertz theory the magnitude and position of the maximum shear stress predicted by Thomas and Hoersch (1930) was also verified [2].

As a result of the increase in the technology in the field ultrasonic testing, the area of contact has been measured [6],[7]. Research by M. Pau, F. Aymerich, F. Ginesu (2002) [6] using ultrasonic wave reflection, tested a railway wheel and rail specimen and noted the accuracy to which the results agreed with the Hertz theory for the prediction of the contact size and shape. Further research using ultrasound was conducted by M.B. Marshall, R. Lewis, R.S. Dwyer-

Joyce, O. Olofsson [7]. It was noted that a small degree of fragmentation in the ultrasound image was due to surface roughness of the specimens. The surface roughness resulted in a higher measurement of the Hertz contact pressure, while the size and shape of the contact area was in good agreement with that calculated by Hertz theory [7]. Figure 2.3 illustrates the ultrasound images obtained in the research.
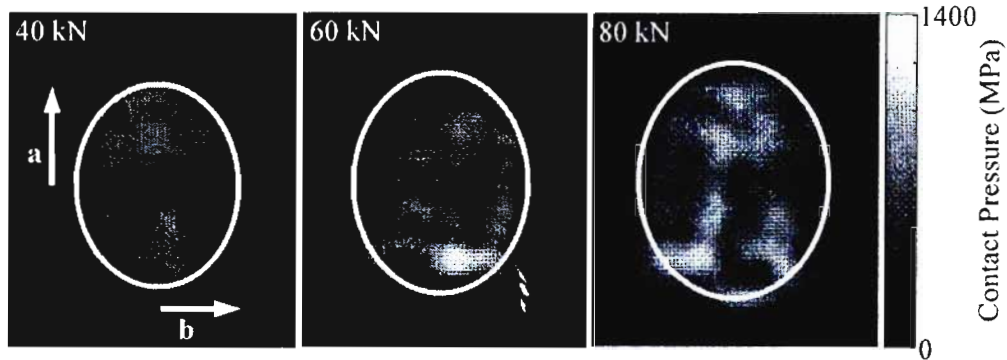
Figure 2. 3 Wheel and rail contact pressure maps [7]

The white outer ring represents the predicted elastic contact patch calculated using equations derived by Hertz. The white areas represent surface contact resulting in contact pressure. The small degree of fragmentation of the contact pressure is due to an initial surface roughness [7]. A. Kapoor, F.J Franklin, S.K Wong and M. Ishida (2002) [8] in a numerical analysis of rail wheel contact also showed that roughness caused the magnitude of contact pressure to deviate from that calculated by Hertz.

9

3. Two Dimensional Line contact

The contact between cylinders is referred to as line or two dimensional contact. Each cylinder has only one principle radius of curvature, while the principle radii for both cylinders fall within the same plane. As the cylinders are brought into contact and deflect the shape of the contacting interface is rectangular [9]. The analysis of two dimensional contact involves the calculation of the size of the contact area and the contact stresses generated as a result.

Two dimensional contact has been theoretically analysed and equations for stress distribution and magnitude have been derived in two ways.

A derivation published in text by A. P. Boresi & O. M Sidebottom [1] highlights the fact that two dimensional contact is a limiting case of three dimensional contact. Referring to Figure 2.2 (b). If the angle between two of the section plans (v_2, v_1) containing the radii of curvature R1 and R2 is set to 0 (α =0) and the values of R1 and R2 tend towards infinity (∞), the resulting geometry is that of the two dimensional case. The equations formed in this derivation are for the three dimensional case [1]. However using the above mentioned geometrical considerations the stress equations for the three dimensional contact yield values for the two dimensional case. A derivation published in text by K.L Johnson derives the equations directly from the recognition of the two dimensional nature of the problem [9].

The derivations and resulting equations for the contact stresses appear different in both the texts. However both sets of equations yield the same values after calculation. Plots of stress distribution and magnitude can be made using both sets of equations, the maximum values can also be calculated. While the two derivations were examined to gain a fuller understanding of the contact stresses, the equations presented in this section are those published in text by K.L Johnson [9].

Testing and experimentation in the present research conducted involves rolling 2 dimensional contact. Presented here is an explanation of the notation and equations used in the calculations of the complex contact stresses and distribution within the contact region.

3.1 Notation for line contact

The following notation defines the geometrical conditions and calculated values for line contact. The notation is standardized in a number of published texts [9],[10].

a	= Half the contact width
P	= Force per unit length
P_0	= Hertz contact stress at the center of contact
R_1	= Radius of curvature of body 1
R_2	= Radius of curvature of body 2

The standard Cartesian system of axes is used.

Figure 3.1 is a graphical representation of the contact between cylinders. The figure illustrates the geometric variables as well as the Cartesian coordinate system used for two dimensional contact [10].
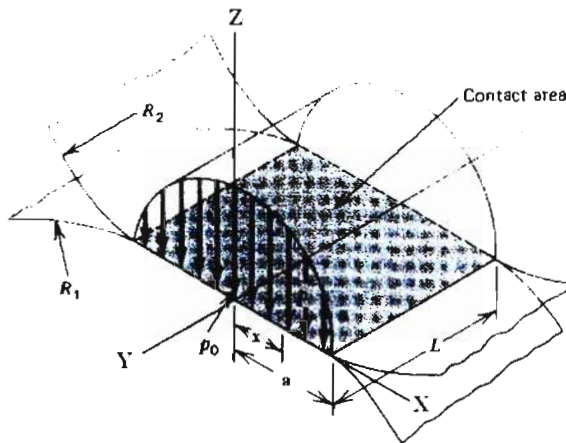
Figure 3. 1 Contact of parallel cylinders [10]

3.2 Contact stresses

Two dimensional line contact is experienced in the contact between cylindrical bodies. Following the interfacial defection of the cylinders the contact area formed is rectangular in shape. Material within the contact region is deformed as a result of this deflection. The material deformation results in the generation of complex stresses. The stress magnitudes vary throughout the contact region. The stress at any point in the contact region can be written as a system of complex stresses applied to an element at that point [11].
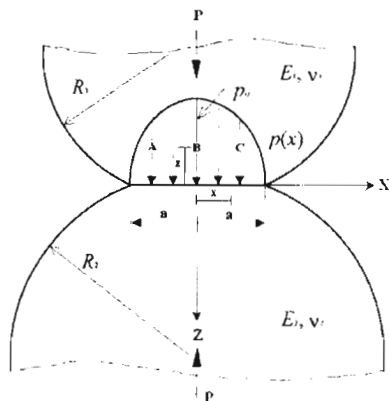
Figure 3. 2 Contact of parallel cylinders [11]

11

Figures 3.1 and 3.2 illustrate the notation used in the line contact (2 dimensional contact). The Elemental positions within the contact region are defined in terms of the ratio x/a for position in the X direction and z/a for position in the Z direction. The X axis is parallel to the contact interface while the Z axis is perpendicular. The letter 'a' is identified as half the contact width [9].

Three elemental positions within the contact region are represented in the diagram by A, B, C. Position B is in the centre of the contact region with A and C on either side. At each position the system of complex stresses applied to that element are represented in the three figures that follow. The magnitudes of the stresses vary with the depth within the contact region [11],[1],[9].

σ_x = The stress in the x direction

σ_z = The stress in the z direction

σ_y = The stress in the y direction

τ_{zx} = Shear stress zx (orthogonal shear stress)

τ_s = Shear stress

E_1, E_2 = Young's modulus of elasticity for body 1 and 2 respectively

υ_1, υ_2 = Poisson's ratio for body 1 and 2 respectively
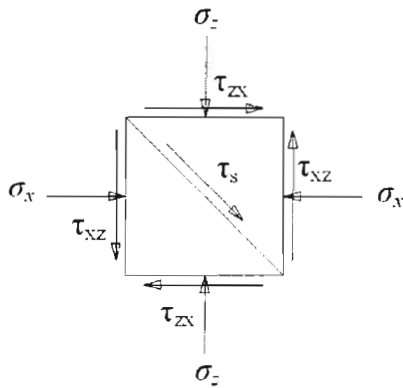
Figure 3. 3 Element stress at position A
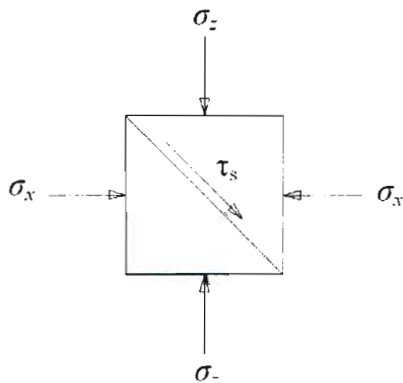
Figure 3. 4 Element stress at position B
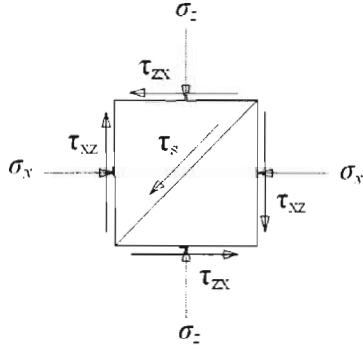
Figure 3. 5 Element stress at position C

With reference to the three previous figures, it is important to note that the orthogonal shear stress (τ_{zx}) has a change in direction in comparing position A and C [9]. This is of significance under rolling contact as this change in direction affects fatigue of the subsurface. It is also noted that the orthogonal stress is not present on the elements in the centre of contact [1] [9].

3.3 Contact stress distribution

The equations presented here were referenced from text by K.L Johnson [9]. The equations were later used in the mathematical modeling of the complex stresses in contact. The equations calculate the values for peak hertz contact pressure, relative curvature of the 2 contacting bodies, half the contact width and a combined elastic modulus for the contacting bodies. The equations for the calculation of the complex stress magnitudes at any point within the contact region are also present [9].

$$E^* = \left[\left(\frac{1 - v_1^2}{E_1} \right) + \left(\frac{1 - v_2^2}{E_2} \right) \right]^{-1} \qquad (1)$$

R = Relative curvature of the 2 contacting bodies

$$R = \left(\frac{1}{R_1} + \frac{1}{R_2} \right)^{-1} \qquad (2)$$

a = Half the contact width

$$a = \sqrt{\frac{4PR}{\pi E^*}} \qquad (3)$$

P_0 = Hertz contact stress at the center of contact

13

$$P_0 = \left(\frac{PE^*}{\pi R}\right)^{\frac{1}{2}} \tag{4}$$

The following equations calculate the stresses experienced at the center of the contact region (x/a = 0). Values for the stresses can be obtained by varying the value of z [9].

$$\sigma_x = -\frac{P_o}{a}\left\{(a^2 + 2z^2)(a^2 + z^2)^{-1/2} - 2z\right\} \tag{5}$$

$$\sigma_z = -\frac{P_o}{a}(a^2 + z^2)^{-1/2} \tag{6}$$

$$\tau_s = -\frac{P_0}{a}\{z - z^2(a^2 + z^2)^{-1/2}\} \tag{7}$$

Due to plane strain conditions experienced in the 2 dimensional contact case, the stresses in the x and z directions are not dependent on Poission's ratio. However the third principle stress and the stress in the y direction is given by [9]:

$$\sigma_3 = \sigma_y = v(\sigma_x + \sigma_z) \tag{8}$$

Expressions for the stress magnitudes at any point (x,z) within the contact region can be expressed in terms of m and n [9].

Where:

x   = Position of the element on the x axis (see Figure 3.2)

z   = Position of the element on the z axis (see Figure 3.2)

$$m^2 = \tfrac{1}{2}[\{(a^2 - x^2 + z^2)^2 + 4x^2z^2\}^{1/2} + (a^2 - x^2 + z^2)] \tag{9}$$

$$n^2 = \tfrac{1}{2}[\{(a^2 - x^2 + z^2)^2 + 4x^2z^2\}^{1/2} - (a^2 - x^2 + z^2)] \tag{10}$$

$$\sigma_x = -\frac{P_0}{a}\{m(1 + \frac{z^2 + n^2}{m^2 + n^2}) - 2z\} \tag{11}$$

$$\sigma_z = -\frac{P_0}{a}m(1 - \frac{z^2 + n^2}{m^2 + n^2}) \tag{12}$$

$$\tau_{zx} = -\frac{P_0}{a} n \left(\frac{m^2 - z^2}{m^2 + n^2} \right) \tag{13}$$

The variable stress in the y direction is given by equation 8. It is noted that the stress in the y direction varies with changes in both the stresses in the x and z directions [9].

4. Contact stress modeling

Using a mathematical program Matlab 7.4 a program was written (m.file) to plot the stress distribution and magnitude within the contact region. The equations (1-4 and 9-13) were used [9]. The program allowed for the stress at any depth and position within the contact region to be determined. The stresses can be calculated at any depth (z/a ratio) through the width of the contact. This is achieved by setting a value for z/a and applying a range of input values for x/a. The opposite can be achieved for the values of stresses at a distance from the centre of contact by setting a value of x/a and setting a range of values for z/a. The program (m.file) created is attached in the Appendix A

The aim was to gain a visual concept and better understanding of the stress distribution and to determine the maximum values for the stresses σ_y, σ_x, σ_z, τzx. .The values for half the contact width (a), the peak Hertz contact pressure (Po) and the relative radius of curvature (R) are also calculated [9]. The testing of specimens in the current research was conducted under different contact loads (P) and different contact lengths (L) (specimen widths). As a result the value of the contact width (a) and peak Hertz contact pressure (Po) varied with each specimen. The program calculated the values and the stresses for each individual specimen removing the need for continuous hand calculations.

Testing was conducted within two deformation regimes. The regimes were elastic and elastic plastic material responses. The limit of the elastic regime is given by the elastic limit while the limit for the elastic plastic regime is given by the Shakedown limit [9].

The elastic limit and the shakedown limit are discussed and explained in full detail in later chapters. However a general overview is presented here. The elastic limit and shakedown limit are defined in terms of Po/k ratios. Po is the peak hertz contact and k is the yield stress in simple shear for a given material. The elastic limit of Po/k ratio is 3.1 and the shakedown limit is at a Po/k ratio of 4. The position within the contact region at which the elastic limit and shakedown limit is reached is also derived and explained with the use of the equations 9-13 [9].

For the analysis of the elastic limit the equations 9-13 were substituted into equations for principle stresses. The principle stress equations were then substituted into two theories of failure [9]. Discussions of both the principle stresses and the theories of failure are presented in Chapter 6.2.4.1 and 6.2.4.2 respectively. Using the m.file created, the principle stresses and the theories of failure could be plotted and visually evaluated. The result was then used to verify the

elastic limit ratio to be Po/k 3.1 and to identify the position within the contact region at which yielding first occurs. A full description of the derivation for the elastic limit is covered in a later section.

An explanation and derivation of the shakedown limit was also conducted using the principle stress equations with the addition of residual stresses. The m.file was used to plot a graph for the discussion of the shakedown limit in rolling contact [22].

The following graph of the stress distribution at the centre of contact and at varying depths below the surface was plotted using the equations 9-13 as inputs into the program (m.file). The value of x/a was set to 0 and a range of values was set for the depth below the surface (z/a) [9].
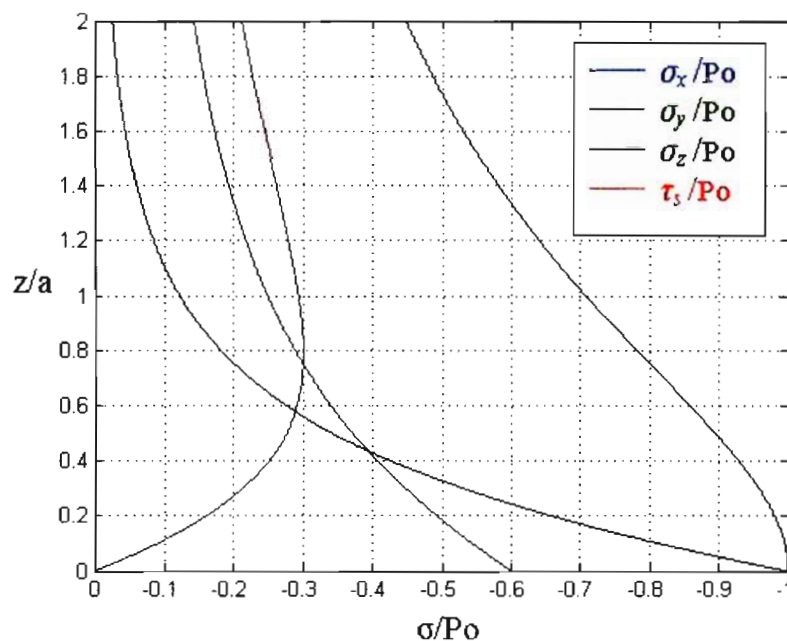
Figure 4. 1 Subsurface stress distribution along the axis of symmetry (x/a=0)

The vertical axis represents the depth below the surface as a ratio of the distance (z) divided by half the contact width (a). The horizontal axis is the stress (σ) divided by the Peak Hertz contact pressure (Po). The stress on an element (σ /Po), at depth and in any direction (x,y,z) maybe calculated using the theoretical plot in Figure 4.1. The shear stress τzx at (x/a =0) is equal to zero [9].

With reference to Figure 4.1 the maximum value of shear stress (τ_s) is found to be at a depth of 0.7861 z/a below the surface. The value of the stress is 30 % of the Hertz contact stress [1]. Other theoretical equations derived from the three dimensional contact case yield identical values for the position and magnitude of shear stress.

17

The distribution of shear stress for a cylindrical body contacting on a flat surface can be seen in the Photo-elastic fringe patterns in Figure 4.2. The lines in the pattern represent regions of constant shear stress (τ_s) [13].The maximum value of shear stress occurs at the centre of the contact region below the surface. The position (depth below the surface) of maximum shear stress (Red curve) can be seen in Figure 4.1, which is approximately 0.79a.
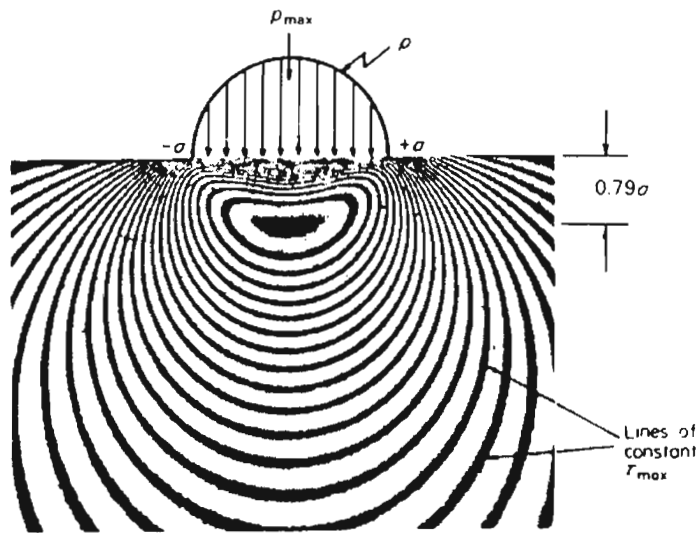
Figure 4. 2 Photo-elastic fringe pattern of contacting cylinders [13]

5. Contact of finite length cylindrical bodies

The Hertz contact stress analysis is theoretical and for actual contact applications does not calculate the variation of stress at the edges of contact. Due to the finite length of actual contacting cylinders stress concentration occur at the edges. The contact stresses calculate using Hertz theory determine the stress accurately over the majority of the contacting length however not at the edges [9]. Text by K.L Johnson [9] explains three cases of stress concentration effects experienced by contacting cylinders. Presented is the case applicable to the research conducted.
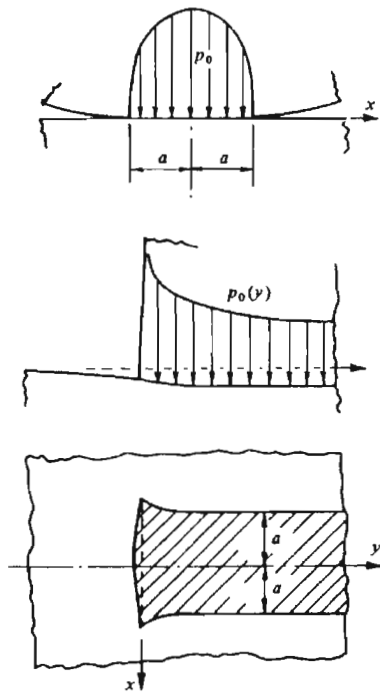
Figure 5. 1 Contact between cylinders of finite length [9]

This is the case of one cylindrical body rolling on another with one of the cylinders having a greater length. The result of this contact is that the cylinder having a shorter length experiences an increase in the hertz contact pressure at the edges of contact. The contact condition is shown in Figure 5.1 [9]. If the Hertz contact stress is significantly high, the material at the edge of the shorter cylinder will yield and a small amount of plastic deformation will be observed [14]. The result of the plastic deformation has the effect of increasing the area of contact. The stress concentration can be reduced with the addition of a rounded or barreled edge applied to the shorter cylinder [9].

The effects of the increased contact stress under rolling contact were observed in wear experiments conducted by W.R Tyfour, J.H Beynon and A Kapoor (1995) [14]. The

experiments showed a loss in diameter of the test specimen and an increase in contact width due to the effect of plastic deformation at the edges of contact. It was stated that although the increase in contact length did not affect the calculated contact stress as the increased area formed did support the applied load [14]. The Figure 5.2 illustrates the geometrical changes of the test specimen used in the testing.
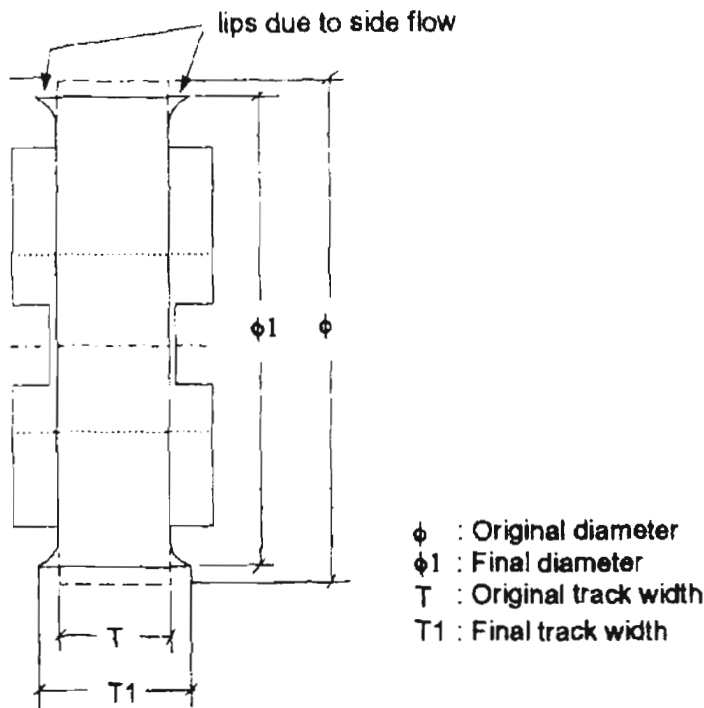
Figure 5. 2 Plastic flow at the edges of contact [14]

The observation made in the experimentation is of significance to the current research conducted as it was noted that the increase in the contact area has a minimal influence on the stress distribution within the contact region [14]. This is an important point to be noted as the tests conducted in the presented research were conducted under 2 dimensional rolling contact conditions.

Due to the design of the test machine the test specimens were of a shorter length than the surface on which rolling was observed. The ends of the test specimen were perpendicular to the contacting surface and no rounded edges were machined to reduce the stress concentration.

The test specimens tested in the presented research showed an increase in contact length. However as mentioned previously the effect of the increase in contact length has a limited effect on the value of contact stress predicted by Hertz contact stress theory.

6. Two dimensional rolling contact
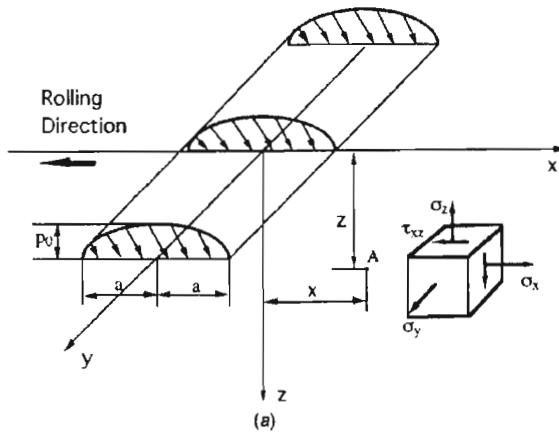
Figure 6. 1 Stress distribution on a subsurface element under rolling contact [15]

The testing and experimentation presented in the current research has been preformed under 2 dimensional rolling contact conditions. The tests were conducted under near perfect rolling conditions and within two deformation regimes. Presented here is a discussion and explanation of the effect of rolling resistance, the contact stresses generated and the deformation regimes experienced under rolling contact.

In the previous text the static contact of cylindrical bodies was discussed. The magnitude and distribution of the contact stresses were explained. The present chapter examines the effect of rolling contact on the stresses for cylinders in contact. Within the elastic contact regime the stresses within the contact region are equal in magnitude to the stresses derived for the static contact case (see Chapter 3). However; if the load is increased the magnitudes of the stresses within the contact region are amplified. As a result of the larger stresses, material within the contact region yields. The quantity of stress at which this occurs is identified as the elastic limit. If additional force is applied to the contacting cylinders increasing the contact stresses beyond the elastic limit, material within the contact region will experience elastic shakedown. At this point the material will plastically deformed and the contact stressed region will no longer behave elastically, however the material will build up residual stresses and the deformation will be elastic after an initial number of rolling cycles. This process is defined as elastic material shakedown. If the force is further increased the material in the contact region will cease to experience elastic shakedown, the magnitude of stress at which this occurs is referred to as the shakedown limit [9].

21

The testing was conducted within the elastic and elastic shakedown deformation regimes. The limits of the elastic and elastic shakedown material responses are the elastic and shakedown limit respectively. The elastic and shakedown limits are expressed as a ratio of the Peak Hertz contact stress (Po) and the yield stress of the material in simple shear (k). The ratio (Po/k) for the elastic limit is 3.1 and the shakedown limit ratio is 4 [21]. The ratio is referred to as a load factor or relative Hertz contact pressure. For all tests conducted a load factor (Po/k) is determined in order to evaluate into which deformations regime the test is conducted. An example of this is if a load factor (Po/k) of 2 is calculated the rolling contact will fall within the elastic regime as 2 < 3.1 which is lower than the elastic limit. If a value of 3.5 is calculated the material will experience elastic shakedown as 3.1 < 3.5 < 4 because 4 is the elastic limit [9].

A detailed explanation of both the elastic and shakedown limits, deformation regimes and rolling resistance are discussed. Within each of the sections reference is made to the researchers and theory to explain the above mentioned topics.

6.1 Rolling resistance

Rolling resistance is experienced in practical applications of rolling contact. The resistance is due to the transfer of torque between rolling surfaces [9]. The magnitude of torque transferred during rolling contact will very from one application to another. However in general, under rolling contact conditions Q is the tangential force and P is the applied normal load. For pure/free rolling contact the ratio Q/P = 0. However, for tractive rolling the ratio Q/P is greater than 0 but less than the maximum value of friction 'μ' (0 < Q/P< μ), where 'μ' is the coefficient of friction. For rolling resistance the ratio is just greater than 0 and substantially smaller than the limiting value of friction μ (0 < Q/P<< μ). It can be seen therefore that rolling resistance can be seen as the lower limit of the tractive rolling condition. Explained in the following text is a discussion of tractive rolling and free rolling resistance [15],[24].

6.1.1 Tractive rolling

An overview of contact mechanics published by J.R. Berber, M. Ciavarella (2000) [16] highlighted coulomb's law of friction to be the most uncomplicated friction condition. The condition identifies that any position within the contacting area of two mating surfaces under traction will experience either a slip or stick condition. The total contact area can be divided into either of these two conditions. The normal force is denoted by P and the tangential force is identified as Q, while the coefficient of friction is μ. Within the stick region the tangential traction (Q) is less than μP and no relative motion is experienced. However within the slip region, relative motion is experienced and the tangential traction is equal to μP. Therefore the

maximum tangential traction is achieved when the complete contact area experiences a slip condition (i.e. Q = μP) [16].

Figure 6.2 illustrates the slip stick areas present within the contact area of two cylinders in rolling-sliding contact [17].
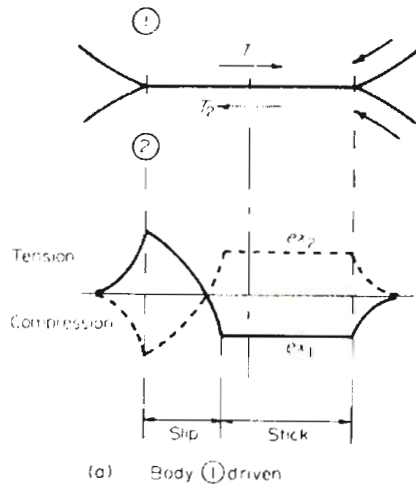
Figure 6. 2 Slip stick area acting at contact interface [17]

Microslip is present at the contacting interfaces as a result of the strains generated within the slip and stick areas. The microslip results in a difference in the linear velocities of the contacting surfaces. The differences in the linear velocities of the two contacting surfaces can be measured. Using the measured values a creep velocity and creep ratio can be calculated. The creep ratio can be expressed as a percentage creep [17]. The following equations calculate the creep ratio. A full derivation of the equations listed below can be found in text [17].

The Difference between the two rigid bodies circumferential linear velocities.

$$\Delta U = U_{X1} - U_{X2} \qquad (14)$$

U_{X1} = Circumferential velocity of cylinder 1 in the x direction
U_{X2} = Circumferential velocity of cylinder 2 in the x direction

The mean circumferential velocities is calculated by

$$U = \frac{U_{X1} + U_{X2}}{2} \qquad (15)$$

The creep ratio is given by:

23

$$\frac{\Delta U}{U} = \frac{\mu a}{R}\left[1 - \left(1 - \frac{T}{\mu P}\right)^{\frac{1}{2}}\right] \qquad (16)$$

Where:

T = Tangential traction

μ = Coefficient of friction

R = Radius of cylinder

P = Load per unit length

a = Half the contact width

U = linear velocity of the surface

The equation for the creep ratio can be rewritten in the non-dimensional form:

$$\frac{\Delta UR}{U\mu a} = \left[1 - \left(1 - \frac{T}{\mu P}\right)^{\frac{1}{2}}\right] \qquad (17)$$

Equation 17 has been verified using experimental results in the calculation of the creep velocity (ΔU). The experimental results have been obtained for a various quantities of applied force (P), Tangential force (T). The accuracy of the theoretically calculated curve compared with the experimental measurements can be observed in figure 6.3 [17].
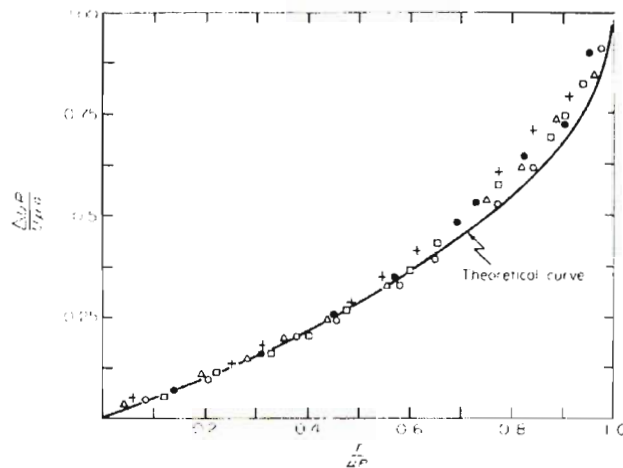
Figure 6. 3 Experimental and theoretical comparison of micro slip [17]

If any friction resulting in the transfer of torques is present during the rolling process, a creep velocity will be measured. During near perfect rolling conditions the quantity of the torque transmitted is extremely small and as a result the creep velocity measured is of an extremely small magnitude. The creep ratio is a result of microslip [17]. Research conducted by A.Nakajimi, T. Mawatari, M. Yoshida, K. Tani, A. Nakahira (2000) [18] into the durability of coated surfaces tested at different slip ratios identified a slip ratio of ≈ 0 % is obtained for free rolling conditions.

24

6.1.1 Free/ Pure rolling resistance

Free or pure rolling conditions are defined as rolling without shear surface tractions [19], however in every day applications of rolling contact, resistance to rotation is observed. Two theories as to the factors responsible for the resistance in rolling contact consider the inelastic behavior of the rolling cylinders. Both of the theories generate a coefficient of rolling friction. The theories are discussed as follows [20],[9].

Figure 6.4 illustrates an absolutely rigid cylinder rolling over a softer surface. The applied load (W) on the cylinder deforms the softer surface creating a small rise of material in front of the cylinder. The cylinder can not climb over the material rise and therefore the pressure distribution is always present during rolling motion. Therefore to continue rolling contact a small driving force P must be applied to the cylinder. The interaction can be likened to rolling out a bump in a carpet [20].
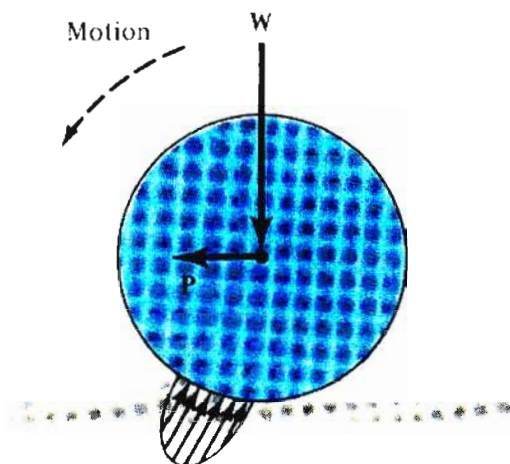
Figure 6. 4 Soft surface of contact [20]

With reference to Figure 6.5. If rolling contact is maintained at constant velocity and a resultant force N substituted for the pressure distribution, then forces W,P and N act persistently on the cylinder during motion [20].

25
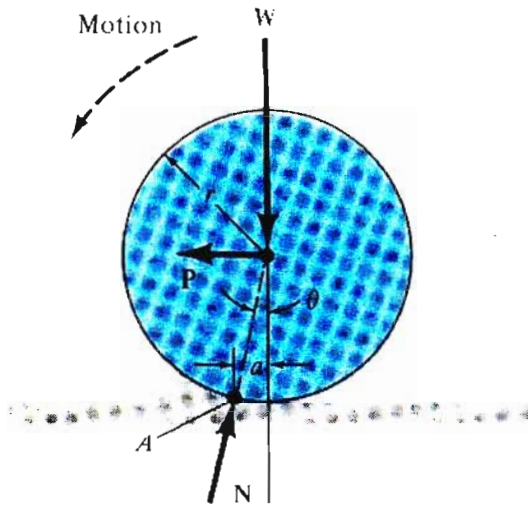
Figure 6. 5 Contact pressure replaced with normal force [20]

Summing the moments about A for an equilibrium condition yields:

$$Wa = P(r \cos \theta) \tag{18}$$

As the deformations are substantially smaller than the cylinder radius:

$$\cos \theta \approx 1 \tag{19}$$

Therefore

$$P = \frac{Wa}{r} \tag{20}$$

a is the coefficient of rolling resistance [20]

The second theory of rolling resistance is as follows:
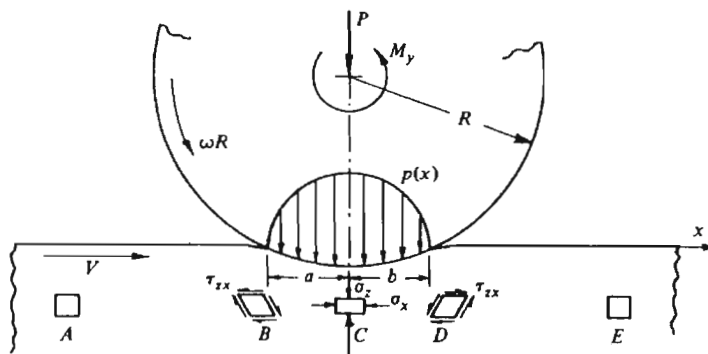
Figure 6. 6 Inelastic rolling contact [9]

Figure 6.6 illustrates one of many material elements passing through the contact region during rolling contact. The material element experiences increasing and decreasing compressive stress and as a result strain energy is developed and released. The strain energy in the material element is increased over the first half of the contact region as the compressive stress is increased to a maximum at the centre of contact. The strain energy is then released or reduced over the second half of rolling contact as the material element is allowed to expand as the compressive stress is reduced. A small quantity of energy is dissipated during the cyclic loading as no material is completely elastic. The energy loss is identified as a hysteresis loss factor and is expressed in terms of the highest quantity of strain energy generated during each loading cycle [9].

An expression for the relationship between the hysteresis loss factor and the moment required to maintain motion is expressed as [9]:

$$\mu_R = \frac{M_y}{PR} = \alpha \frac{2a}{3\pi R} \qquad (21)$$

My = Rolling resistive torque / torque required to maintain motion

R = Radius of cylinder
a = Half the contact length
P = Contact load
α = Small fraction of the of the strain energy dissipated (Hysteresis loss factor)
μR = coefficient of rolling resistance

Comments and observation have been made with respect to the above analysis. Both the coefficient of rolling resistance and hysteresis loss factor are discussed as follows [17]:

While the hysteresis loss factor/ energy dissipated during rolling contact is similar to that of a simple tensile test, the magnitude is however different. In both cases energy is dissipated in the elastic deformation of a material, however due to the rather more complex elastic deformation under rolling contact the hysteresis loss factor can be three times larger.
The analysis assumes the hysteresis loss factor to be constant, regardless of the quantity of straining. However the degree of straining may vary for large strain conditions.
The analysis further assumes that the hysteresis loss factor and therefore rolling resistance is constant regardless of rolling velocity or temperature. However, both strain rate and temperature affect the magnitude of strain generated [17].

6.2 Rolling contact stress analysis

Rolling contact may be found in many applications such as roller bearings, gears in mesh and wheels on rails [1]. As a result of the contact, stresses are generated within the contacting bodies. The stresses act within the contact region. The cyclic nature of the stresses due to rolling can result in rolling contact surface fatigue. Material elements within the contact region experience direct stress in three directions, shear stress and shear strains. The material within the contact region responds differently under increased contact loading. The material response is dependent on the material property (k) and the applied Hertz contact stress (Po). The load factor or relative Hertz contact pressure (Po/k) can be calculated for any specific rolling contact condition. The magnitude of the ratio will determine the response of the material in the contact region. Material response under rolling contact has been divided into four deformation regimes. Within each of the deformation regimes the material in the contact region responds differently to the applied contact stress. The four contact deformation regimes (material responses) are as follows: elastic material response, elastic material shakedown, plastic shakedown and rachetting. The limiting load factor (Po/k) for elastic material response is referred to as the elastic limit (Po/k = 3.1). The limiting load factor for the material shakedown is the shakedown limit (Po/k = 4) [9].

The testing conducted in the current research involved the testing of coated test specimens under 2 dimensional rolling contact. The tests were conducted within two of the deformation regimes. An understanding and overview of the contact stress and material responses is therefore of significance. Load factors for each test specimen were calculated.

Researches Merwin and Johnson analyzed rolling contact for two dimensional contact. The analysis identifies deformation regimes in which specific material responses can be expected. The deformation regimes are bounded by limiting values of load factors ratio (Po/k) and are identified as follows [21]:

Po/k < 3.1   continuing elastic deformation

3.1< Po/k < 4   Transient plastic deformation (shakedown)

Po/k > 4   continuing elastic-plastic deformation

Additional research into rolling contact stress analysis was conducted using Semi analytical approaches and finite element methods. The contact stress analysis has been performed using semi analytical approaches by a few researches, A.D Hearle, K.L Johnson (1987) [22], Y. Jiang, H. Sehitoglu (1994 & 1996) [23] [24]. The semi analytical methods are simple and are based on

an elastic solution. The rolling contact stress distributions are predicted accurately and a large number of rolling contact cycles may be simulated using these methods [15].

A number of elastic-plastic rolling contact stress analyses have been conducted using FE methods. Finite element analyses were published by V. Bhargava, G. T Hahn, C.A. Rubin (1985) [28], A.M Kumur, G.T Hahn, V. Bhargava (1989) [54.], B. Xu, Y. Jiang (2002) [15], Y. Jiang, B. Xu, H. Sehitoglu (2002) [19]. These finite element simulations for rolling contact make use of similar mesh models and boundary conditions [15].

A number of proposed material behavior models were also developed for use in the finite element analysis. Material behavior models were published by Y. Jiang, H. Sehitoglu (1996) [25] [26] [24]. The published texts presented plasticity models for material experiencing cyclic loading.

The analyses of rolling contact using finite element models, semi analytical methods and material response models are complex, the details of which are beyond the scope of the research conducted. However, the results and observations made by the above mentioned researchers enable an understanding and overview of rolling contact analyses and material response behavior to be gained.

Presented here is an overview of contact stress analysis and material behavior. Results and observations form the above mentioned published research is referenced to identify important concepts in the rolling contact analysis. The material response behavior, load ratios and deformation regimes are discussed.

Under cyclic loading an elastic material can experience one of four possible types of material response. The material responses are also referred to as deformation regimes and are identified as follows; perfectly elastic, elastic shakedown, plastic shakedown and ratchetting. Figure 6.7 illustrates the relationship between stress, strain and material response under cyclic loading for an elastic material [27].
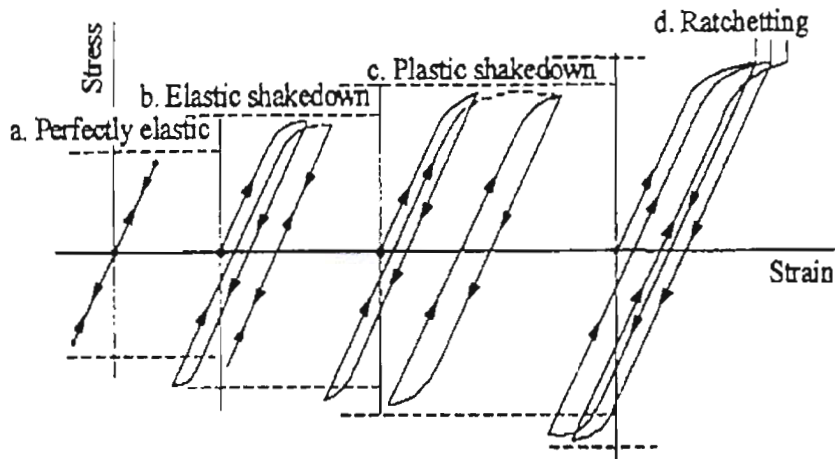
Figure 6. 7 Material response to cyclic loading under rolling sliding contact [27]

During rolling contact, stresses inside the contact region are cycled as material is repeatedly rolled through the contact region. Some material elements within the contact region exhibit specific material responses due to the applied load [27].

For rolling contact, the peak hertz contact pressure (Po) can be calculated for any specific contact condition. A specific material property k for an elastic material can be determined. A relationship between k and the yield stress (Y) in simple tension for an elastic material is given as [1]:

$$k = \frac{Y}{\sqrt{3}} = 0.577Y \qquad (22)$$

A load factor (Po/k) or relative Hertz contact stress for any rolling contact condition can then be determined. The load factor relates the Hertz contact stress (Po) to the material property (k) to determine the material response within the contact region during rolling contact. Most published research into rolling contact analysis makes reference to the load factor for a given contact condition. The deformation regime into which the rolling contact falls will determine the material response.

The text in the following chapters discusses the material response within each of the deformation regimes. A full derivation and discussion of both the elastic limit and the shakedown limit are also both presented. The effect of traction on rolling contact stress is briefly explained.

6.2.1 Elastic regime

Under pure rolling contact conditions; material with in the contact region responses completely elastically if the value of load factor remains below the elastic limit. The restrictive value of load factor at which material within the contact region will start to yield is 3.1. Below this load factor value all material within the contact region will remain entirely elastic. The stresses calculated using the equations for static two dimensional contact (Chapter 3) apply for this rolling contact case. The maximum value of the load factor at which material in the contact region ceases to respond elastically was first identified by researches Merwin and Johnson in 1963 [21]. Within the elastic regime no residual stresses or strains are initiated under rolling contact.

In summary the load factor (Po/k) range for elastic material response under rolling contact is $0 < Po/k < 3.1$. The limiting load factor for this regime is the elastic limit Po/k = 3.1. A derivation and discussion of the elastic limit is covered in Chapter 6.2.4 [9].

6.2.2 Elastic material shakedown

Under pure rolling contact conditions, rolling elements loaded above their elastic limit encounter cumulative plastic deformation. The deformation is the consequence of the progressive shearing of surface layers relative to subsurface material [22].

Depending on the load factor ratio (Po/k) under which rolling contact is conducted the material within the contact region will respond in one of two ways. For a load factor of greater than 3.1 and less than 4 the material will be subjected to elastic shakedown, while for load factor ratios greater than 4 the material inside the contact region will undergo a combination of plastic shakedown and ratchetting [9].

According to Melan's theorem stated in text by K.L Johnson [9] the parameters for material shakedown are as follows: "If any time independent distribution of residual stresses can be found which, together with the elastic stress due to the load, constitutes a system of stresses within the elastic limit, then the system will shakedown. Conversely if no such distribution of residual stresses can be found, then the system will not shakedown and plastic deformation will occur at every passage of the load" [9].

Plastic deformation occurring during the preliminary rolling contact cycles is referred to as elastic shakedown. Elastic material shakedown is limited as residual stresses and strain hardening result in the material achieving an elastic material response as a steady state condition. The load factor ratio below which this material response will occur is the shakedown limit [27].

In summary elastic material shakedown under rolling contact conditions is experienced for the following range of load factor ratios: 3.1< Po/k <4. The lower value of load factor is 3.1 and is referred to as the elastic limit while the upper value of the load factor 4 is referred to as the shakedown limit. The shakedown limit is fully discussed and explained in section 6.2.7 entitled the shakedown limit [21].

In 1994 Y. Jiang, H. Sehitoglu [23] analyzed rolling contact using a plasticity model to determine the residual stresses and cumulative surface displacement rate for rolling contact under different load factor values. Figure 6.8 shows two graphs depicting the residual stresses in the x and y direction at different depths below the surface. The third graph in the figure illustrates the residual shear strain rate ($\Delta\gamma_{xz}$) a varying depths below the contact surface with respect to the applied load factor.
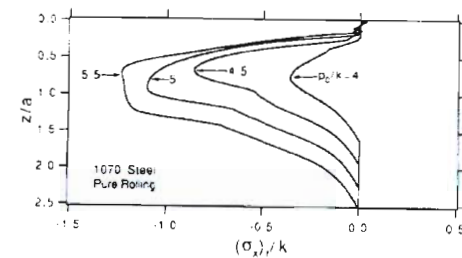
Fig. 8(a) Variation of residual stress $(\sigma_x)_r$.
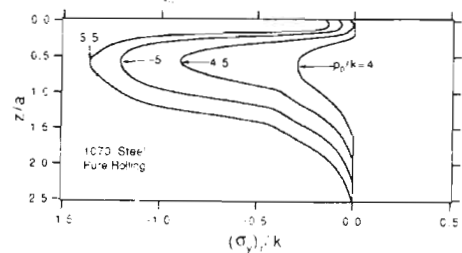
Fig. 8(b) Variation of residual stress $(\sigma_y)_r$.
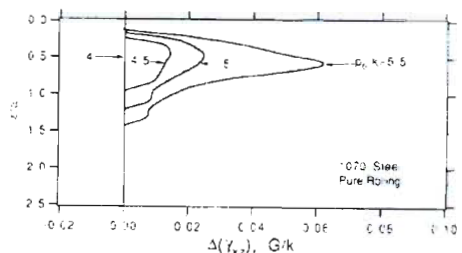
Fig 8(c) Variation of residual shear strain rate $\Delta(\gamma_{xz})_r$.

Figure 6. 8 Steady state residual stresses and shear strain rate [23]

It can be seen from Figure 6.8 that while residual stresses in both the x and y directions are predicted for a load factor value of 4 there is approximately 0 residual shear strain rate. The residual shear strain rate can be integrated with respect to the depth below the surface to determine cumulative surface displacement. At a load factor ratio of Po/k = 4 there is no residual strain rate indicating that the material has experienced elastic shakedown. At values of Po/k>4 residual strain rates are predicted, this highlights the fact the limiting value of material shakedown response in terms of a Po/k ratio is 4 [23].

In 1985 V. Bhargava, G. T Hahn and C.A. Rubin [28] used a finite element model to analyze stresses within the contact region under rolling contact conditions. Material responses for different load factor ratios were analyzed. For a load factor ratio of 3.5 material shake down was predicted. This prediction is in line with the theory that for a load factor range between 3.1 and 4 material shake down is a result.

6.2.3 Plastic shakedown and ratchetting

The testing and experimentation in the present research is conducted below the shakedown limit (Po/k = 4) ratio. This means that a full explanation and study of material behavior above the shakedown limit falls outside the scope of the present research. However a brief description of the material response above the shakedown limit (Po/k > 4) is of interest.

Material within the contact region under rolling contact experiences cyclic loading. The material response due to the cyclic loading above the shakedown limit is either ratchetting or plastic shakedown. Plastic shakedown or cyclic plasticity is a material response to cyclic loading for which an elastic plastic closed loop is formed, indicating that no additional plastic deformation is developed with further loading cycles [27]. The ratchetting material response is however a continuous accumulation of strain with every rolling contact cycle completed [29]. Figure 6.7 illustrates the relationship between stress, strain and material response under cyclic loading for an elastic material.

Research has been conducted to understand the effects of ratchetting material response in rolling contact. In 1996 Y. Jiang, H. Sehitoglu [25] [26] developed relationships for material behavior used in the calculation and prediction of cyclic ratchetting plasticity. In 1997 X. Su, P. Clayton [29] conducted ratchetting strain experiments with steel specimens under rolling contact. The following graph was plotted as a result of the research. It is observed in the graph that the strain rate decreases asymptotically with number of rolling cycles; concluding that ratchetting will

continue to occur continuously during rolling contact. The result of ratchetting material behavior is failure of the surface due to fatigue [29].
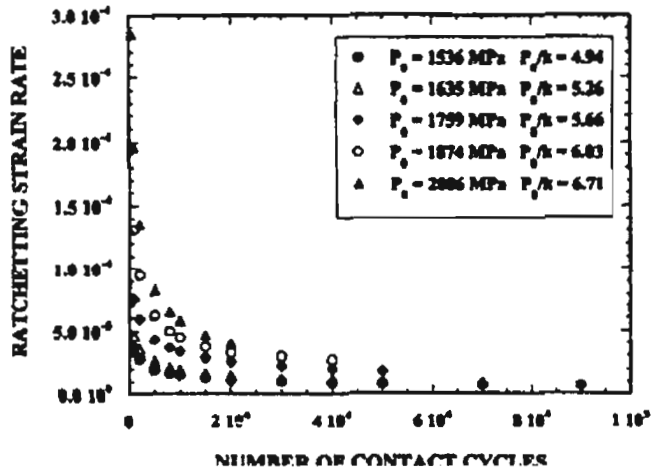
Figure 6. 9 Ratchetting strain rate versus number of contact cycles [29]

In 1996 Y. Jiang, H. Sehitoglu [24] applied a plasticity model in a semi analytical analysis of rolling contact stresses. Figure 6.10 illustrates the models predicted results. The following graphs were plotted at three different Po/k ratios and represent the amount of surface ratchetting predicted verse the number of rolling cycles. The effect of the traction ratio (Q/P) on the amount of surface ratchetting is also illustrated. The total normal load is P and the total tangential force is denoted by Q.

34
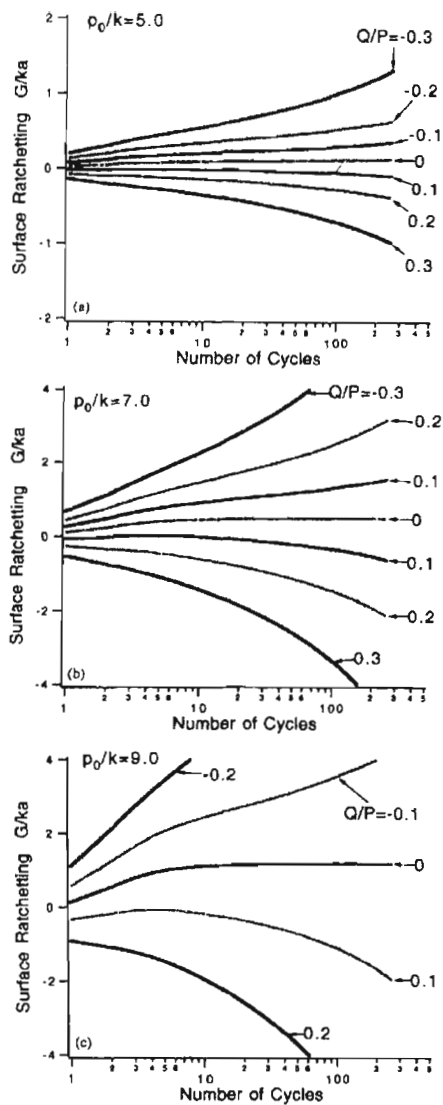
Figure 6. 10 Surface ratchetting compared to number of rolling passes [24]

It can be concluded that the ratchetting material response is increased with an increase of both load factor ratio (Po/k) and traction ratio (Q/P) [24].

6.2.4 Elastic limit

As discussed in Chapter 6.2.1, under rolling contact, material within the contact region behaves elastically due to the applied contact stresses. However, if the applied contact force in increased the stresses within the contact region are increased in magnitude. At a specific quantity of contact stress subsurface material will begin to yield.

The precise value at which yielding occurs is referred to as the elastic limit. Material within the contact region stressed under the elastic limit (Po/k = 3.1) behaves elastically. However rolling contact above the elastic limit will results in elastic material shakedown [21]. The testing

conducted in the present research is performed above and below the elastic limit, therefore a detailed explanation and description is required.

In text by K.L Johnson [9] it is stated that the Po/k ratio for which the elastic limit is reached is 3.1 or 3.3 at a depth below the surface of 0.7 z/a or 0.78 z/a . The difference in the calculated value is varies depending on the yield criteria used to predict yielding [9].

In the following text the elastic limit ratio and the position of yielding is determined. In order to determine the magnitude of load factor (Po/k) at which material elements within the contact region will begin to yield, principle stresses within the region are determined. Substituting the principle stresses into two theories of failure equations, predicts failure in the form of yielding.

The calculation of the position with the contact region is determined from a plot of the failure theories vursus depth below the surface. The matlab program written to determine elemental stresses within the contact region was used to determine both the magnitude and position of the point of first yielding. A previous section of contact stresses modeling discusses the matlab program used in detail.

6.2.4.1 Principle stresses

Text complied by A. P. Boresi & O. M Sidebottom (1985) [1] defines principal stresses as the following: "Any general state of stress at any point 0 in a body, there exist three mutually perpendicular planes at point 0 on which the shear stresses vanish. The remaining normal stress components on these three planes are called principal stresses" [1].

It is the principal stresses described above which are used in the theories of failure to determine the point in the contact region at which the point of first yielding will occur.
The principal stresses acting on any element within the contact region can be calculated using the following equations [9].

$$\sigma_1 = \tfrac{1}{2}(\sigma_x + \sigma_z) + \tfrac{1}{2}\left[(\sigma_x - \sigma_z)^2 + 4\tau_{zx}^2\right]^{1/2} \qquad (23)$$

$$\sigma_2 = \tfrac{1}{2}(\sigma_x + \sigma_z) - \tfrac{1}{2}\left[(\sigma_x - \sigma_z)^2 + 4\tau_{zx}^2\right]^{1/2} \qquad (24)$$

$$\sigma_3 = \nu(\sigma_x + \sigma_z) \qquad (25)$$

The following graph is plotted using the matlab program discussed in text on contact stress modeling. The graph illustrates the distribution of the principal stresses about the centre of the contact region at various depths below the surface.

The y axis illustrates the depth below the surfaces as a ratio of the measured depth (z) divided by half the contact width (a). As both of the values are measured in the same units the ratio has no units. The x axis represents the values of the principal stresses (σ_1, σ_2, σ_3) divided by the peak Hertz contact pressure (Po). The ratio is also a unit less measure [9].
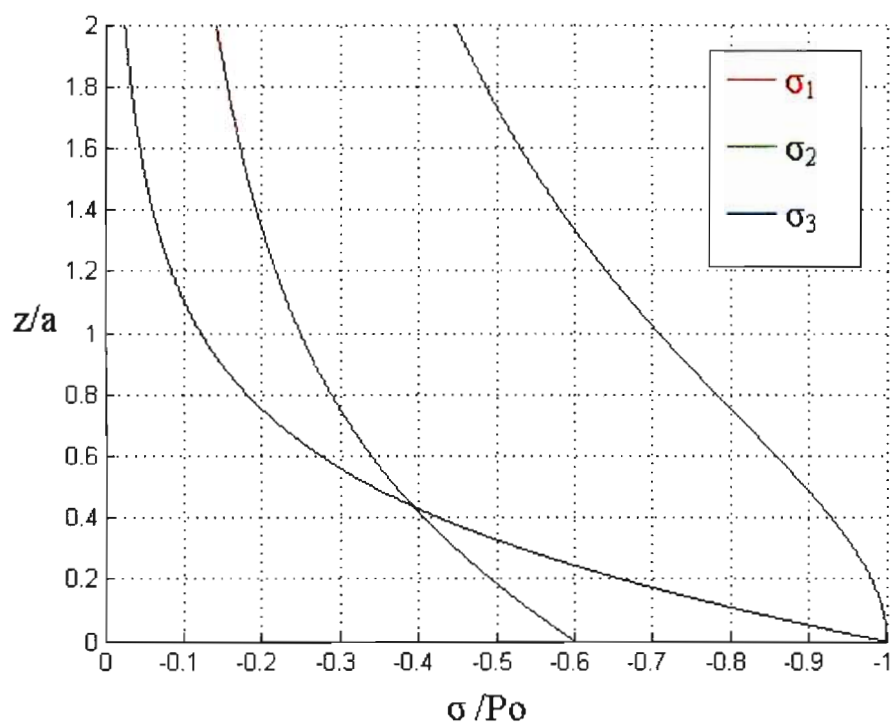
Figure 6. 11 Principal stress distribution and magnitude vs depth below the surface

Principal stress 1 (σ_1) = Red
Principal stress 2 (σ_2) = Green
Principal stress 3 (σ_3) = Blue

6.2.4.2 Yield criteria / Failure theories

Many engineering components are subjected to complex loading conditions, resulting in complex stresses been generated within the material. Predicting the stresses and load conditions at which yielding or failure will occur is therefore difficult. However, theoretical criteria have

37

be established to combine the effect of the complex stress states in determine yielding. The criteria are referred to as theories of failure [30].

A number of failure theories have been proposed, however only two criteria are examined due to the application of the criteria to ductile materials [9]. The two criteria examined are the Maximum shearing stress theory (Tresca) and the Distortion energy theory (Von Mises).The theories are expressed as follows [30]:

Distortion energy theory (Von Mises):
"Failure is predicted to occur in a multiaxial state of stress when the distortion energy per unit volume becomes equal to or exceeds the distortion energy per unit volume at the time of failure in a simple uniaxial stress test using a specimen of the same material [31]".

Maximum shearing stress theory (Tresca-Guest theory):
"Failure is predicted to occur in a multiaxial state of stress when the maximum shear stress magnitude at magnitude becomes equal to or exceeds the maximum shearing stress magnitude at the time of failure in a simple uniaxial stress test using a specimen of the same material [31]".

The equations for both Tresca and Von Mises failure theories are expressed as follows [31]:
Distortion energy theory (Von Mises):

$$J_2 = \tfrac{1}{6}\left\{(\sigma_1 - \sigma_2)^2 + (\sigma_2 - \sigma_3)^2 + (\sigma_3 - \sigma_1)^2\right\} = k^2 = \frac{Y^2}{3} \qquad (26)$$

Maximum shearing stress theory (Tresca-Guest theory):

$$\max\left\{|\sigma_1 - \sigma_2|, |\sigma_2 - \sigma_3|, |\sigma_3 - \sigma_1|\right\} = 2k = Y \qquad (27)$$

For the above equations:

$(\sigma_1, \sigma_2, \sigma_3)$: Principal stresses

k : Yield stress in simple shear

Y : Yield stress in tension or compression

For equations 26 and 27 failure is predicted if the value calculated on the left hand side of the equation is equal to the right hand side. A greater value on the left hand side of the equations indicates failure.

A contract between the two yield criteria can be seen in the comparison of the two stress criteria in the two dimensional principle stress state. Figure 6.12 illustrates the accuracy to which the yield criteria predict the yield for numerous tests on ductile materials. It can be seen that both the criteria are acceptable while the Tresca maximum shear stress criterion predicts failure a slightly lower stress level. The Von Mises (shear strain energy) criteria is observed to more accurately predicted the yield of the tested specimens [30].
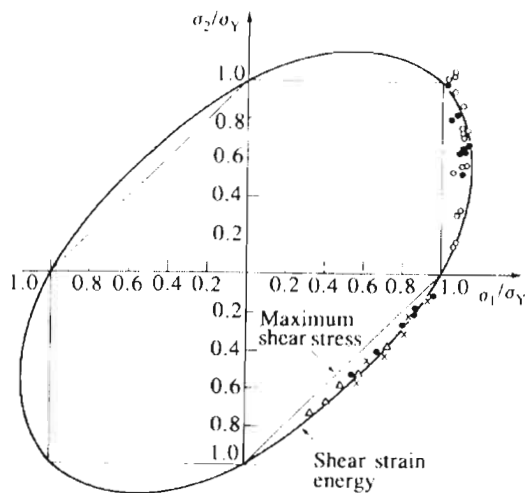
Figure 6. 12 Yield criteria compared with actual test measurements [30]

6.2.4.3 Plastic yielding in contacting cylinders

In the following text the value of the Po/k ratio for which the elastic limit is reached, as well as the position within the contact region at which yielding occurs is determined.

The matlab program discussed in section 4 (contact stress modeling) was used in the substitution of equations and plotting of graphs.

By the substitution of complex elemental stresses (equations 11, 12, 13) into equations 19, 20, 21 the principal stresses for any point within the contact region are calculated. The principal stresses about the centre of the contact region are the largest. Therefore the x value input into equations 11, 12, 13 is zero. The yield criteria equations (26, 27) are evaluated through the substitution of the principal stress equations. The complex stresses, principal stresses and

39

yielding criteria were all able to be plotted with depth below the surface using the matlab program mentioned above [9].

With reference to yield criteria (equation 26,27), failure is predicted if the value calculated on the left hand side of the equation is equal or greater than the right hand side. Graphs of the variation of the yielding criteria (Left hand side of the equation) against depth below the surface were plotted. The yield criteria evaluated in the following text are that of Tresca and Von Mises.

Evaluation of the Tresca yield criteria is as follows:

Setting the result for the left hand side of equation 27 to be equal to xPo, equation 27 becomes:

$$xP_0 = 2k = Y \qquad (28)$$

$$x = \frac{2k}{P_0} \qquad (29)$$

Plotting the varying value of x with depth below the surface, the following graph is obtained.
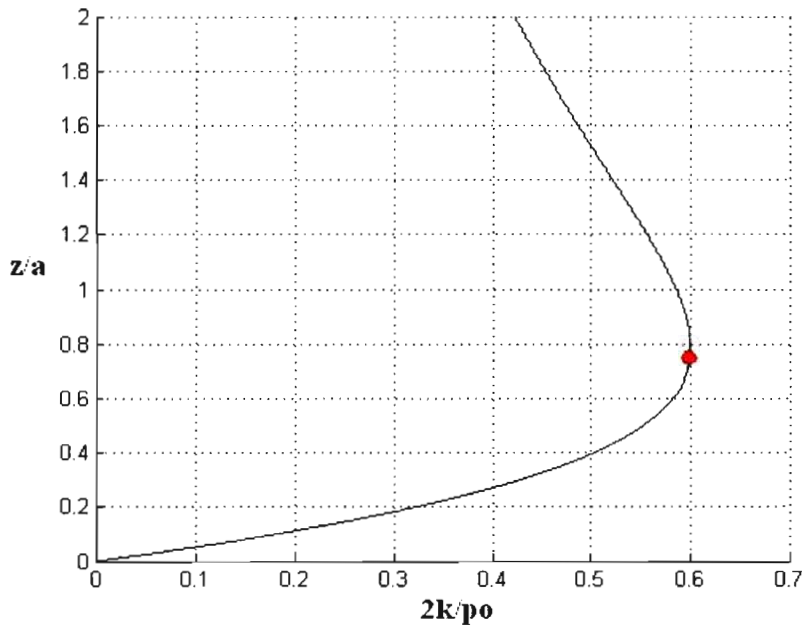
Figure 6. 13 Tresca yield criteria with depth below the surface

The red dot in the figure above is the position at which the maximum value for x is reached. The maximum value of x (0.6) is observed to be at a depth below the surface of 0.78 z/a.
Substituting the maximum value of x (0.6) into equation 28 yields:

40

$$0.6P_0 = 2k = Y \tag{30}$$

$$\frac{P_0}{k} = 3.33 \tag{31}$$

$$P_0 = 1.67Y \tag{32}$$

Evaluation of the Von Mises yield criteria is as follows:

Setting the result for the left hand side of equation 26 to be equal to $xPo2$, equation 26 becomes:

$$xP_0{}^2 = k^2 = \frac{Y^2}{3} \tag{33}$$

$$x = \frac{k^2}{P_0{}^2} \tag{34}$$

Plotting the varying value of x with depth below the surface, the following graph is obtained.
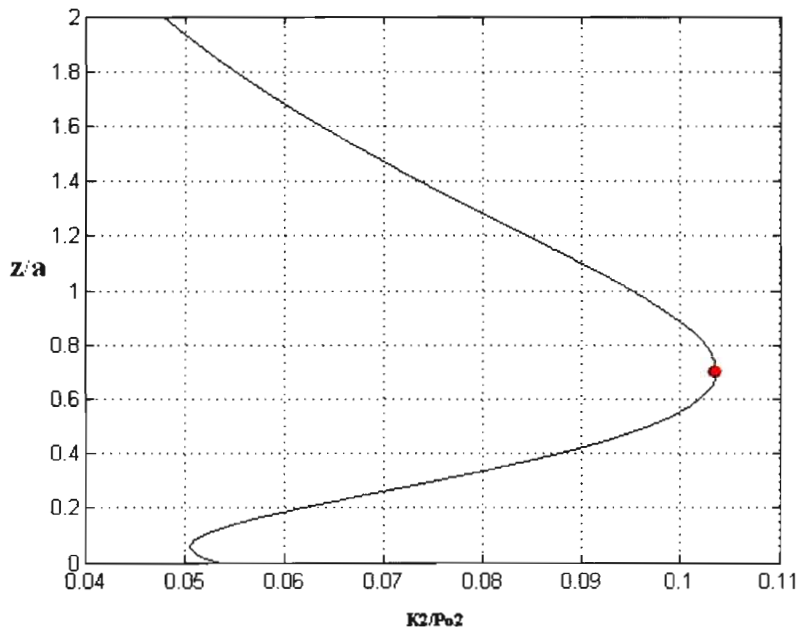
Figure 6. 14 Variation of Von Mises yield criteria versus depth below the surface

The red dot in the figure above is the position at which the maximum value for x is reached. The maximum ratio of x (0.104) is observed to be at a depth below the surface of 0.7 z/a.

Substituting the maximum value of x (0.104) into equation 33 yields:

41

$$0.104 P_0{}^2 = k^2 = \frac{Y^2}{3}$$

(35)

$$\frac{P_0}{k} = 3.1$$

(36)

$$P_0 = 1.79Y$$

(37)

The Po/k ratio for the elastic limit to be reached is predicted as 3.1 and 3.3 by the Von Mises and Tresca yield criteria respectively. The position below the surface at which the yielding will initiate, is predicted as 0.7 and 0.78 of the half contact width (a) by the Von Mises and Tresca yield criteria respectively. For the current research the load factor (Po/k) for the elastic limit will be accepted as 3.1.

6.2.5 Shakedown limit

As mentioned in chapter 6.2.2, the shakedown limit is the restrictive load factor (Po/k) value at which elastic material shakedown will no longer be experienced. Rolling contact conducted at greater load factor values will result in plastic shakedown and ratchetting material responses [21].

Elastic material shakedown takes place during the first couple of rolling contact cycles. During these initial cycles, residual stresses are generated within the contact region. After the residual stresses are formed the material within the elastic region behaves elastically [9].

In 1987 work by A.D Hearle, K.L Johnson [22] stated that Shakedown is governed by the maximum orthogonal shear stress ($\pm \tau zx = 0.25$ Po) which occurs at the following points within the contact region: xm = $\pm$ 0.87a, zm = 0.5a. The shakedown limit will be exceeded if the maximum shear stress ($\pm \tau zx = 0.25$ Po) exceeds k. Therefore the shakedown limit can be stated as Po/k = 4 [22]. Presented here with reference to Figure 6.15 and text by K.L Johnson [9] the determination of the value for the shakedown limit is explained.
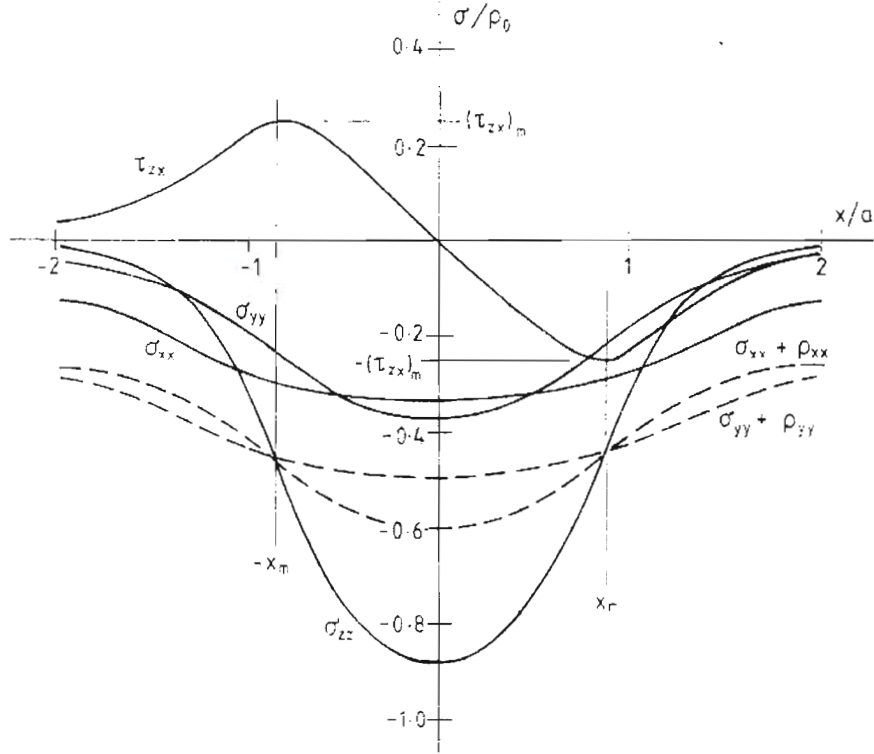
Figure 6. 15 Stress distribution through the contact region at z/a=0.5 [22]

The principal stresses within the contact region are determined by the following equations [9],[22]: Note the equations are the same as equations 23, 24, 25 however with the addition of residual stresses (ρxx, ρyy) formed in the x and y directions [22].

$$\sigma_1 = \tfrac{1}{2}\left(\sigma_{xx}+(\rho_{xx})+\sigma_{zz}\right)+\tfrac{1}{2}\left[\left(\sigma_{xx}+(\rho_{xx})-\sigma_{zz}\right)^2+4\tau_{zx}^{\,2}\right]^{\tfrac{1}{2}} \qquad (38)$$

$$\sigma_2 = \tfrac{1}{2}\left(\sigma_{xx}+(\rho_{xx})+\sigma_{zz}\right)-\tfrac{1}{2}\left[\left(\sigma_{xx}+(\rho_{xx})_r-\sigma_{zz}\right)^2+4\tau_{zx}^{\,2}\right]^{\tfrac{1}{2}} \qquad (39)$$

$$\sigma_3 = \nu\left(\sigma_{xx}+\sigma_{zz}\right)+\left(\rho_{yy}\right) \qquad (40)$$

To avoid yielding using the Tresca criterion, principle stress 1 and 2 (σ_1, σ_2) can be substituted into equation 27. Due to the plane strain condition principle stress 3 (σ_3) is not included. Both sides of equation 27 are then squared, yielding the following [9]:

$$\tfrac{1}{4}\left(\sigma_1-\sigma_2\right)^2 \leq k^2 \qquad (41)$$

Where k is the yield stress in simple shear

Substituting the principal stresses into equation 41 yields

$$\tfrac{1}{4}\left\{\sigma_{xx}+(\rho_{xx})_r-\sigma_{zz}\right\}^2+\tau_{zx}^{\,2} \leq k^2 \qquad (42)$$

43

Observing equation 42; The orthogonal shear stress (τ_{zx}) cannot exceed the yield stress in shear (k) for the equation to be satisfied. However if the residual stress in the x direction is equal to the stress in the z direction minis the stress in the x direction [(ρxx)r = (σzz – σxx)] then the orthogonal shear stress (τ_{zx})can be equal to yield stress in simple shear (k). Stated differently, if the maximum value of orthogonal shear stress (τ_{zx}) anywhere in the contact area equals the yield stress in shear (k) a limiting shakedown condition will be reached. Equation 47 then becomes [9]:

$$\tau_{zx}^{2} \le k^{2} \qquad\qquad (43)$$

As previously mentioned the maximum value of orthogonal shear stress (τ_{zx}) is 0.25Po. Substituting into equation 43 yields the shakedown limit in terms of normalized hertz contact pressure (Po) and yield shear stress (k). The shakedown limit is therefore equal to four [9].

In summary the shakedown limit is reached under 2 dimensional rolling contact at a load factor of Po/k = 4. Where Po is the Peak Hertz contact stress and k is the yield stress in simple shear.

6.2.6 Effect of traction

Tangential forces are often transferred during rolling contact and as a result the contact stresses within the contact region are increased and affected. The effect of traction on two dimensional rolling contact stress analysis is largely reliant on the Po/k ratio at which rolling is experienced and the amount of traction present. The traction ratio (Q/P) is the ratio of the tangential tractive force (Q) and the applied load (P). The ratio is referred to as the coefficient of friction (μ). Figures 6.16 and 6.17 illustrate isochromatic measurements of constant lines of maximum shear stress. The maximum shear stress is observed to be effected by the tangential frictional force. The shear stress is increased and the position within the contact region is also shifted [17].
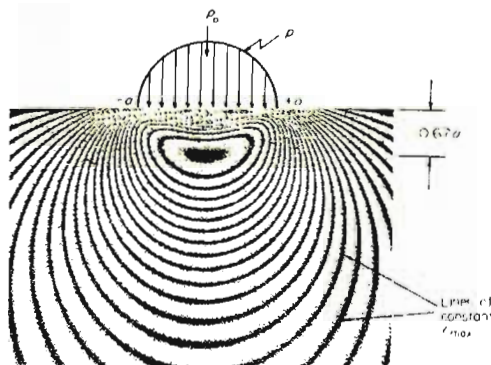
Figure 6. 16 Isochromatics of maximum shear stress [17]
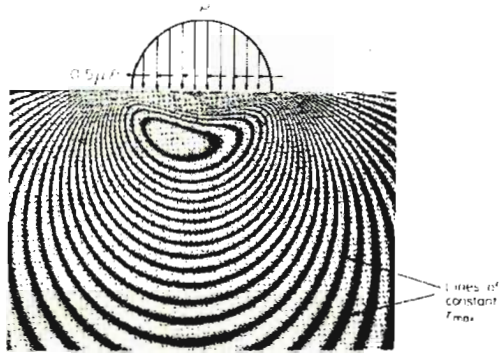
Figure 6. 17 Isochromatics of maximum shear stress affected by friction [17]

Traction experienced during rolling contact effects the residual stresses generated during elastic material shakedown [22]. In 1994 Y. Jiang, H. Sehitoglu [23] analyzed rolling contact stresses, Figure 6.18 illustrates the effect of traction (Q/P) on the residual stresses (σ_x, σ_y) developed in both the x and y directions. It is observed that the magnitudes of the residual stresses are increased with increasing traction.
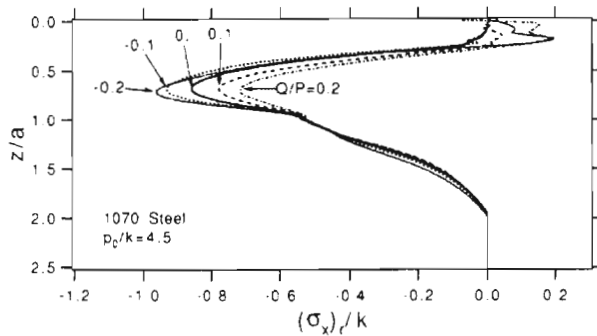
Fig. 9(a) Variation of residual stress (σ_x).
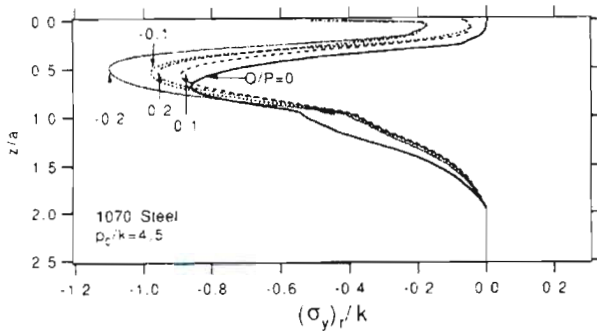
Fig. 9(b) Variation of residual stress (σ_y).

Figure 6. 18 Variation of residual stress with tangential loads [23]

The shakedown map (Figure 6.19) is a graphical representation of the relationship between material responses for given rolling contact situation in terms of friction coefficient (μ) and load factor ratio (Po/k). The material response can exhibit one of four possible behaviors; elastic, elastic shakedown, plastic shakedown or ratchetting and is dependent on the specific rolling contact condition [32].

45
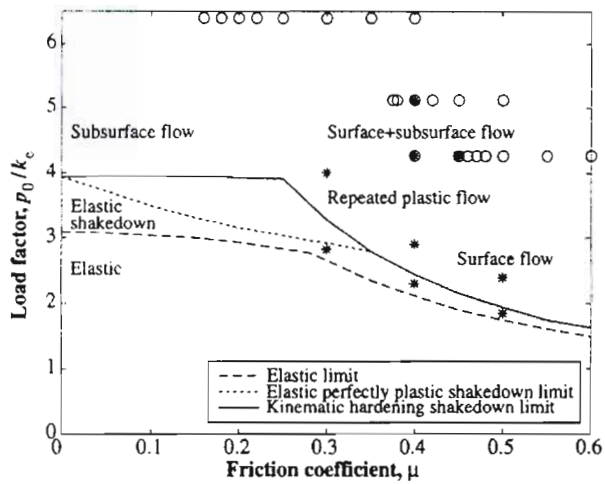
Figure 6. 19 Effects of friction on the shakedown map [32]

Both the elastic limit and the shakedown limit can be observed in the figure 6.19. For pure rolling conditions ($\mu = 0$) the elastic limit is Po/k = 3.1 and the shakedown limit is Po/k = 4 [32].

The testing in the presented research is conducted under near perfect rolling contact conditions. The effect therefore of rolling resistance on the changes in the contact stresses and the position of the yield point Po/k ratio affecting the material behavior is considered to be negligible.

6.3 Rolling contact of coated surfaces

For coated surfaces the microstructure, bonding mechanism, coating thickness and differences in mechanical properties affect the contact stresses predicted by Hertz contact stress theory [33]. However most research and experimentation conducted for coated rolling contact either neglects the effect or only small differences are predicted through calculation.

In 1999 R. Ahmed and M. Hadfield [33] conducted rolling contact experiments on plasma coated ball bearings using a modified four ball machine. The calculated contact stress neglected the coating thickness and difference in mechanical properties of the coating and substrate. In later work by R. Ahmed [34] in 2002, using the same equipment but testing HVOF (High velocity oxy-fuel) coated test specimens, the Peak Hertz contact stress (Po) was calculated using the uncoated test specimen's mechanical properties.

In some research, attempts to account for the effect of the coated surface on the contact stress were made. This was achieved by adjusting the mechanical properties of the coated surface. In 1997 R. Nieminen, P. Vuoristo, K. Niemi and G. Barbezat [35] researched fatigue failure mechanisms of plasma and HVOF coated specimens under rolling contact. The modulus of elasticity used to calculate the Hertz contact stress for the plasma coating was assumed to be the same as that for a detonation gun coating having a similar composition [35].

In 2000 B.Y Sarma and M.M. Mayuram [36] conducted experimental studies on life prediction of thermal sprayed coatings. A first order modulus perturbation method by H. Gao, C. Chiu and J. Lee [37] was used to account for the differences in the elastic matrix through the coating thickness. The variation was a result of the coating thickness and difference in mechanical properties. The equations calculated an effective modulus of elasticity (E) and Poisson's ratio (υ). The effective mechanical properties were used to calculate the contact stress. The maximum contact stress was calculated for both coated and uncoated specimens, the differences in the values were within a few percent of each other.

It is assumed in the present research that the mechanical properties for the coatings are the same as that of the substrate and that the contact stresses calculated are the same for both coated and uncoated test specimen. The mechanical properties used in the calculation of the contact stress are the elastic modulus [E] and Poisson's ratio (υ). This assumption is a generalization and could lead to small errors in the calculation of stresses induced in the substrate, however, the practice is not uncommon (in the field) and merely simplifies the calculations to allow the comparison of the two coating methods under investigation.

7. Surface wear in rolling contact

Under rolling contact conditions, contacting surfaces experience wear. Wear may be defined in one of two ways: "The progressive loss of substance from the surface of a body brought on by mechanical action, or the destruction of material produced as a result of repeated disturbances of the frictional bonds [17]".

Any rolling contact condition has specific characteristics. Characteristics include the transfer of torque, applied load, contact geometry, surface roughness and the presence of lubrication. From the normal load and contact geometry, the contact stresses and contact area are calculated; while torque transfer is a result of the quantity of the slip-stick generated during rolling. Material specific properties along with contact stresses are used to calculate a load factor ratio [52]. Dependent on the quantity of the ratio and a relationship to friction (see shakedown map, Figure 6.19), the material behavior and deformation regime into which the rolling contact will be governed can be determined [32]. Specific rolling contact characteristics are covered in Chapter 6 with emphasis placed on 2 dimensional rolling contact.

Rolling contact is a detailed field of study and the material behavior and wear mechanisms are complex. The quantity and type of wear are determined by the specific rolling contact conditions. Due to the variable nature of the conditions and material responses, calculation and prediction of wear is difficult. However an overview of rolling contact literature indicates that three main types of wear are predominant: Adhesive, abrasive and wear resulting from fatigue [46].

Fatigue wear under rolling contact conditions operates significantly on two scales, macroscopic and microscopic. On the macroscopic scale, fatigue wear is identified as Rolling Contact Fatigue (RCF) while microscopic fatigue wear is known as surface wear. Both wear phenomenon share the same fatigue mechanism however act on separate scales [52]. A large amount of research both experimental and theoretical has been conducted into these wear under rolling contact conditions.

Theoretical analyses and simulations ([38],[39],[32],[40],[41],[11]) of rolling contact wear and in particular rolling contact fatigue, predict cycles to failure under given rolling contact conditions for specific materials. The theoretical analysis for the prediction of failure under rolling contact fatigue exhibit many of the same analytical process but differ in the techniques used. The stresses within the contact region are generally determined semi-analytically or using finite element modeling. The fatigue failure and material response modeling for the cycling

stresses are various and often different as are the crack initiation and propagation models. Many of the simulations predict the position at which a crack will initiate and the cycles to failure.

Testing and experimentation ([42],[43],[44],[45],[46]) has been conducted on test specimens of various shape, size, surface finish, material properties and under different traction, load and in some cases lubricated conditions. A number of tests have been conducted using coated test specimens ([18],[47],[33]).

The shape of the test specimen, applied traction and load affect the contact stresses generated in the contact region. The material properties and material response to cyclic stress affects wear.

The theoretical predictions of rolling contact fatigue and wear are not often backed up by experimental results. And, the experimental results and testing are often application specific and generally do not seek to correlate with theoretical failure predictions.

Under complete sliding contact conditions, adhesive and abrasive wear are well research and understood [52]. As a result, a number of equations have been generated to calculate the resulting wear rates. The equations generally relate material hardness, sliding distance and applied contact pressure to the rate or quantity of wear. The equations can be fond in a number of trigology texts ([48], [31], [49]). The test used most often for complete sliding contact testing is the pin on disc wear machine.

Under rolling contact conditions both rolling and sliding is experienced with the amount of sliding been controlled by the quantity of traction present. As a result, both adhesive and abrasive wear operate under most rolling contact conditions. Furthermore, due to the cyclic nature of rolling contact, fatigue is a contributing factor to the wear or failure of the contacting interfaces. The wear mechanisms under rolling contact is therefore substantially more complex and difficult to calculate specific rates of wear than in the complete sliding case [52].

In this section a general description and overview of adhesive, abrasive and fatigue wear is presented. An overview of conducted research is used to discuss and describe the wear mechanisms and factors affecting the type and quantity of wear. Experimental observations made from other research in rolling contact are also discussed.

The testing conducted in the present research is conducted at near perfect rolling conditions i.e. only very small quantities of traction. The type of contact is two dimensional line contact; and, the stresses under which the tests are conducted are varied between specimens as a result of differences in contact width and applied load.

Figure 7.1 illustrates wear in rolling contact, and the characteristics (traction, asperity interaction etc) resulting in the formation of wear debris [33].
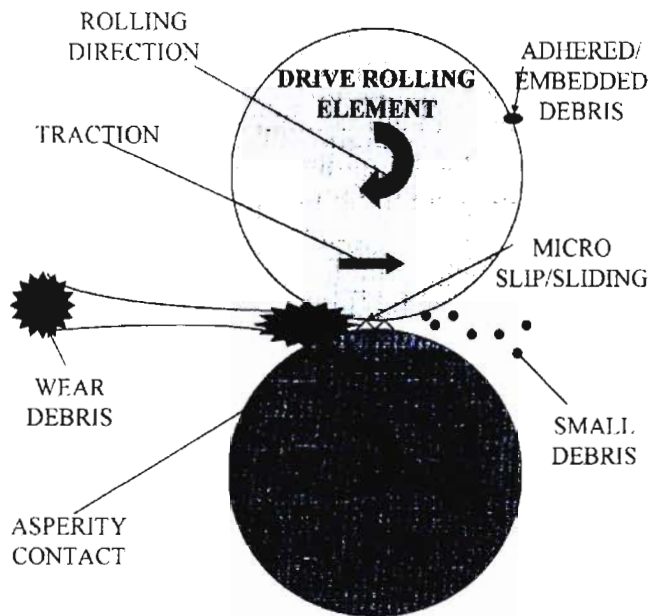
Figure 7. 1 Wear under rolling contact [33]

7.1 Adhesive wear

The mechanics of adhesion between contacting bodies are complex and affected by factors such as plasticity and surface roughness [50]. Adhesion between rolling contact bodies, however, results in adhesive wear. Adhesion further plays an important role in contact fatigue which is also a wear mechanism under rolling contact [51].

Large quantities of friction and high wear rates highlight the effect of adhesive wear under rolling contact. The characteristics are common to most rolling contact systems [44].
Experiments conducted by Q.Y. Liu, RZ. Zhou (2001) [46] under rolling contact conditions noted larger specimen wear with increased adhesion. It was concluded that rolling wear was greatly effected by an applied tangential frictional force [46].

As a result of surface roughness, contacting surfaces mate at only a few surface asperities. The actual area of contact therefore is substantially smaller than the apparent area. While the applied load between surfaces may be small the pressure on the contacting asperities is significantly larger. The stresses generated on these contact points may exceed the yield strength resulting in localized plastic deformation. The deformation can cause the surface points to bond

together. This bonding is referred to as cold welding. If the surfaces are moved relative to each other the welded asperities are fractured. Each fractured particle is observed as a wear fragment. The position at which the contacting points fracture is dependent on the material properties and temperature distributions within the contact area. Adhesive wear can be a limiting mechanism in that once most of surface roughness has been removed very little asperity contact is present. This characteristic is often referred to as a wearing-in-process which improving the surface finishes of mating surfaces [31].

Work by Y.Kimura, M. Sekizawa, A. Nitanai (2002) [52] noted that microscopic fatigue is the controlling factor in adhesive wear. Microscopic fatigue results in failure of surface asperities subjected to recurring frictional and normal forces [52]. Microscopic fatigue wear is covered in the chapter 7.3.2.

7.2 Abrasive wear

Abrasive wear is characterized by surface damage in the form of scratches or grooves often referred to as scoring. The surface damage and the resulting wear particles are generated in one of two ways during sliding contact. Firstly; differences in surface hardness between contacting surfaces. The softer surface is damaged by the contact of the harder surface's asperities. This case is referred to as two-body abrasive wear. Secondly; hard particles can become trapped between the rubbing surfaces. A hard particle passing between the contacting surfaces leads to wear/surface damage of one or both of the surfaces. The wear condition is referred to as three-body abrasive wear [31].

Abrasive wear was noted by R Ahmed [33], [34] in rolling contact experimentation of plasma and HVOF coatings. The testing was conducted on a modified four ball rolling contact machine. Both three body abrasion and plowing were noted to have had occurred on the thermal sprayed test specimens. The abrasion is the result of micro-slip and asperity contact present at the contacting surfaces. The wear mechanism was further noted to be reduced with an increase in coating hardness. The generation of wear debris generated from two body abrasive wear was noted to accelerate wear later in the rolling contact test. It was suggested that the initial wear debris later lead to three body abrasion occurring, accelerating the wear process [34].

7.3 Fatigue wear

As mentioned, fatigue wear is one of the predominant wear mechanisms experienced under rolling contact. In addition the phenomenon occurs on both a macroscopic and microscopic scale [52].

Rolling contact surfaces have both macroscopic and microscopic non conforming contacting geometries. The macroscopic geometries are defined by the overall contact shape of the contacting bodies. The microscopic geometries are those formed by contacting surface asperities, the asperities are the result of surface roughness. Under rolling contact, cyclic stresses are applied to all non conforming geometries, resulting in fatigue on both scales. For the macroscopic non-conforming geometries, Hertz contact stresses and material response behaviors are fully discussed in chapter 6.2. However, the calculation of contact stress acting on surface asperities, in addition to been substantially higher is difficult to predict. On the macroscopic scale fatigue wear is referred to rolling contact fatigue (RCF), while on a microscopic scale it is referred to simply as fatigue wear [52].

The following three figures illustrate the two scales (macroscopic and microscopic) in which fatigue acts under rolling contact. Figure 7.2 illustrates the contact of cylinders (macroscopic scale geometry) while Figure 7.3 is an enlarged detailed view of the interaction of asperities at the contacting interface. Figure 7.4 illustrates the non conforming micro geometries of the asperities. Both macroscopic and microscopic contacts are nonconforming and therefore experience contact stresses. Under rolling contact the cyclic nature of the stresses results in fatigue.
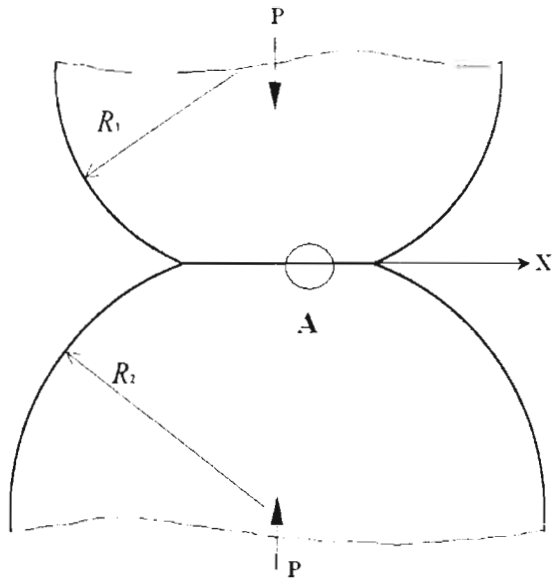
Figure 7. 2 Non conforming macroscopic geometries
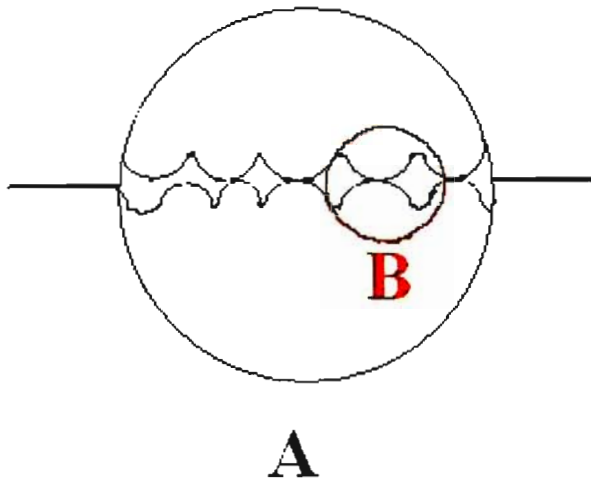
Figure 7. 3 Asperity interaction (Surface roughness)
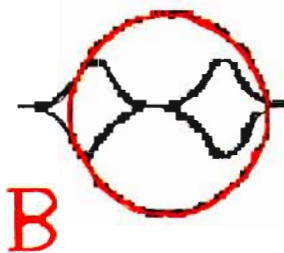
Figure 7. 4 Non conforming microscopic geometries

Rolling contact fatigue (RCF) is manifest in many ways, examples include macro and micro pitting, crack initiation and spalling. RCF often occurs concurrently with wear and other surface damage. As mentioned the mechanical applications which experience RCF failures are numerous however including gears, cams and bearings [53].

Surface failures resulting from RCF are experienced after a specific number of rolling contact cycles, the number of cycles leading up to failure can often be measured. However failure of contacting asperities as a result of microscopic fatigue is more difficult to measure as the contact stresses are far greater than on a macroscopic scale. Due to the increased stress, the fatigue life of contacting asperities is substantially shorter [52].

The continuous removal of tiny wear fragments from a rolling contact surface is characteristic of microscopic fatigue. The wear particles are fatigued and fractured surface asperities. The fatigue cycle is continuous as new asperities are than brought into contact and undergo fatigue. Depending on the material behavior the fatigue mechanism may increase or decrease over time if the quantity of asperities either increases or decreases as rolling contact continues [52].

Not much can be done to reduce the effect of RCF, however the addition of lubricants and improved surface finish can reduce the effect of fatigue wear [52].

Work by G. Donzella, M. Faccoli, A. Ghidini, A. Mazzu (2005) [54] proposed that RCF and wear were competitive failure modes under rolling contact, due to their interaction. As rolling contact fatigue (RCF) is characterized by the generation and propagation of surface cracks (RCF) the removal of the contacting surface through wear reduces the quantities and size of these cracks [54].

A substantial amount of research and experimentation has been conducted using different traction coefficients, materials, loads, contact pressure and geometries. A number of observations have been made. The following sections briefly summarize aspects of the conducted research, to discuss rolling contact fatigue on both macroscopic and microscopic scales.

The testing conducted in the present research is conducted under near perfect rolling conditions with small quantities of slip and slide ratio. The type of contact is two dimensional line contact. The testing is done at different contact stresses by varying the contact width and applied load. Both rolling contact fatigue and wear are influenced by applied contact pressure, traction, Slip/slide ratio and surface finish [58].

7.3.1 Macroscopic fatigue (RCF)

As mentioned in chapter 7.3, macroscopic fatigue or RCF failure can be identified as the spalling of components surface. Spalling is the spontaneous dislodgment of a particle from a surface which prevents the correct function of the component [31]. Prior to spalling a contacting surface will develop cracks which propagate under fatigue leading to fracture after a specific/critical number of stress cycles. Often no noticeable wear is observed prior to spalling. RCF is present in all rolling or rolling-sliding contacts [45],[46]. Rolling-sliding contact is a result of the presence of traction between contacting bodies during rolling, while rolling contact has very little or no traction present. Rolling and rolling-sliding contact were discussed in previous text in section 6.1.

Fatigue is the phenomenon responsible for surface wear in RCF. Fatigue failure is defined as the "failure of material under the action of repeated stresses" [55]. Under rolling contact, stresses are generated due to the contact; and, as rolling proceeds the stresses at the surface and subsurface of the contacting bodies are cycled. The contact stresses are discussed in Chapter 3.2 while the material response and deformation regimes are covered in Chapter 6.2. Traction has an effect on the contact stresses and as a result affects the fatigue life of surfaces in contact. The effect of traction on the contact stresses is covered in section 6.2.6.

Research conducted on rolling contact fatigue can be divided into two fields of approach. The first is the mathematical and numerical modeling for the prediction of the position at which the fatigue crack will appear and as to the number of cycles at which a crack will initiate [38],[39]. The second is the experimentation conducted to observe rolling contact fatigue failures [42],[46]. The study of RCF is a continuously growing field of study with a large and growing number of proposed material models and fatigue failure parameters. The concept of rolling contact fatigue (RCF) is therefore covered here only to discuss the failure mechanism specific to two dimensional rolling contact.

As discussed in Chapter 6.2, the material response to rolling contact is governed by the stress level or load factor ratio (Po/k). Rolling contacts occurring at load factor ratios below the shakedown limit (Po/k < 4) will develop residual stresses and become elastic within a few stress cycles, however at larger load factor ratios plastic deformation and shear ratchetting strain will occur [27]. Both of these material responses are discussed in chapter 6.2.3. The rolling contact fatigue process is believed to the result of the shear strain ratchetting failure mechanism (RF). This has been suggested by numerous experimental findings [43]. For the frictionless contact of

an elastic-perfectly-plastic material model the shakedown limit is equal to four (Po/k = 4) [43]. Under rolling contact conditions at greater load factor ratios ratchetting material response is observed. Both ratchetting and plastic material response are covered in section 6.2.3.

Results from a simulation by Y. Jiang, H. Sehitoglu (1999) [39] further verified that the action of ratchetting as a material response is only significant above a load factor ratio of 4 (Po/k =4). The effect of ratchetting was identified to further increase with an increase in the load factor ratio. The simulation indicated a finite number of cycles ending in failure for load factor ratios greater than 4. The model used in the simulations predicted the number of rolling contact cycles to failure for load factor ratios between 4 and 8 [39].

P. Clayton, X. Su (1996) [42] conducted experimentation on steel under various load factor ratios (Po/k) and tractions. The test specimens were in the form of rollers and measurement of the ratchetting strain was conducted for the tests. Figure 7.5 illustrates the ratchetting strain measured. The figure illustrates the strain increasing with number of cycles and increasing with greater values of load factor ratio (Po/k). All the ratchetting was measured for values of load ratio of Po/k > 4. This further highlights the predicted value of Po/k ratio of 4 as the value above which ratchetting occurs. As mentioned it is the ratcheting material response which dominates RCF [42].
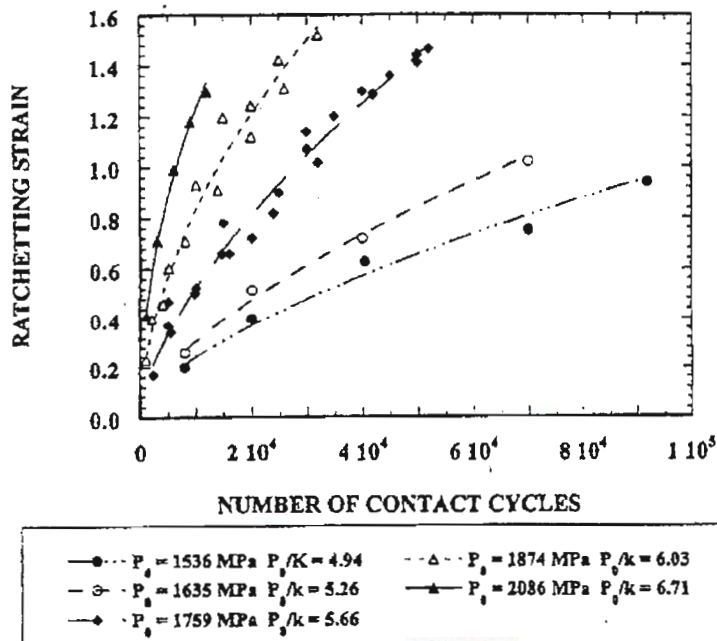
Figure 7. 5 Experimental ratchetting strain measurements [42]

Traction under rolling contact results in rolling-sliding of the contacting bodies. The amount of traction affects the shear stresses generated within the contact area. The effect of traction on the contact stresses is covered in section 6.2.6.

For pure rolling contact, the limiting value of load factor ratio above which ratchetting will occur and RCF will begin is the shakedown limit. However the presents of traction can cause ratchetting and RCF to initiate at load factor ratios less than the shakedown limit [42]. Stated differently RCF may cause failure in rolling contact at load ratios (Po/k) of less than 4 in rolling contact conditions with traction.

Figure 7.6 illustrates that in the presence of friction the elastic perfectly plastic shakedown limit is reduced with increasing friction. Therefore failure due to ratchetting or plastic flow may occur at load factor ratios of less than 4 in the presence of traction [42].
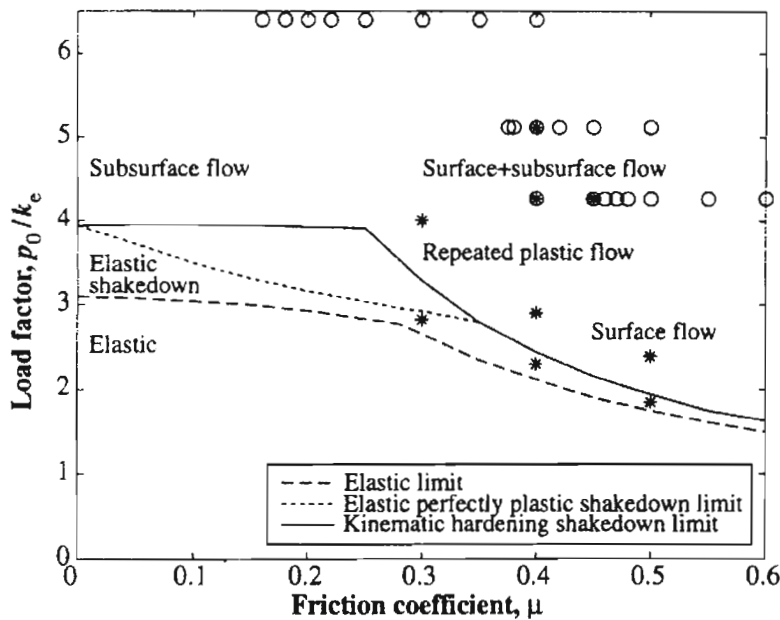
Figure 7. 6 Shakedown map (material response) [32]

The prediction of macroscopic fatigue failure is made further difficult due to the presents of imperfections in actual materials. Imperfections include aspects of physical metallurgy and micro cracks and other inclusions [56],[57].

Research by Ev.A. Shur, N.Ya Bychkova, (2005) [56] examined the relationship between RCF and the contacting bodies structure at a metallurgical level. It was shown that the greater the carbide content and the smaller the grain size the greater the resistance to RCF. The RCF life of a contacting body can also be improved with increased hardness and material purity [56].

7.3.2 Microscopic fatigue wear

As mentioned previously microscopic and macroscopic geometries under rolling contact conditions experience fatigue which results in the wear of surfaces. The macroscopic and microscopic geometries can be seen in Figures 7.2, 7.3, 7.4. Microscopic geometries (asperities) are a result of surface roughness. A large quantity of asperities can be found on most engineering surfaces as they are manufactured through machining.

Rolling contact wear is observed in the railway industry as wear on the surfaces of both wheels and rails. The wear is responsible for changes in the contact geometry [49]. Changes in the contact geometry effect stress distribution on a macroscopic scale and may therefore affect macroscopic fatigue, further highlighting the relationship between both macro and microscopic fatigue wear processes.

A further characteristic of microscopic fatigue wear is that it may lead to further surface wear and even accelerate wear once initiated. Researches R. Amed, M. Hadfield (1999) [33], reported that surface wear initiated from the generation of small debris (due to asperity contact) accelerated the wear process due to three body abrasion. Abrasion is discussed in Chapter 7.2.

The microscopic fatigue wear mechanism can be explained as follows: As two contacting surfaces are brought into contact, the asperities (non conforming geometries) of both surfaces touch. The surface asperities are then deformed. However due to the various height distributions, the contact stress magnitudes are different for each contacting asperity. The range of contact stress magnitudes can vary from a low level of elastic stress to the fracture stress of the material [13].

As a result of the contact stresses the asperities will be subject to one of two outcomes: asperities subject to contact stresses less than the fracture stress will experience one cycle of fatigue with every rolling pass, while asperities stressed higher than the fracture stress will be detached from the surface immediately as rolling contact commences [13].

As rolling contact continues, the remaining asperities will failure as a result of local surface fatigue fracture. The failed asperities will be observed as wear fragments. Microscopic fatigue wear can occur continuously during rolling contact as new asperities are formed at the fractured interfaces [13].
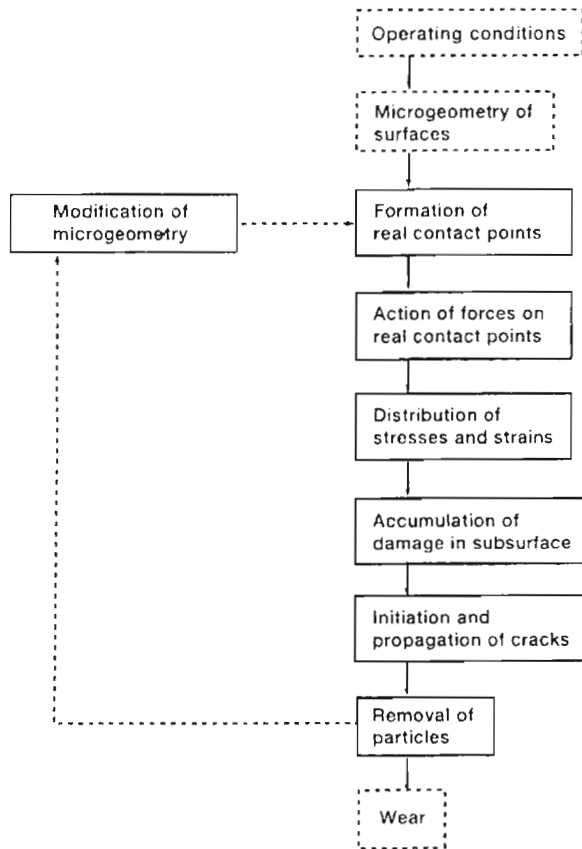
Figure 7. 7 Process of microscopic fatigue wear [52]

Microscopic fatigue results in the generation of wear particles through the removal of surfaces fragments. The analysis uses contact geometry well defined by hertz on the macroscopic level. The microscopic fatigue theories and analysis uses results form rolling contact fatigue (RCF). Microscopic surface fatigue may also result in geometrical changes of the surface on a macroscopic scale [52].

Figure 7.7 illustrates the fatigue wear process of micro irregularities. The operating conditions are the applied load and traction present while the micro irregularities are a result of surface finish. The contact points are then subject to cyclic stress resulting in fatigue. Cracks in the asperities are then initiated and propagate resulting in the removal of particles as wear. As particles are removed new asperities are formed which are then fatigued forming a loop [52].

Macroscopic fatigue under 2 dimensional rolling contact with no traction is predicted to occur for a load factor ratio of greater than 4 (fatigue = Po/k > 4 for pure rolling) as ratchetting and plastic shakedown occur [39] [43]. While no fatigue is predicted for load factor ratio of less than 4, microscopic geometries (asperities) may be stresses significantly more, resulting in localized ratchetting material response leading to microscopic fatigue. Therefore wear of a rolling contact

59

surface may be visible as a result of microscopic fatigue (wear) while macroscopic fatigue (spalling) may not occur [52].

The wear fragments produced as a result of microscopic fatigue often appear as flakes. The shape is the result of the fragments been rolled flat before leaving the contact area.

Testing and experimentation by P.Clayton, N. Jin (1996) [45] in which rolling contact was conducted on low/ medium carbon banitic steels under rolling contact, noted that RCF and wear were improved with increased initial hardness of the test specimens. In experimentation by M. Ueda, K. Uchino, A. Kobayashi (2002) [57], it was observed that wear rates were reduced with increased carbon content for pearlitic steels.

7.4 Rolling contact wear of coated surfaces

Contact stresses are approximately the same for both coated and uncoated surfaces. This is discussed in section 6.3. The cyclic nature of the contact stresses under rolling contact results in fatigue of the surfaces. All wear processes discussed previously act on both coated and uncoated contacting surfaces with the inclusion of delamination wear [34].

As a result of micro defects found in coated surfaces, stress concentrations are present. The defects may occur in the coating microstructure or the interface between coating and substrate. Cracks then initiate and propagate from the defects and lead to the failure of the coating though delamination. The cracks run adjacent to the contact surface and generally occur at the position of maximum shear stress [34].

Testing and experimentation ([34],[18],[58],[35]) by several researchers into rolling contact behavior of thermally coated surfaces, observed the wear mechanisms of adhesion, abrasion and fatigue.

8. Powdered metal coating processes

The aim of the presented research is to compare two powdered metal coating processes under rolling contact conditions. The coating processes are laser cladding and plasma spraying. The same composition of the metal powder was used for both coating processes. Surface fatigue and wear are both observed under rolling contact conditions.

Laser cladding and plasma spraying are surface coating methods. Both processes use powdered metal with the addition of heat to create a surface coating. However the application methods are distinctly different and as a result produce different coating properties. The differences are that of bonding mechanism and coating microstructure. Plasma spraying is a thermal spray application method while laser cladding is a fusion or welding process. As a result laser cladding creates a metallurgical bond between coating and substrate while plasma spraying produces a mechanical bond.

The effect of both wear and corrosion may be decreased by the addition of a plasma sprayed surface. The surface may also present sought-after thermal and electrical characteristics. Dimensional control and surface restoration may also be achieved [59]. Laser cladding produces surfaces with similar benefits and applications to that of plasma spraying.

Each of the coating methods have a wide variety of coating parameters which can vary. General processes parameters which vary are the composition of the substrate, powder composition and characteristics, feed rate of the powdered metal, application speed, part manipulation and gas flow rates. More specific process parameters for plasma spraying are heat generated in the plasma gun and application distance [60]. While for laser cladding, beam energy and powder application method are of importance [61]. As a result of the large variation of parameters for both application methods, the optimization of either plasma coating or laser cladding for any specific application can be viewed as a research field in itself.

The theory and application of plasma spraying can be found in text by R. Suryanarayanan [60]. The text covers an analysis of the of the thermal spray jet, the momentum and the heat and mass transfer experienced in the spraying process, the structure and properties of a number of specific plasma sprayed coatings and the application of plasma spraying for electronic materials. Research conducted by M. Schneider into Laser cladding with powder (1998) [61] gives an explanation and discussion of the laser cladding process parameters. The research covers a discussion on powder placement methods, temperature distributions effects on the substrate material and the laser power effect on coating.

While each of theses coating processes (Laser cladding and plasma spraying) can be research fields in themselves, presented in this chapter is a description of each coating method and an explanation of the nature of the coatings formed. The aim is to give a general overview of the two coating methods under investigation.

8.1.1 Plasma coating

The plasma spray process provides a coating using molten material. Powdered material is injected through a plasma flame where it is melted and accelerated towards the components surface. As the molten material contacts the surface it swiftly cools and solidifies forming a coated layer. The process is referred to as "cold" as the temperature of the substrate is cool in comparison to the coating material. The relatively cool temperatures maintained during coating prevent distortion and metallurgical changes of the substrate [62].

It is the generation of plasma which creates the high temperatures required to melt the powdered metal used in the coating process. Plasma is a state of matter like the three more commonly known states; liquid solid and gas. However, if substantial heat is added to any material an unstable state of plasma will form. Within plasma, electrons are removed from the atoms creating a 'gas' which is electrically conductive. Lighting bolts, Aurora borealis (The northern lights) and flames are examples of plasma occurring in nature [63]. Figure 8.1 illustrates the plasma coating process in operation.
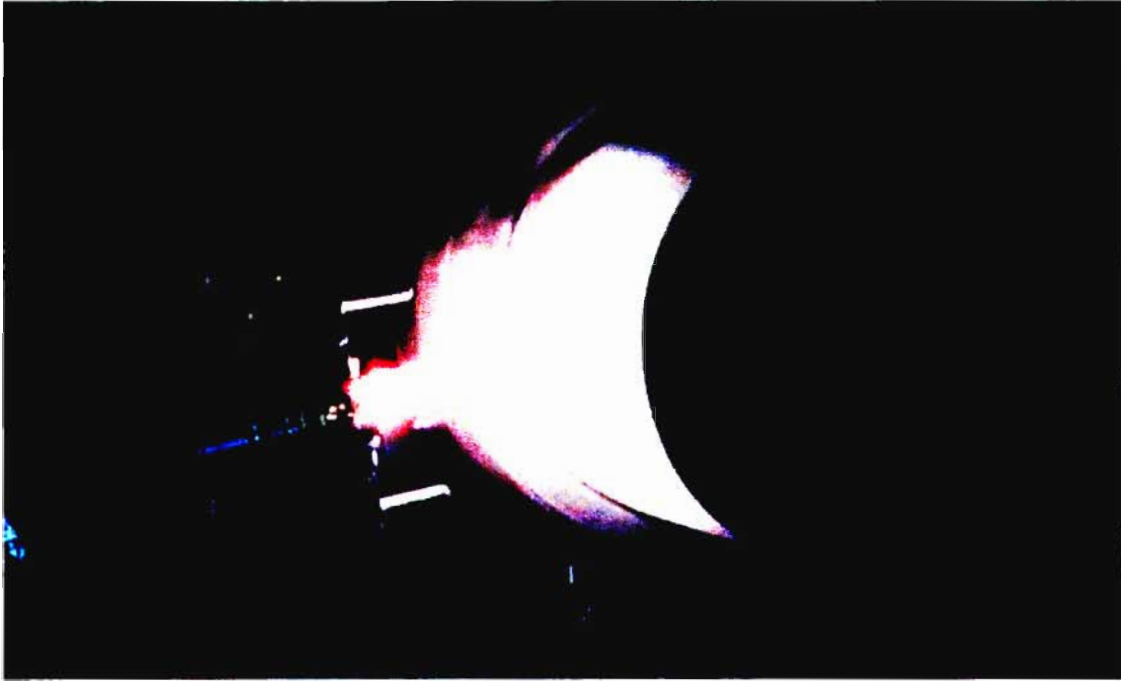
Figure 8. 1 Plasma spraying of a cylindrical component's surface [62]

Plasma spraying, HVOF (High velocity Oxy Fuel), Arc and flame spraying are all thermal spray process. Of these spraying processes plasma spraying is more accommodating due to the high energy of the plasma flame and the use of powdered material as a coating feedstock. The powder allows for a variety of coating materials to be used while the high temperatures of the flame is sufficient to melt most materials [59]

The generation of the plasma and melting of the powdered metal occurs within the plasma gun. Figure 8.2 illustrates the operation of the gun. A cathode and anode are housed within the gun, the orientation of the electrodes form a nozzle configuration with a small opening through which plasma gasses can flow. DC power is supplied across the electrodes (cathode and anode) which results in the formation of an electric arc. The plasma gasses under pressure are forced through the arc. Electrons are removed from the gasses atoms and unstable plasma is formed. As the atoms and electrons recombine back to form a gaseous state, thermal energy is released. The temperature of the resulting plasma flame or flume can be between 6,600°C and 16,600°C [59]. To prevent the nozzle of the plasma gun melting, water is circulated through the nozzle to provide the required cooling and prevent failure. Powdered coating material is injected into the high temperature plasma flume where it is rapidly melted and propelled toward the target surface. On contact with the target surface the material cools and solidifies forming a surface coating [59].

63
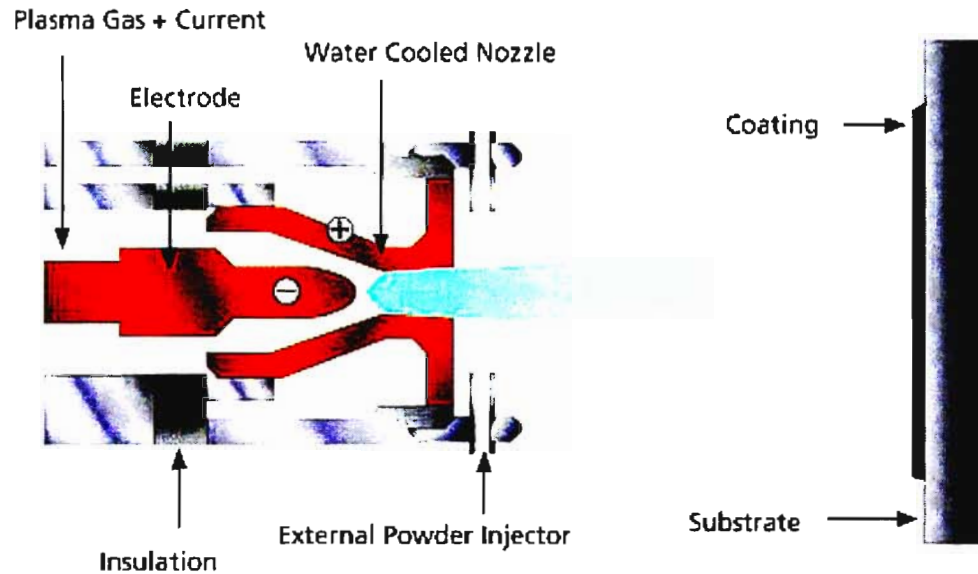
Figure 8. 2 The plasma spray gun [63]

Gasses used to generate plasma are generally a combination of two of the following; Hydrogen, Helium, Argon or Nitrogen. The selected gasses and the quantity of applied current control the amount of energy and temperature of the resulting plasma flame. Predictable and repeatable coating results can be obtained due to the accurate regulation and control of the following process variables; applied current, gas flow rates, the point and angle at which the material is injected and the distance from the gun to the components surface. A wide range of coating materials with various melting temperatures can be used as a result of this control and regulation [59].

The temperature of the target component surface is maintained and controlled by the relative speed between the plasma gun and the target component's surface. Compressed air is also used to reduce surface temperatures which are generally in the range of 38°C to 260°C [59].
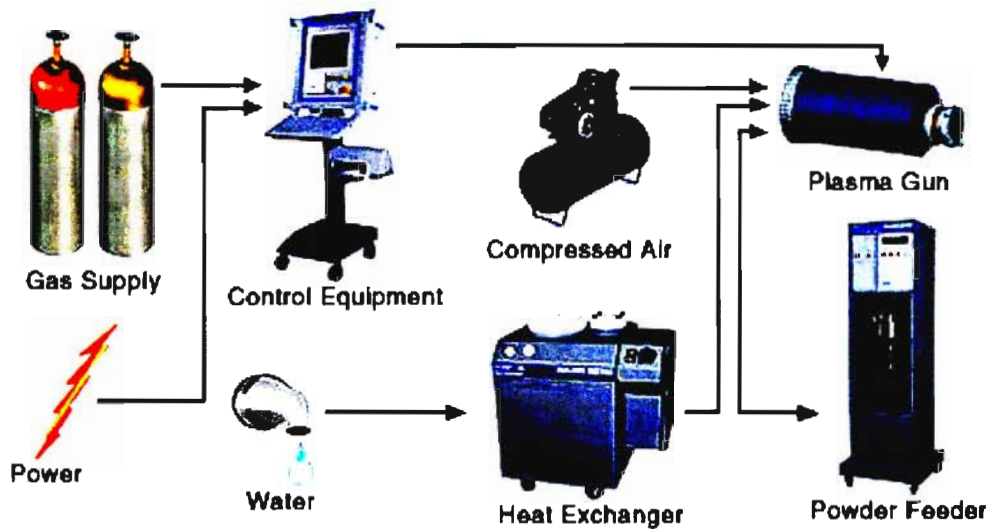
Figure 8. 3 Key components of a plasma spray system [59]

While it is in the plasma gun in which significant heat is produced and the metal powder melted; the spraying system is comprised of additional equipment, each performing a specific task and function. The important additional equipment is a powder feeder, heat exchanger, compressed air supply and control equipment. The function of the control equipment is to regulate both the power (DC volts) and the plasma gasses supplied to the gun. The powder feeder regulates the rate of powdered material input while the heat exchanger cools the circulating water which is passed through the gun for cooling during operation. The compressed air is supplied for the cooling the target surface. Figure 8.3 illustrates the key equipment and their functions in the spraying process [59].

The condition of a target surface is of significant importance; surfaces are generally cleaned and grit blasted prior to coating. Specific areas of the component which do not require coating are generally masked off during the blasting process [63]. Blasting removes oxide layers and creates a rough surface; as a result the mechanical coating adhesion between coating and substrate is improved. [64].

8.1.2 The nature of the coating

The high temperatures and particle velocities (200-300 meters per second) obtained during spraying produce good quality coatings [64]. The final coating thickness is built up in layers each deposited in separate coating passes. The coating structure in cross section appears therefore to be laminar or layered. The layered or laminar structure is characteristic of all thermal sprayed coatings. Each layer is constructed of melted powder particles which have flattened and solidified on contact with a surface. Sprayed material does not diffuse into the

substrate during coating. The structural properties of the coating are therefore affected by the thickness of each individual flattened particles and the interface bond between the layers/particles [60]. The resulting bonding mechanism is mechanical. Figure 8.4 illustrates the deformation of a molten powder particle on contact with a component's surface [62].
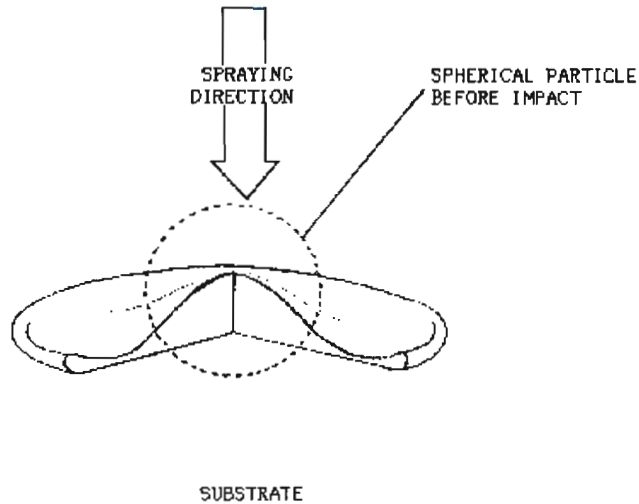
Figure 8. 4 A thermally sprayed spherical particle impinged onto a substrate [62]

The interfacial bonds between coating layers/particles and therefore of the entire coating is largely effected by; spraying distance, gas entrapment, particle temperature and velocity. If the spraying distance is to large the liquid droplets may cool and be partially solidified on contact with the surface. The same result will occur should the particle temperature or velocity be to low leading to a weak interfacial bonding. Gasses can become entrapped between particles/layers resulting in the formation of voids further reducing bonding strength [60].

Oxidation of the spray material may occur as air becomes caught up in the spray stream. The entrainment of surrounding atmosphere cools and slows the spray stream further reducing the quality of the coating [64]. Figure 8.5 and the microstructure picture (Figure 8.6) illustrate the composition of a coating. Within the laminar structure, voids, oxide inclusion and un-melted particles are visible [62].

66
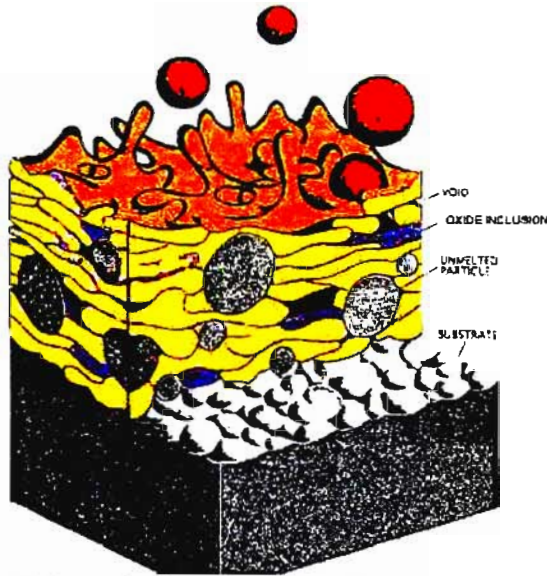
Figure 8. 5 Schematic diagram of thermal spray metal coating [62]
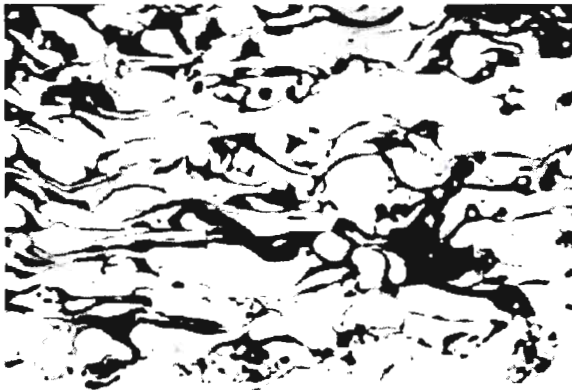
Figure 8. 6 A typical microstructure of a metallic sprayed coating [62]

Comparison of particle velocities, coating adhesion, oxide content and coating porosity of thermal spray application methods is illustrated in the following table [64]. It is noted that the adhesion of the plasma coatings is less than that of HVOF coatings; this is a result of lower particle velocities. The lower particle velocity has the effect of increasing the presents of porosity and oxide content when compared with HVOF. However plasma spraying is one of the better thermal spray methods when compared with either arc or flame [64].

Table 1 Characteristics of thermal spray coatings [64]

Process	Particle Velocity (m/s)	Adhesion (MPa)	Oxide Content (%)	Porosity (%)	Deposition Rate (kg/hr)	Typical Deposit Thickness (mm)
Flame	40	<8	10–15	10–15	1–10	0.2–10
Arc	100	10–30	10–20	5–10	6–60	0.2–10
Plasma	200–300	20–70	1–3	1–8	1–5	0.2–2
HVOF	600–800	>70	1–2	1–2	1–5	0.2–2

8.2.1 Laser cladding

The laser cladding process uses substantial heat and energy to metallurgically fuse an alloy to a substrate, the transfer of heat is rapid and localized to one specific area on a surface at any one time [65]. The energy and heat required is generated using a LASER, the defined of which is a Light Amplification by Stimulated Emission of Radiation [66].

The goal of cladding is to deposit a material of desired physical properties over a substrate. Cladding materials are chosen based on whether they need to provide corrosion resistance, wear resistance or higher hardness, depending upon the final application of the component being clad. Due to the coating modification an ordinary and possibly less expensive base material can be used to manufacture the main component [61].

Surface cladding is generally performed either by laser and conventional welding. Both processes provide a good metallurgical bond between coating and substrate. However laser cladding compared to conventional welding provides better thickness control, this is a result of the precise control over the thermal input from the laser onto the components surface. The control of the thermal input prevents the base material properties from been detrimentally effected due to temperature and prevents distortion of the component/surface been coated [66].

The cladding material for conventional welding is limited to wire format while the laser process is compatible with all powdered metals and ceramics. The result is that the laser process is easier to automate than conventional welding as a cladding process [66].

As the properties of the clad surface and the underlying or substrate material can have different compositions and microstructures, laser cladding has found a wide range of applications [67]. In the aircraft industry for example, turbine blades can be both repaired and coated. A laser clad tip added to a blade produces a wear resistant edge, while the creep resistance of the blade material is not adversely affected. Laser cladding also has advantages over existing methods namely TIG welding. Specific advantages are that of higher quality and reproducibility of micro structural properties, improved turn around times, better volume capability and cost reduction. Distortion of the turbine blade is also reduced due to the lower and more controlled heat inputs [67].

Four important items are required to generate a laser clad surface; a laser, powdered material, shielding gas and coating surface. Clad surfaces are made up of a series of beads or weld tracks. Powdered material is melted and fused onto a substrate within a localized melt pool. A single track is the result of a continuously solidifying pool. These weld tracks are visible in Figure 8.7. Shielding gas is used during the cladding process to prevent oxidation of the melt pool [61].
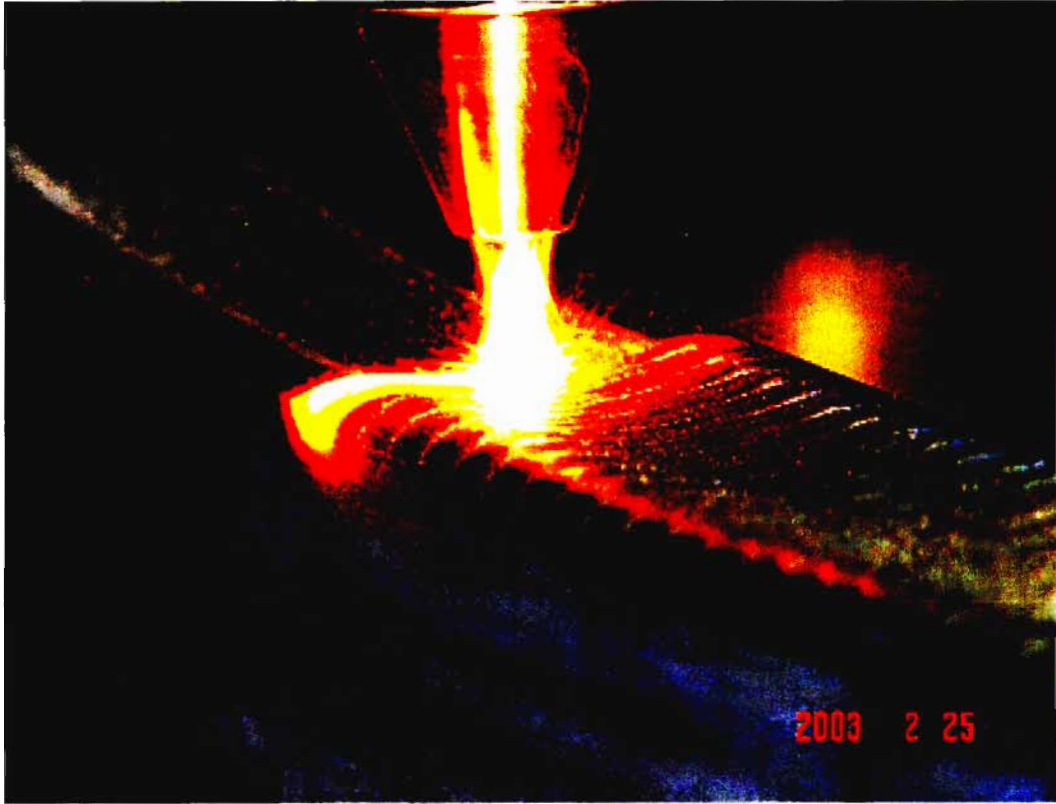
Figure 8. 7 The laser cladding process [66]

The powdered material can either be pre-placed on the components surface or added into the melt pool during the cladding progresses (in-situ). The pre-placed powder application method is referred to as two stage cladding while in-situ powder application is referred to as one stage laser cladding [61]. Figure 8.8 illustrates the two powder application methods [61].
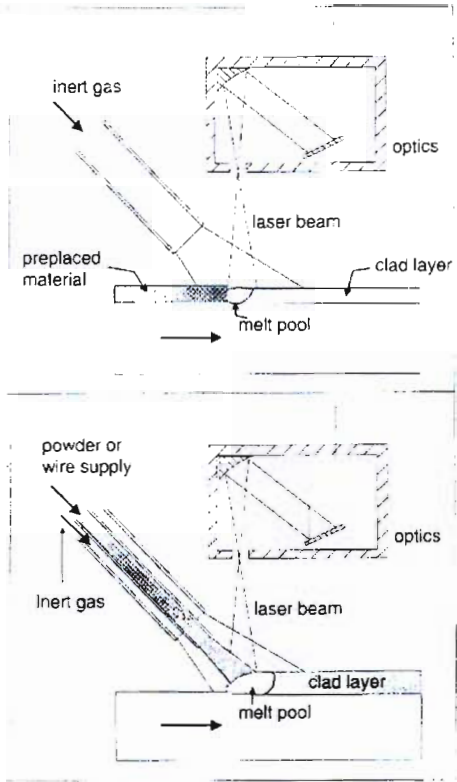
Figure 8. 8 Two stage (pre placed) and one stage (in-situ) laser cladding [61]

Two configurations for powder application are used in one stage (in-situ) laser cladding. The powder material can either be added laterally or co-axially in relation to the laser beam. Figure 8.9 illustrates the two powder supply configurations [61].
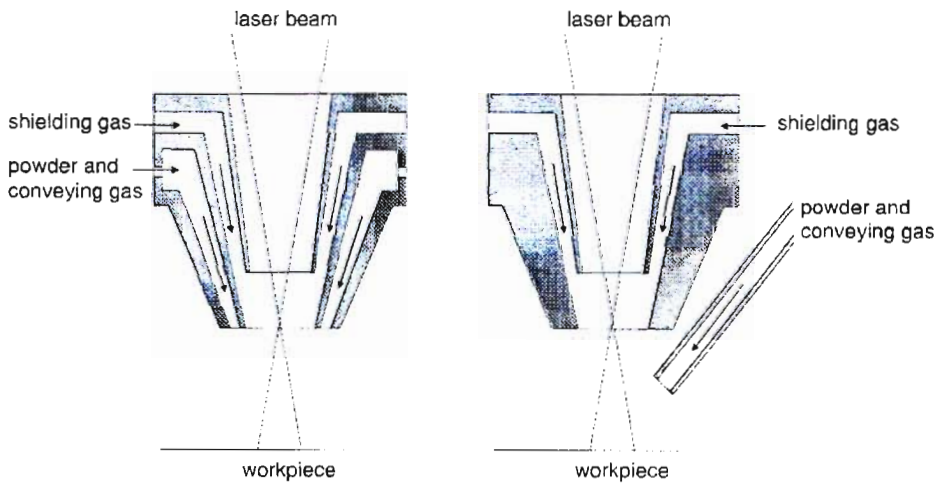
Figure 8. 9 Co-axial (left) and lateral (right) powder supply [61]

8.2.2 The nature of the coating

While the laser cladding process is discussed in the previous chapter, it is the nature and characteristics of the final clad surface which is significantly important. Coating characteristic such as dilution, bonding mechanism, cross sectional shape and porosity are presented here. The process parameters which cause or affect these characteristics are also discussed.

Laser cladding is generally applied to a surface in a single layer. The layer is comprised of a series of weld tracks which are the result of a continuously solidifying melt pool during cladding. The melt pool consists of molten powdered metal and substrate material. To utilize the coating properties fully, mixing between the coating and substrate is kept as low as possible during fusing, while not reducing the interfacial bond strength after solidification has occurred [61]. The quantity or amount of intermixing between clad material and substrate is referred to as dilution. High dilution results in an alloying of a surface, the alloy been a combination of the clad and surface materials. A low dilution clad surface is desirable, the base material properties are not adversely affected by the additional coating and the full benefit of the clad surface can be achieved and utilized [61].

A quality deposited layer can be achieved by good manipulation and control of the melt pool. The size and shape of the pool is effected by; gas flows, laser beam energy, part manipulation and powder characteristics [67]. The cross sectional shape and properties of the clad are dependent on a number of parameters such as the powdered material characteristics, composition, shielding gas flow rate and beam energy. The beam energy is significant in the amount of heat generated during cladding and is affected by the feed rate of the component and the beam power density. The powder characteristics (composition and grade) affect the resulting microstructure after solidification. While the shielding gas flow rates effect the aspect ratio of the clad [67].

1) Alloying.   2) Correct structure.   3) Poor Bonding.
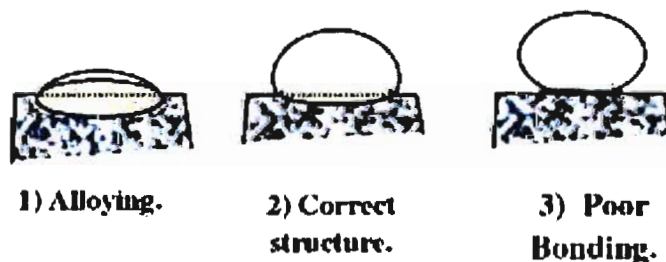
Figure 8. 10 Penetration of laser cladding [67]

The Figure 8.10 illustrates the types of bonding which laser cladding can produce. The beam energy and resulting cladding temperatures effect the clad layer produced. The third figure illustrates the effect of to little energy. The energy is insufficient to melt the powder and substrate and poor adhesion is the result. The second figure illustrates the ideal energy input. The interface bonding is good with very low dilution. If the energy during cladding is to high dilution and alloying between coating and substrate occurs, this is indicated by the first figure [67].

Some laser clad coating may have voids or small holes present at either the interface between the coating and substrate or within the coating or clad layer. The holes or voids are referred to as porosity [61].

The entrapment of gas bubbles and differential cooling rates of clad regions are believed to be responsible for the formation of porosity within the coating or clad layer. Therefore the porosity is due to solidification complications. Porosity found between the substrate and the clad layer is the result of the coating over minor surface flaws or inclusions (grease or dirt) [61].

A further type of porosity is found between the overlapping cladding runs. This type of porosity occurs when to much power is supplied by the laser to each individual melt pool. The porosity is referred to as inter-run porosity. The porosity can be avoided if the width to height ratio of the clad layer is greater than 5 [61]. Inter-run porosity is illustrated in Figure 8.11 and is characterized by the formation of voids between runs or weld beads.
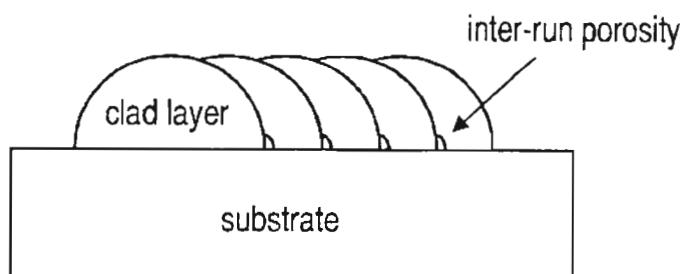
Figure 8. 11 Coating made of multiple layer runs [61]

72

9 Testing and Experimentation

The aim of the research was to investigate the rolling contact performance of two coating processes and two separate powder compositions applied to British standard En 9 steel. The test specimens were manufactured and coated using laser and plasma coating methods. Two different powdered metal compositions were used for each of the coating processes. Rolling contact fatigue tests were performed to obtain comparative results between the coated and uncoated test specimens and between the coating compositions for a given coating process. The tests were conducted under non lubricated 2 dimensional pure rolling contact conditions, at various contact stresses. The contact stress for any given test was calculated using a matlab program discussed in Chapter 4 in the current work.

Under rolling contact, material is removed from the surface of contacting bodies; the rate of removal of the material is the focus of this investigation. The exact mechanism of failure of the surface is a combination of the two phenomenon: wear and surface fatigue. Failure of the test specimen as a result of surface fatigue was identified as a sudden collapse or fracture of the surface or coating after a critical number of rolling contact cycles. Wear (fatigue wear) was identified as a continuous removal of surface material during rolling contact. Both of these mechanisms are discussed in Chapter 7 of the presented work.

Table 2 shows the compositions of the two powdered metals applied both using plasma spraying and laser cladding. Batch No. 1434/05 is referred to as composition 1 while batch No. 1435/05 is referred to as composition 2. In the table the top row of letters refer to the elements abbreviations (Ni –nickel etc.) while the numbers below represent the percentage concentration for a given powder composition. The plasma spraying was performed by a local company called Ceramic Anilox Engravers (CAE), while the laser cladding was conducted by the National Laser Center base at the CSIR (Center for Scientific and industrial research). The two powders were selected due to differences in composition. While the quantities of silicon and carbon are similar and the amount of manganese is slightly greater in composition 1, it is the presents of other elements which make the compositions distinctly different. Table 2 illustrates the presents of Nickel and Molybdenum in composition 1 while Chromium, Tungsten and Vanadium are present in composition 2. Of the initial four powders purchased the two used for the research were the most distinctly different.

Table 2 Chemical compositions of metal powders

Ni	Mo	Cr	Si	C	W	Mn	V	Fe	Batch No.
3.8	0.28		0.24	0.22		0.86		Balance	1434/05
		0.5	0.26	0.22	0.55	0.13	0.19	Balance	1435/05

The coated and uncoated En 9 test specimens were tested using a specifically designed rolling contact test machine. Through testing and evaluation, the response to rolling contact of the coated test specimens were evaluated against one another and the uncoated steel under rolling contact. The performance of the coating compositions were also evaluated against one another for a given coating application process. Results used to determine the performance of the coatings and coating processes were, the number of cycles to failure and the wear rates of the coated surface.

For each specific rolling contact test performed a number of measurements were made. The number of rotational cycles of both specimen and running disc were counted, this data was used to calculate slip ratios, velocities of both discs and cycles to failure. The applied force and contact geometries (diameter and contact width of test specimens) were also measured for the calculation of Hertz contact stresses. The rolling resistance was also measured to evaluate the amount of traction present. The specimen diameters were measured to determine coating thickness and rate of surface wear (diameter changes). Microstructure pictures of the coated surface were taken prior to testing and following testing, and used to visually inspect the effects of the rolling contact on the surfaces. The pictures taken were of the cross sections of the surface and substrate, this allowed for the visual inspection of both the coating and subsurface. Any damage and deformation of the microstructure due to the effect of contact stress acting on the contacting interface was observed and noted.

The small subscript numbers in the following section refer to the specific technical specification of equipment, components and instrumentation used in the testing process. Further details are found in section 9.3. All test specimens tested were machined from the same 100 mm diameter EN9 steel.

The specimens were divided into 3 groups each consisting of 4 test specimens. The first group of specimens remained uncoated while the other 2 groups were coated using laser and plasma coating methods. Within each of the coated groups two specimens were coated using composition 1 and two specimens with composition 2.

The four test specimens from each group were machined down to a reduced contact width. Two specimens of 10 mm and 2 x 5 mm contact width were machined. The contact width was reduced to increase the contact stress at which the tests are conducted. Each test specimen was number punched to allow for accuracy in data logging. Referring to Figure 9.1, test specimen 1 was then fixed to the shaft using a locking element 10.1. Bearings 10.2 mounted on the shaft to

allow for free rotation of the shaft and the test specimen. The complete assembly is referred to as the specimen assembly and is tested as a unit in the rolling contact test machine.

The components shown in Figure 9.1 make up the specimen assembly while Figure 9.2 is a photograph of the assembly. The reduced contact width of 10 mm is visible in Figure 9.2.
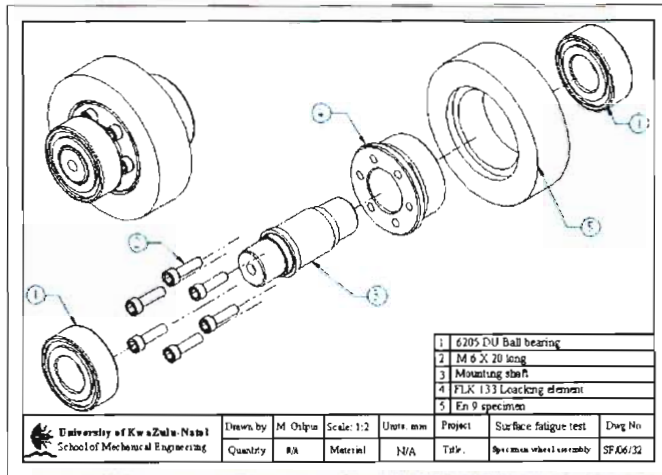
Figure 9. 1 Exploded test specimen assembly

Figure 9. 2 Complete test specimen assembly

The En 9 test specimens tested were referred to as test specimens 1, 2, 3 and 4 for the contact stresses of 300, 500, 700 and 900MPa respectively. The En 9 substrate was tested first to create a benchmark for the coated specimens to be tested against. Four En 9 specimens were uncoated while Four specimens were coated using each of the application processes. The coated specimens were tested under similar hertz contact stresses to that of the uncoated specimens.

En 9 steel is used in the manufacture of numerous mechanical components and some machined parts requiring wear resistance. Examples include small gears, keys, cylinders, shafts, rifle

barrels and machine tools. Harding may be achieved using an induction process, however care must be taken during hardening to obtain the desired properties [68].

The ultimate tensile strength and yield stress of normalized En 9 are approximately 700 MPa and 340 MPa. Using equation 22 in Chapter 6.2, the approximate value for the simple shear yield stress can be calculated as 200 MPa. As discussed in Chapter 6.2 the ratio of Hertz contact stress (Po) divided by yield stress is simple shear (k), is referred to as a load factor ratio (Po/k).The load factor ratio is also often referred to as the normalized Hertz contact stress. The value of the load factor ratio will determine the material response behavior for a given rolling contact condition.

The tests conducted at 300 MPa (Po/k = 1.5) and 500 MPa (Po/k = 2.5) fall within the elastic material response regime as the stresses are below the elastic limit (Po/k = 3.1). The test conducted at 700 MPa (Po/k = 3.5) falls within the elastic material shakedown regime as the load factor ratio is below the shakedown limit (Po/k=4) but above the elastic limit (3.1<Po/k <4).The material response for the test conducted at 900 MPa (Po/k = 4.5) is plastic shakedown and ratchetting. The material response, deformation regimes and limiting values are discussed in Chapter 6.2. Figure 9.3 illustrates graphically the above described behavior for the test conditions.

En 9 Benchmark
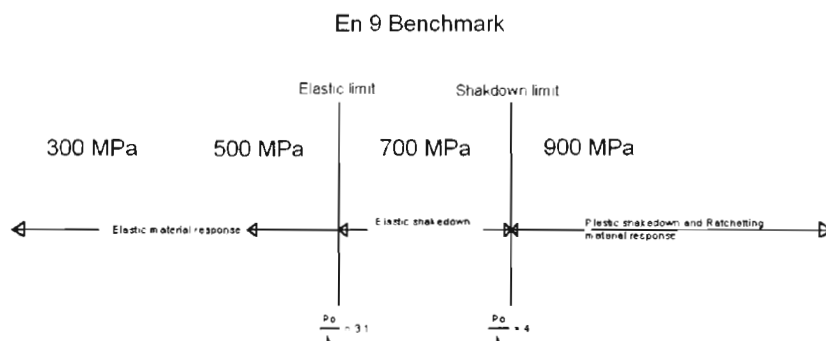
Figure 9. 3 Contact stresses and material responses

The En 9 test specimens were coated using two application methods (Plasma and Laser) and two coating compositions were coated using each of the application methods. A total of 8 specimens were coated. The coated surfaces were then ground to produce the required coating thickness and surface finish. The as-coated coating thicknesses of the laser and plasma specimens were 1 and 0.5 millimetres respectively. A recommendation by the application company (CAE) was that the final coating thickness for the plasma specimens be 0.1 mm. This coating thickness was found to be common with other plasma coated specimens tested in similar research [35]. The plasma coatings were reduced to 0.1 mm thickness; 20% of the original as-

coated thickness (0.5mm). Reducing the thickness of the laser clad coatings by the same percentage resulted in a coating thickness of 0.2 mm.

With reference to the discussion in Chapter 6.3, the Hertz contact stresses calculated for the coated and uncoated test specimens are assumed to be the same. The contact stress for the coated test specimens were calculated using the same matlab program discussed in previous text for the uncoated specimens.

The plasma coated test specimens were tested at Hertz contact stresses of 300 MPa and 500 MPa, while the laser clad specimens were tested at 500 MPa and 700 MPa. Both separate powdered metal compositions were tested at these stress levels for each of the coating application methods. The common contact stress between the laser and plasma tests was therefore 500 MPa. Some plasma tests were conduced at a lower contact stress of 300 MPa as the bonding mechanism between coating and substrate is mechanical in nature and is suspected to be less durable than the laser clad test specimens tested at 700 MPa.

No coated test specimens were tested at 900 MPa contact stress only one En 9 specimen was tested at this stress. Testing of all coated specimens at a contact stress of 500 MPa resulted in an overlap of rolling contact conditions which allowed for direct performance comparisons to be made.

The 8 plasma and laser coated test specimens tested were referred to as PC1300, PC1500, PC2300, PC2500. LC1500, LC1700, LC2500, LC2700. The first letter refers to the coating application process (Plasma or laser). The second letter and third number refer to which composition the specimen was coated (C1 composition 1 or C2 composition 2). The final number at the end refers to the approximate Hertz contact stress (Po) at which the test was conducted. Figure 9.4 and 9.5 illustrate graphically the generation of the test specimens for the testing of both laser and plasma.

```
                          Laser cladding
                               |
          ┌────────────────────┴────────────────────┐
          |                                          |
    Composition 1                            Composition 2
          |                                          |
    ┌─────┴─────┐                            ┌───────┴───────┐
    |           |                            |               |
500 MPa      700 MPa                     500 MPa          700 MPa
(LC1500)     (LC1700)                    (LC2500)         (LC2700)
```
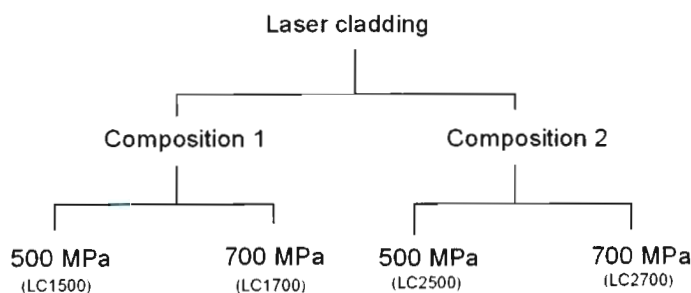
Figure 9. 4 Laser cladding contact stresses

```
                        Plasma spraying
                              |
          ┌───────────────────┴───────────────────┐
     Composition 1                            Composition 2
          |                                        |
   ┌──────┴──────┐                          ┌──────┴──────┐
 300 MPa       500 MPa                    300 MPa       500 MPa
 (PC1300)      (PC1500)                   (PC2300)      (PC2500)
```
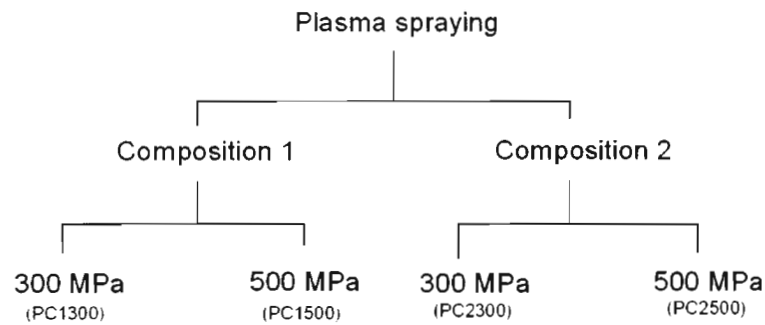
Figure 9. 5 Plasma spraying contact stresses

9.1 Testing equipment

For the experimental regime described in the proceeding section the following equipment was required, a rolling contact machine, grinding station and measurement devise. The following is a description of the equipment and operation. The subscript numbers following specific equipment reference further details in section 9.3. The numbers identify the equipment seen in the figures within the text.

9.1.1 Rolling contact test machine

The rolling contact test machine was designed and custom built for the project, the text that follows describes the machine operation, components, equipment and measurement methods used in the investigation/testing process.

9.1.2 Machine operation

The test machine was designed with symmetry (Axis ZZ) allowing for the testing of 2 test specimens to be conducted simultaneously. The tests can be conducted at different stress levels due to the separate loading arms.
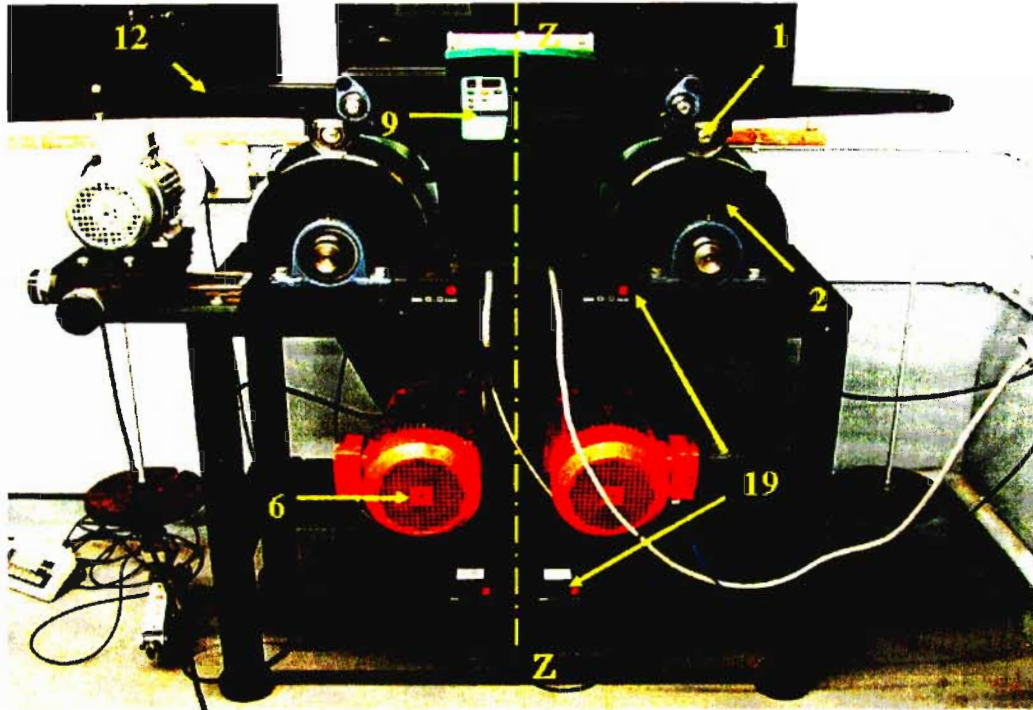
Figure 9. 6 Rolling contact test machine

The operational concept of the surface fatigue machine is simple, as it involves the rolling of two wheels on one another under load. The two wheels used in the investigation are the test specimen $_1$ and the main rotating disc $_2$. The diameters of the two discs are different. The diameters of the main rotating disc and the test specimen are ±350 and ±100 millimeters respectively. The diameter of both discs will vary slightly depending on the coating thickness applied to the test specimen and the amount of material removed during the grinding of the main rotating disc.

While the test specimen is measured, observed and changed during and after every 1000 000 cycles the main rotating disc is not. The removal of this disc from test machine for machining can cause a number of alignment complications when reinstalled later. It is for this reason that the disc is surface ground while remaining in mounted position on the testing machine. The grinding operation is performed using the specifically designed grinding station 3.

The torque required for the test is applied to the main rotating disc. This disc remains permanently shaft mounted on to the machine. The shaft and bearings 4 are housed in plumber block bearing housings 5. The drive for this disc is provided by a Flange mounted AC Electric motors 6 through a gearbox 7 and belt drive 8. Speed in revolutions per minute of the electric motor and therefore the disc is controlled using a Frequency controller 9.

The test specimen is mounted on a shaft with bearings. The complete assembly is referred to as the specimen assembly 10. The specimen assembly is placed into bearing cups 11 which are connected to the loading arm 12.

9.1.3 Force application and measurement

In order to generate a contact stress between the test specimen and the main rolling disc a normal load (L) is applied to the contacting interface. A loading arm is used to apply the load to the specimen assembly and this load generates the stresses at the interface between the test specimen and the rotating disc. The loading arm is illustrated in Figure 9.7.
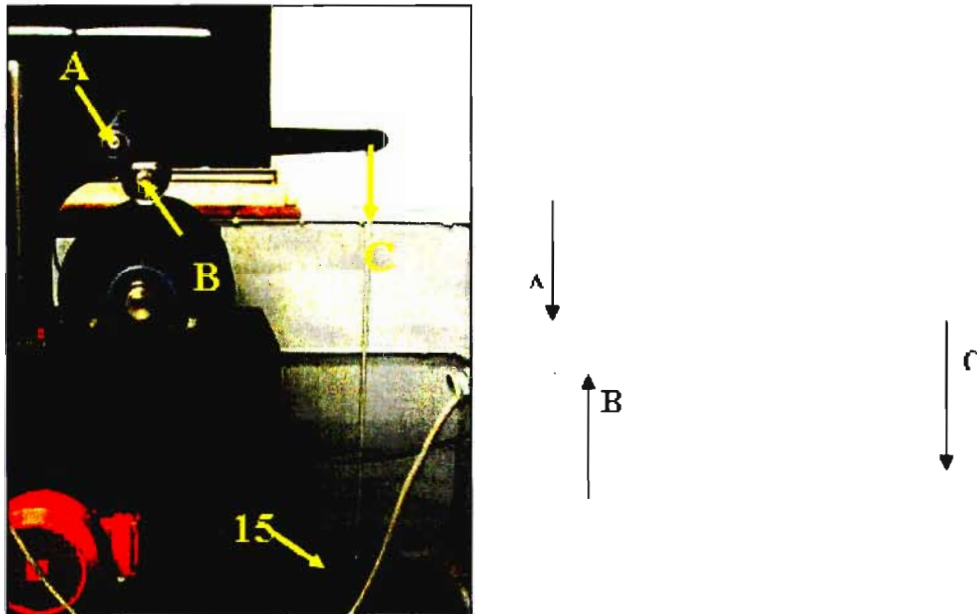
Figure 9. 7 Loading system

The loading arm is pivoted at point A with bearings $_{13}$ mounted to a shaft. The bearings are mounted in bearing housings $_{14}$ at position A. The bearings allow the loading arm to rotate up and down. The rotation allows the test specimen to be removed easily during testing. Mass pieces are added to the loading arm to generate the force required.

The mass of the loading arm with the addition of Mass pieces 15 is measured using a screw jack 16 mounted with a load cell 17. The force generated in the load cell is displayed on a readout 18. The screw jack, load cell and readout are visible in Figure 9.6. The force measured by the load cell with the loaded arm fully supported is the force generated at point C. The force generated at point B (At the test specimen) is 10 times larger due to the ratio of the loading arm pivoted at pivot point A.

The horizontal distance between points A and C is 500 mm while the distance between A and B is 50 mm. The force generated at B due to the applied load at C is 10 times greater due to the sum of moments about pivot A.

9.1.4 Cycle counting

The counting of cycles completed by the test specimen is measured using proximity counters [19]. The switching sensor for the counter is an inductive proximity switch [20]. The switching system allows for non contact cycle counting. The measurement pickup for the inductive proximity sensors is the head of a M5 cap screw. The screw is threaded into a tapped hole situated in the side of the test specimen at a radius of 35 mm. The cap screw rotates with the test specimen and is counted upon passing the sensor.

The counting of cycles of the main rotating disc is achieved using the same system as the cycle counting of the test specimen. However the measurement pickup for the proximity sensor is eight M 12 X 1 cap screws. These screws are located near the centre of the disc and are evenly spaced. Eight counts are completed for every revolution of the disc. Therefore division of total counts measured by 8 is a measure of the total disc revolutions.
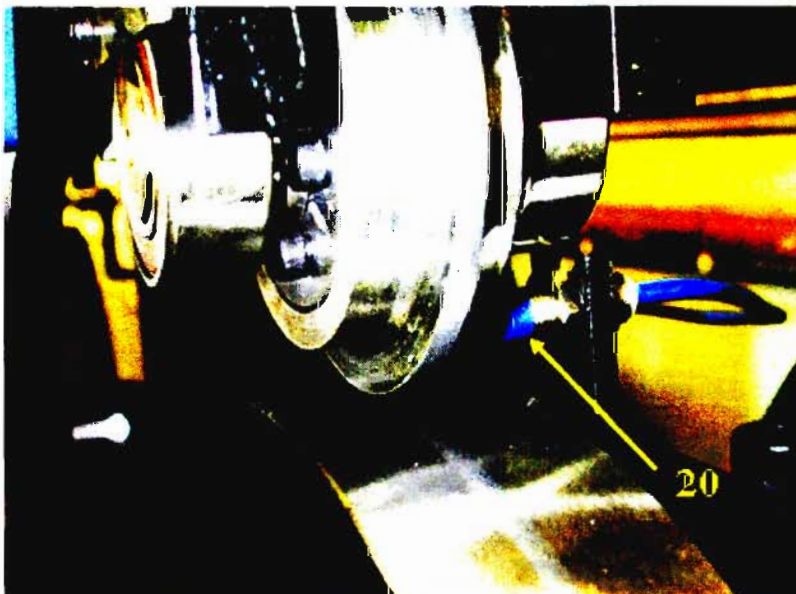

Figure 9. 8 Contact between specimen and main disc

9.1.5 Speed measurement

The frequency controller is fitted with a digital speed display of the motor speed. This speed measurement can be multiplied by the drive ratios (Gearbox, Belt drive and difference in the wheel diameters) to determine the operating speed of the test specimen. However the measurement is approximate due to slip in the belt drive etc. Therefore the speed of the test specimen during testing is calculated using the number of revolutions/cycles completed by the test specimen and the time taken to complete them. The operating speed during the tests remains constant at ±500 rpm. The speed is used for all tests as a standard.

9.1.6 Measurement of slip/Creep

The measurement of the quantity of slip between the main rolling disc and the test specimen is determined using the difference in the velocities for the two rotating wheels. The velocities of the test specimen and main rotating disc are calculated using the cycle counting method explained previously.

9.1.7 Measurement of rolling resistance (RR)

Rolling resistance is a measurement of the force required to rotate the test specimen assembly. This value is obtained by subtracting the forces required to rotate the main rotating disc with and without the loaded test specimen. The force is measured using a length of builders line [21] attached to the periphery of the Main rotating disc. A force is then applied to the end of the line. The force is generated by the addition of mass pieces applied to a mass hanger connected to the end of the line. The mass pieces are added to the hanger until the main disc rotates.

The mass pieces and hanger are then weighed using a scale [22]. The mass measurement obtained is multiplied by gravitational acceleration (g) to obtain a force. This process is repeated for both the loaded and unloaded disc.

The difference in the applied forces is a measurement of rolling resistance. Measurement of rolling resistance is conducted before every test. The rolling resistance is the amount of force which is transmitted between the 2 discs during operation. Figure 9.9 and 9.10 illustrate the measurement method while the following calculations are used to determine the quantity.
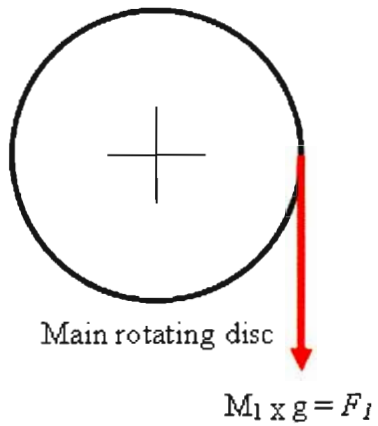
Figure 9. 9 Measurement step 1
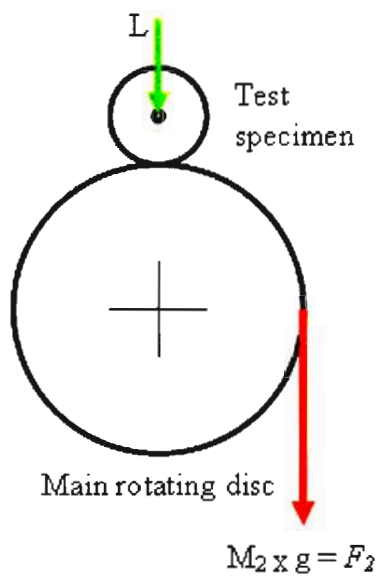
Figure 9. 10 Measurement step 2

L = Applied load (N)

g = Gravitational acceleration

Measurement step 1:

$F_1 = M_1 \times g$

F_1 = Drive resistance to rotation and bearing friction

Measurement step 2:

$F_2 = M_2 \times g$

$F_2 = F_1 + Rr$

Rr = rolling resistance

$$F_1 + Rr = M_2 \text{ X g}$$

$$(M_1 \text{ X g}) + Rr = (M_2 \text{ X g})$$

$$Rr = F_2 - F_1$$

$$Rr = (M_2 \text{ X g}) - (M_1 \text{ X g})$$

$$Rr = g (M_2 - M_1)$$

9.1.2 Diameter measurement

The diameters of the test specimens is measured after machining, following coating, grinding and during testing. These measurements are taken to determine coating thickness and surface material removed (wear rates) during testing. The diameter measurements are conducted using a mounted micrometer spindle [23], illustrated in Figure 9.11.
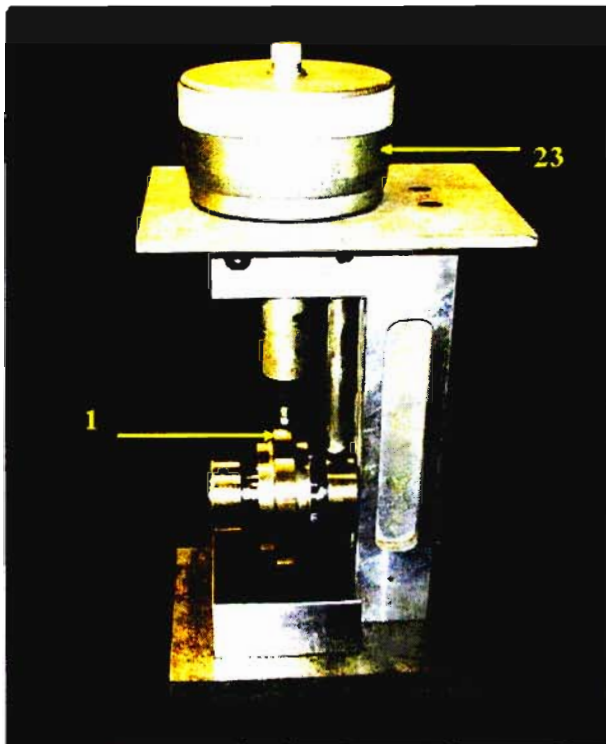
Figure 9. 11 Diameter measurement equipment

9.1.3 Grinding station

In order to obtain a consistent surface finish and remove the effect of surface wear on the main rotating disc, the testing surface is ground prior to each sample test.

The grinding process is conducted using a grind stone $_{3.1}$ rotated at 2740 revolutions per minute by an electric motor $_{3.2}$. The grind stone is mounted to the motor with a specifically designed attachment $_{3.3}$. The motor is mounted to a 2 axes bed $_{3.4}$. The function of the bed is to allow the grind stone to traverse the width of the disc and to adjust grinding depth. Figure 9.12 shows the grinding station and components. The white arrows illustrate the directional movement of the grinding station.
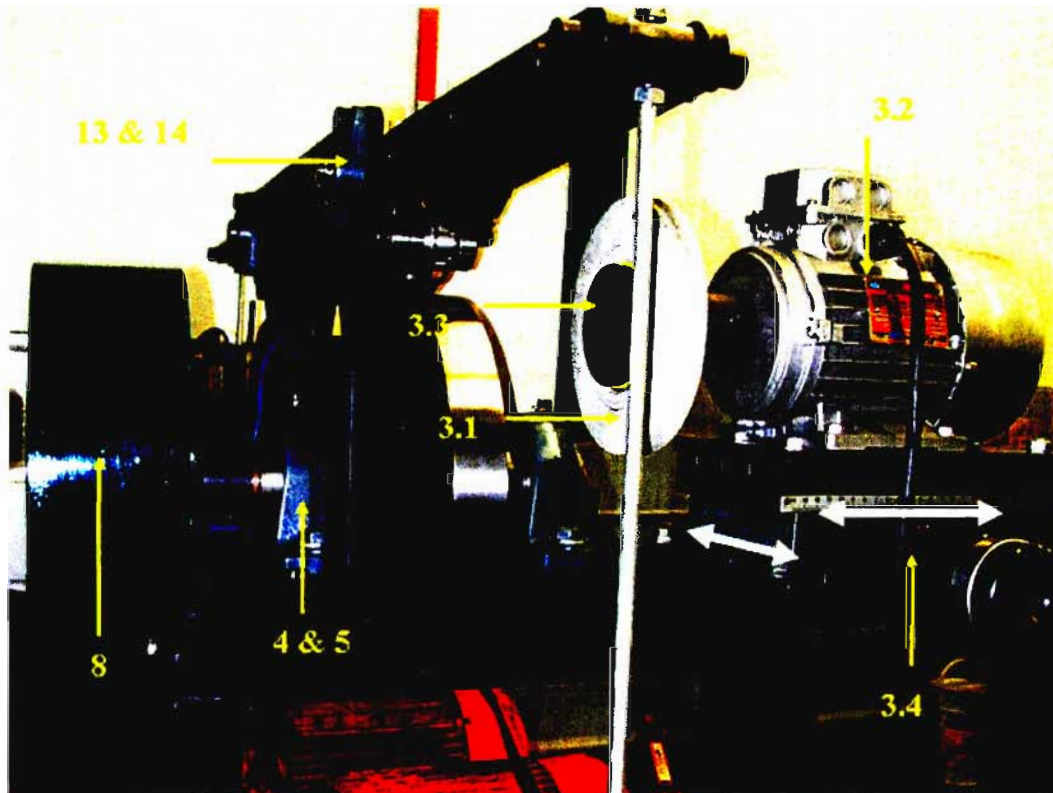
Figure 9. 12 Rolling contact test machine 2

In order that the main disc in ground correctly and accurately in position the following steps are followed:

The bed of the grinding unit is accurately aligned with the surface of the main rotating disc. This alignment is conducted using a square and a clock gauge.

Following the grinding operation the ground surface is clocked up to check the surface for accuracy. This is done to prevent the grinding of a taper on the running surface. A taper would have an adverse effect on the test results as one side of the test specimen would experience a greater contact pressure than the other.

9.2 Testing procedure

The following text is a description of the procedure followed in the testing of all tests specimens. The procedure involved the tasks and measurements performed prior to, during and after the testing.

Prior to testing the test specimen in the specimen assembly was cylindrically ground between centers. The grinding operation was performed using a cylindrical grinder [29]. The grinding of the test specimens assembly was conducted to achieve two objectives. Firstly grinding allowed for a consistent surface finish to be obtained for all specimens tested, both coated and uncoated prior to testing. Secondly grinding allowed the outer surface of the test specimen to rotate with accurate concentricity about the axis of the shaft and therefore reduce any vibration during testing. The main rotating disc mounted on the test machine is also surface ground using a specifically designed grinding station.

Following grinding, the diameters of each test specimen and main rotating disc were accurately recorded. The diameter measurements were used for the calculation of the coating thickness for each of the coated test specimens, the calculation of the contact stress under which each specific test was to be conducted and as an initial diameter measurement prior to testing. Each specimen was clearly number stamped for accurate identification.

Using the contact geometry of the main rotating disc and the test specimen, the load required to generate the contact stress for each test specimen was calculated. The calculation was performed using the matlab programme discussed in Chapter 4. The magnitude of the force required at the end of the loading arm was then determined.

Prior to inserting the test specimen in to the rolling contact test machine, a cap screw was inserted into the side of the specimen and the contacting surfaces were cleaned with ethanol to remove any oil, contaminants etc. The head of the cap screw was used as a pickup for the proximity counter. One cycle for the test specimen was counted for each rotation of the cap screw. The cycle counters for both the main rotating disc and the test specimen were then zeroed. The cycle counters were used to monitor both speed and slip during testing. Before each test the rolling contact resistance for the test specimen was measured.

During testing the test specimens were initially removed and diameters measured at approximately 30000, 60000 and 100 000 cycles of rotation. Measurements were then taken at

approximately every 100 000 cycles thereafter. The test specimens were removed from the test machine by lifting the loading arm using a screw jack [16].

The changes in diameter were recorded in order to calculate the surface wear rates. The rate of wear for each test specimen is measured as diameter change verses number of cycles. At each measurement interval 15 measurements were taken when the specimen was removed from the test machine. The measurements were then averaged. As a result there are a number of decimal places for each diameter measurement. The measurements are used to plot changes in diameter against number of rotational cycles of the test specimen. Factors effecting the measuring of the test specimens were temperature, small amounts of surface contamination and possible increases in surface roughness.

During each test both the main rotating disc and the test specimen were cleaned at approximately every 40 000 cycles of rotation. The aim was to remove any loose wear partials or contaminants from the mating surfaces during testing. The surface cleaning was preformed by rubbing an ethanol cloth against the main rotating disc. Wear particles and contamination were transferred to the cloth. This was done to limit the amount of abrasive wear in the test as the test specimen would not have to roll over previously dislodged wear particles.

The rolling contact fatigue test was complete when the test specimen completed 1000 000 cycles of rotation. However if facture or collapse of the rolling contact surface occurred at cycles less than 1000 000, the test was stopped and number of cycles noted.

Upon completion of each rolling contact test the specimen was removed from the specimen assembly (i.e. Bearings, shaft and locking element are removed). The test specimen was cut[24] at the surface, the sample mounted and prepared for micro structural photographs[25] taken under a microscope [26] at various magnifications.

The sample preparation was conducted according to the sample preparation procedures described in the *Metalog guide* published by *Struers* in 1992 [69]. The cut specimens from the contact surfaces are mounted in a mounting press 27. The preparation of the test samples is conducted in 4 operations, 2 grinding and 2 polishing. The samples were prepared using a polishing machine 28. At each of the preparation steps the mounted sample is ground / polished on different rough surfaces with the addition of an abrasive solution. The solution is a combination of an abrasive and a lubricant. Each preparation step was conducted at a specific speed, applied force and time duration. The settings for these variables are set on the polishing

machine. Samples were etched following polishing using Nitol. Table 3 illustrates the test specimen preparation procedure [69].

Table 3 Sample preparation procedure [69]

Grinding		
Surface	MD-Piano 220	MD-Allegro
Abrasive	Diamond	DP-suspension
Grit/Grain size	/	9 μm
Lubricant	Water	Green/Blue
rpm	300	150
Force (N)	180	180
Time (minutes)	until plane	4
Polishing		
Surface	MD Dac	MD-Chem
Abrasive	DP-Suspension	OP-A
Grit/Grain size	3 μm	/
Lubricant	Green/Blue	/
rpm	150	150
Force (N)	180	90
Time (minutes)	4	2
Etchant	Nitol	

Figure 9.13 Illustrates the surface which was cut and than mounted for visual inspection under a microscope. The mounted samples allowed for the depth in section to be inspected.
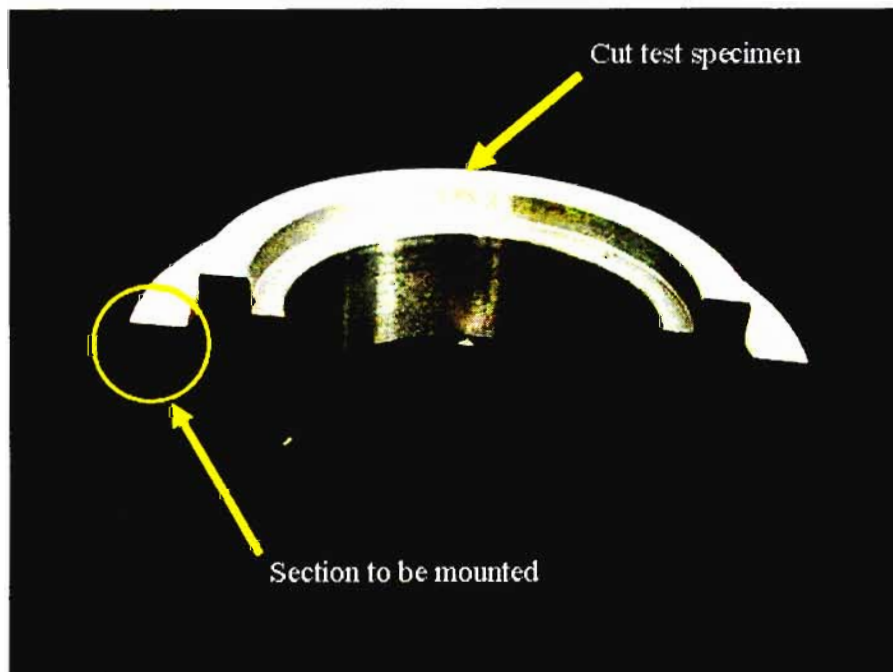
Figure 9. 13 Cut test specimen following testing

9.3 List of Equipment, components and instrumentation

1. Test specimen   Ø100 mm width 10 or 5 mm material En 9
2. Main rotating disc   Ø350 mm width 40 mm, material Benox
3. Grinding station
   3.1 Grinding stone:200X20X31.75 38A60 VH Maximum speed 6570 rpm

   3.2 Electric motor: 0.75 KW, 2 pole, 3 phase, 2845 rpm A.C motor

   3.3 Grinding stone attachment

   3.4 2 axes bed

4. Ball bearings UC212
5. Plumber block bearing housings   TR P212
6. Flange mounted AC electric motor   5.5Kw 1440 rpm
7. Gearbox   SEW flange mounting gearbox. Ratio 1.78:1
8. Belt drive   4 grove wedge belt ratio 3.5:1
9. Frequency controller   Commander SE 11Kw
10. Specimen assembly
    10.1 *Fenner* Taper-lock   FLK 133 30X55
    10.2 Ball bearings   6205 DU
11. Bearing cups
12. Loading arm
13. Loading arm pivot mounting bearings:
14. Y bearing flange unit: FL 205 TR

15. Mass pieces: Cast ± 9 Kg cast weights pattern U 5714 *Umgeni iron works*

16. Screw jack   *Prolift* 1500 Kg scissor jack SF-2119444

17. Load cell   VLC-110S   capacity 600Kg

18. Readout   *Vertical measurements and control* read out. *Model VC-210*
19. Cycle counter   Zenith instruments Model 489-6D counter/time
20. *Detechtor*   inductive proximity sensor

21. *Raco* Builders line Nylon Monofilament 0.8 mm Diameter 27.3 Kg Breaking strain.

22. Avery Berkel scale F100   Max capacity 2 Kg

23. Micrometer spindle: Manufacturer *L.S.Starrett Co.* (USA)

24. Cutoff saw: *Imptech* abrasive cutter

25. Camera: *Nikon Coolpix 990*

26. Microscope: *Nikon Epiphot- TME* Inverted microscope

27. Mounting machine: Struers LaboPress-3

28. Grinding and polishing machine: Motopol 2000 grinder/polisher

29. Matrix cylindrical grinder manufacturer Coventry gauge and tool Co. Ltd (UK)

10. Test Results

Irrespective of the applied load the rolling resistance for all the test specimens coated and uncoated was measured to be an average of less than 1%. This is the ratio of applied load to force required to rotate the disc. This indicates that all testing was done under very near perfect rolling contact conditions. The rotational speed for all test specimens was maintained at approximately 160 rpm as the main rotating disc was rotated at a constant 563 rpm. Slip between test specimen and main rotating disc was measured to be substantially less than 1%, further indicating the very small quantity of friction (negligible traction) present under test conditions.

10.1 En 9 Steel

All specimen samples were machined from the same En 9 steel bar. The bar was manufactured at Frankwen Forge (Pty) Ltd. The bar was swaged and then normalized. Quality control testing performed by the company stated the following approximate mechanical properties for En 9 manufactured there:

Yeild stress / Proof stress	=	±350	MPa
Ultimate tensile strength	=	±750	MPa
% Elongation	=	20 %	
Hardness Brinell	=	200	BHN

In order to verify these results obtained for normalised En 9 steel, a book of British standard En steels was consulted [68]. The mechanical properties were stated in imperial units and were converted using conversion tables [55]. The converted quantities were found to be consistent with stated values. En 9 is a British alloy designation, alternative American designations for the same alloy are 1055 (SAE) and C1055 (AISI) [70].

A chemical analysis of the En 9 used in the manufacture of all the test specimens was conducted at an independent laboratory [70]. The results of which are as follows:

Carbon	0.56	%
Manganese	0.64	%
Sulphur	0.012	%
Phosphorus	0.01	%

Silicon   0.19   %

The above percentages are the constituting elements while the remaining material is iron. The percentages obtained for the compositional analysis fall within the specification of the En 9 alloy [70].

The figure below is a picture of the microstructure of the En 9 used in the present work. The microstructure consists of both ferrite and pearlite. The white rectangle in the corner of the picture represents 50μm.

Figure 10. 1 En9 microstructure (scale 50 μm)

The yield stress in simple shear for a given steel can be determined if the yield stress in simple tension or compression is known. The yield stress for En 9 is ±350 MPa, the resulting value for the yield stress in shear (k) is approximately 200 MPa (equation 22).

Both the hertz contact stress (Po) and the yield stress in simple shear (k) are important in the calculation of the load factor and determining the material response under rolling contact. A detailed discussion is presented in Chapter 6.2.

Four test specimens were tested at Hertz contact stresses of 300, 500, 700 and 900 MPa respectively. Using a value of 200 MPa for the yield stress in simple shear (k) the load factor

ratio under which the tests were conducted were1.5, 2.5, 3.5 and 4.5. Differences and changes in wear rates, contact widths and surface hardness for each of the test specimens were noted.

10.1.1 Wear

During the testing of all En 9 test specimen, wear was observed as a continuous removal of wear debris in the form of wear particles from the contacting surfaces. The wear particles were thrown free of the surfaces of the bodies and landed all over the testing machine. Figure 10.2 illustrates the wear particles on the wear machine surface. Wear particles were collected using a glass slide and are shown in Figure 10.3.
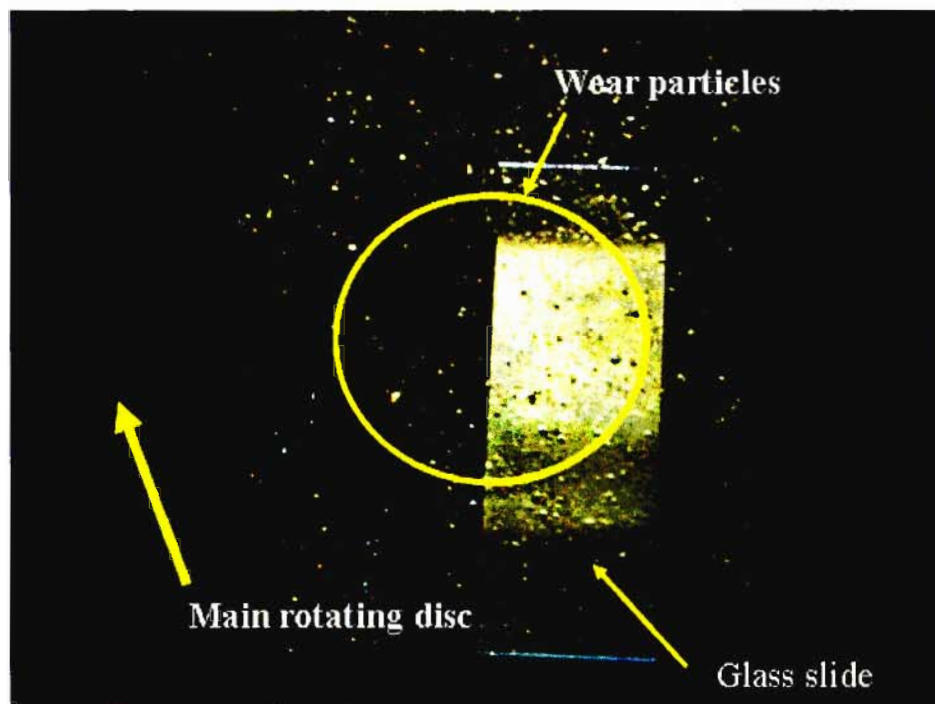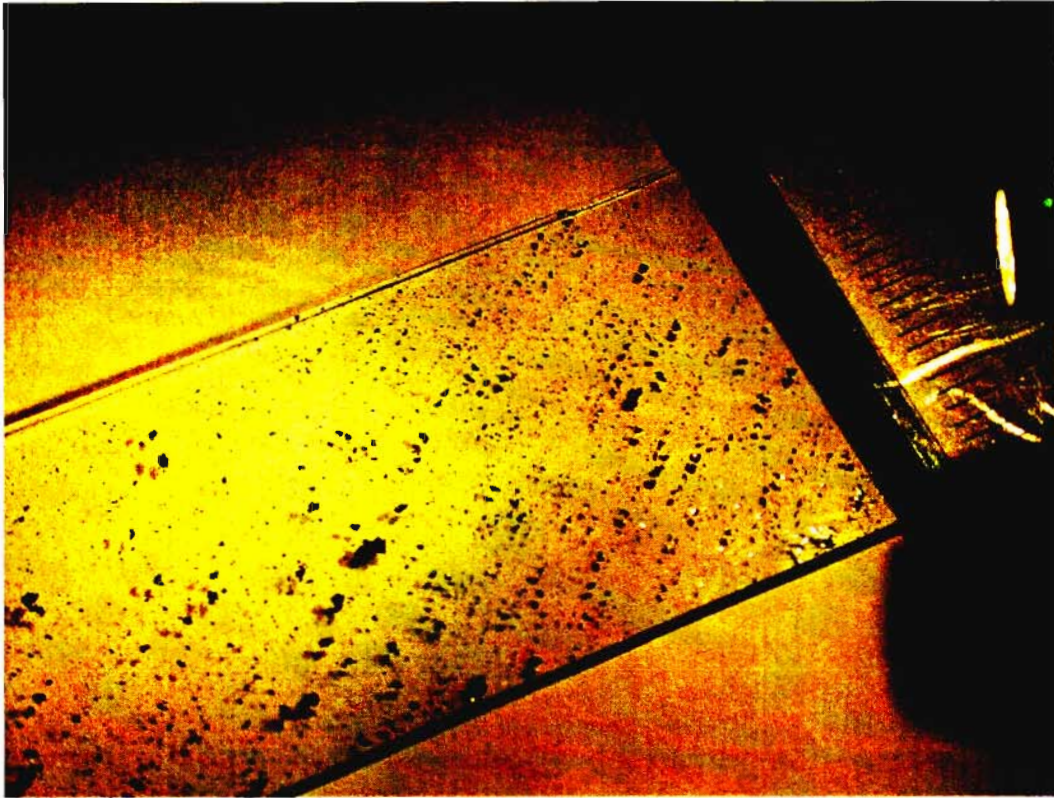

Figure 10. 2 Collection of wear particles during testing

Figure 10. 3 Wear particles on glass slide

The quantity and rate of wear was measured as a change in specimen diameter over a number of cycles. At approximate intervals of 30 000, 60 000, 100 000 and every 100000 cycles thereafter, the test specimen was removed from the test machine and the diameter measured.

Specimens once removed from the test machine were cleaned thoroughly with ethanol to remove any surface contamination. At each diameter measurement interval fifteen measurements of were taken and averaged. This was performed for accuracy as the changes in diameter were small between measurement intervals. Diameter measurements to the nearest micrometer only, could be measured, however averaging allowed for further accuracy.

The averaged diameter measurements were plotted against the number of cycles completed by the particular specimens (Figures 10.4, 10.5, 10.6).

The diameter measurements are indicated in the graphs as data points and are represented by red indicators. The blue line is the best fit linear function formulated using the software for the given data points. A small degree of scatter is observed about the linear function, this may be explained by factors affecting the measurements. Factors such as temperature differences, small amounts of surface contamination and possible changes in surface roughness may affect the measurements at any specific measurement interval.

The linear best fit functions (Blue line in the wear graphs) are plotted in a combined graph (Figure 10.7). This allowed for wear rates of test specimens to be compared to each other. No graphs could be plotted for specimen 4 tested at a Hertz contact stress of 900 MPa (Po/k 4.5). The test was aborted at 5000 cycles of rotation due to extreme wear from the commencement of the test. The wear was observed to be producing major damage to both contacting surfaces and was aborted.
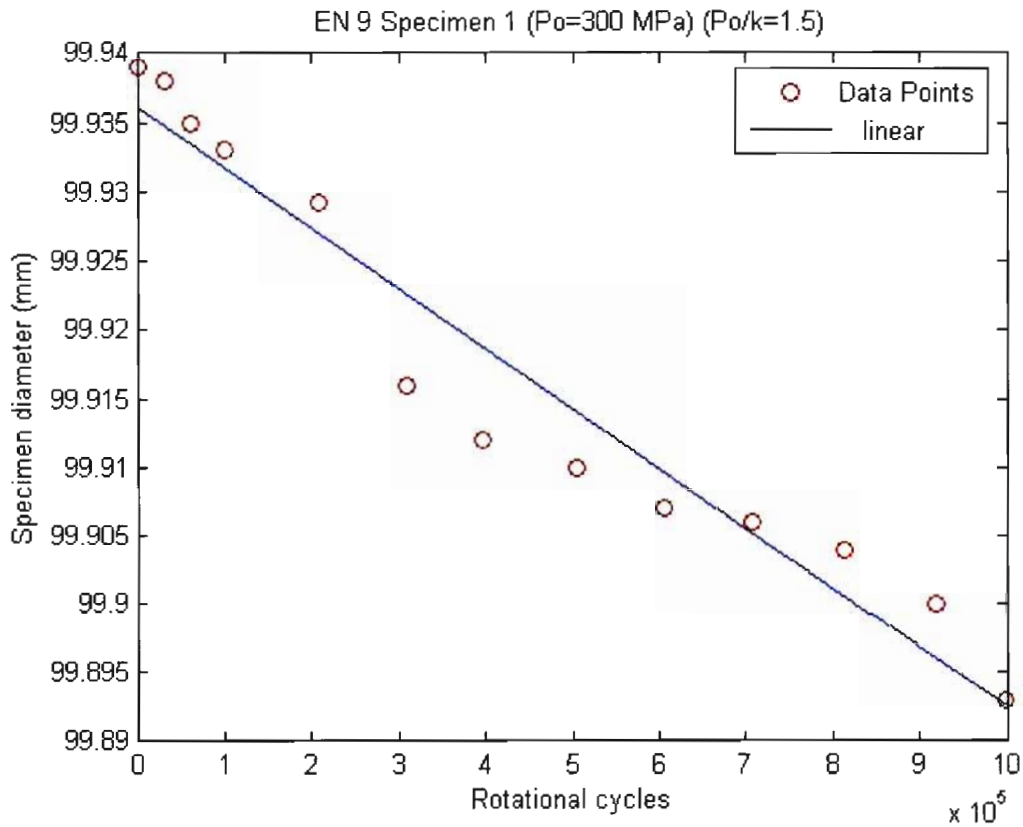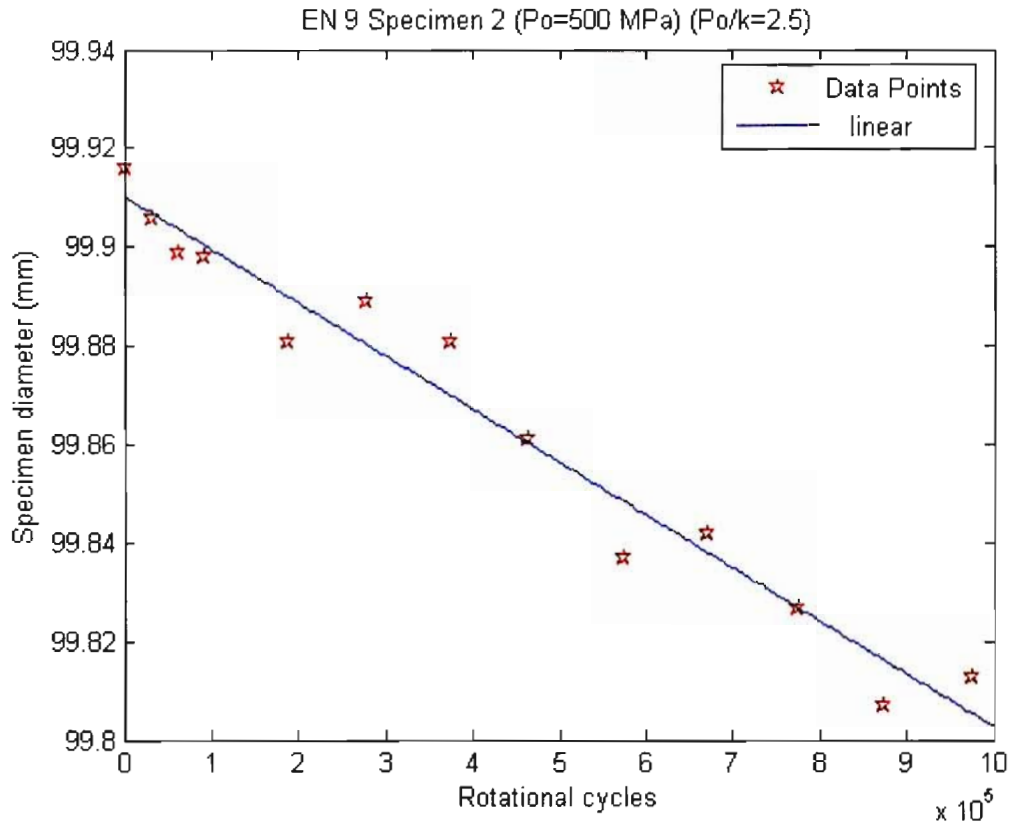

Figure 10. 4 En9 Specimen 1

94
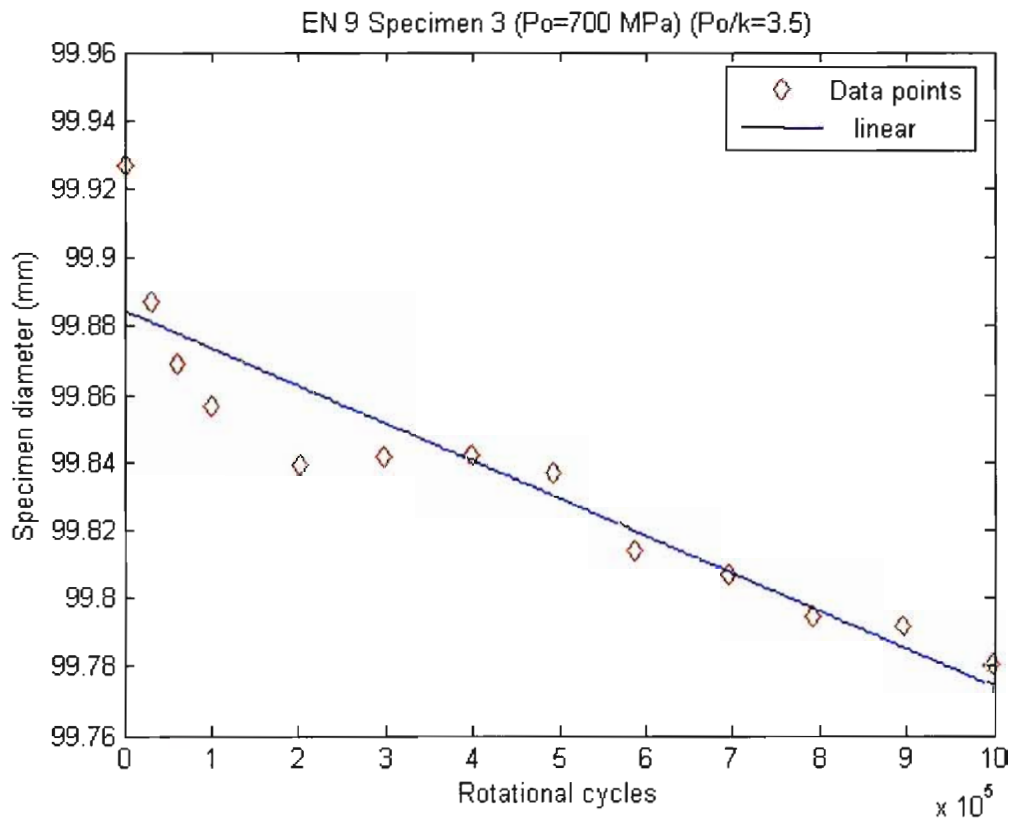
Figure 10. 5 En9 Specimen 2

Figure 10. 6 En9 Specimen 3

Possible wear mechanisms responsible for the changes in diameter are adhesive wear, abrasive wear and fatigue (macroscopic and microscopic) wear. Specifics of these wear mechanisms are discussed in Chapter 7.

Adhesive wear could not have had a significant role on material removal under the tested conditions. The reason for this is that adhesive wear is characterized by high coefficients of friction. The testing was conducted under near perfect rolling contact conditions therefore the role which adhesive wear could have played is significantly small or negligible.

Abrasive wear may have had a slightly more significant role. Wear particles removed from the surfaces which were not immediately removed may have been rolled back through the contacting area allowing three body abrasive wear to operate. However due to the regular cleaning of the contacting surfaces during testing and at each measurement interval the effect of this wear mechanism would have been greatly reduced.

Surface fatigue wear is believed to be the predominant wear mechanism under the tested rolling contact conditions. This is indicated by inspection of Figures 10.5, 10.4.and 10.7. The linear wear rate (blue lines in Figure 10.4 and 10.5) for the specimen tested at a Hertz contact stress 500 MPa (red line in Figure 10.7) is steeper than that of the specimen tested at 300 MPa (green line in Figure 10.7). This indicates that a greater rate of wear was experienced for the test specimen tested at 500 MPa than at 300 MPa. The greater the Hertz contact stress the larger the contact stresses at the contacting asperities.

While macroscopic fatigue is experienced as a result of the Hertz contact stress, microscopic fatigue wear is a result of contact stresses at surface asperities. An increase in Hertz contact stress therefore increases both the effect of macroscopic and microscopic fatigue wear. This is in line with fatigue principles that the higher the stress the greater the effect of fatigue. A discussion on both macroscopic and microscopic fatigue is presented in Chapter 7.3.

Following the completion of each test, the specimens were cut and mounted. The microstructure of the material near the contacting surface was inspected. No surface or subsurface cracks were found. As macroscopic fatigue is characterized by the development of cracks leading to the fracture or macroscopic spalling of a surface it is concluded that the macroscopic fatigue wear mechanism was not present.

However microscopic fatigue defined as the fatigue failure of contacting asperities under rolling contact is the most significant and predominant fatigue mechanism present during the tests.

It is this failure mechanism which resulted in the generation of small wear particles observed during testing (see Figure 10.3).

While wear of both contacting surface was observed, the majority of the material was removed from the test specimen while only a small amount of wear was observed on the main rotating disc. This further highlights the fact that the fatigue wear mechanism is predominant under the tested conditions. The diameter relationship between the test specimen and the main rotating disc is 3.5. This means that a surface asperity on the test specimen would pass through the contact area 3.5 times more often than asperity on the main rotating disc. This will result in the asperities on the test specimen experiencing more stress cycles, the greater the number of stress cycles the greater the effect of fatigue on the surface asperities which in turn leads to microscopic fatigue failure.

An important observation is noted in the rate of wear of specimen 2 and 3 (Figure 10.5 and 10.6). Specimen 2 was tested within the elastic region (Po/k = 2.5), while specimen 3 was tested within the shakedown region (Po/k = 3.5). The resulting best fit linear graphs plotted in Figure 10.7 illustrate the rate of wear for the two test specimens are similar (red and blue lines) while the contact stress for specimen 3 is higher. An explanation for this can be given as follows.
For specimen 2 the material remained elastic within the contact region. The resulting wear rate remains reasonably constant throughout the testing. However specimen 3 was tested within the shakedown region for the given material. Specimen 3 would therefore have had to experience elastic shakedown in the initial number of contacting cycles. This is illustrated by the large difference (diameter change) from first data point to the next data point at 30 000 cycles in Figure 10.6. Following the initial shakedown the material within the contact region behaves elastically. Following this initial steep change in diameter the rate of wear remains simarlar to that of test specimen 2 tested at 500 MPa and within the elastic region is obtained. A discussion on the rolling contact stress analysis and material shakedown can be found in Chapter 6.2. However the wear rate of specimen 3 remains slightly higher than specimen 2 indicating the effect of slightly higher stress on the fatigue failure mechanism.
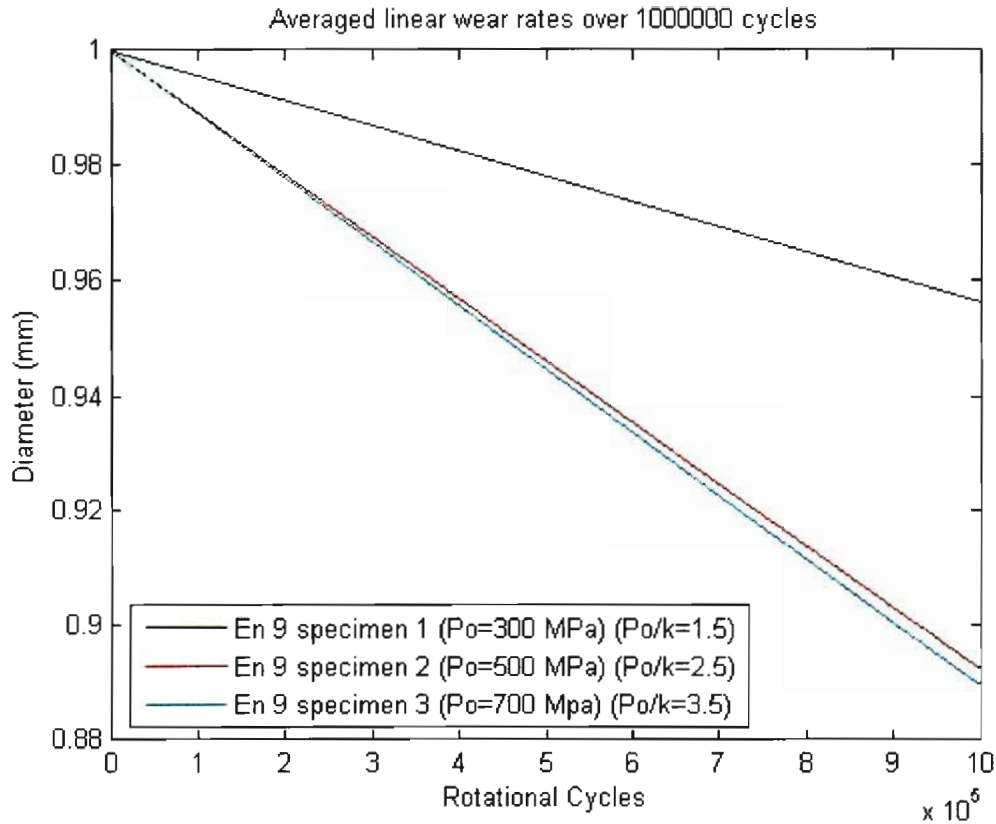
Figure 10. 7 Rates of wear

10.1.2 Surface Hardness

The hardness values for each of the tested specimens were measured following the completion of each test. The surface hardness values were measured using a digital Rockwell type hardness tester. The measurements were taken at the center of the test specimen's contacting surface, this was done to reduce the effect of the edge deformation on the hardness measurement. The values obtained were an average of five readings and are stated as follows:

Untested 0	0	MPa	95 HRB
Specimen 1	300 MPa		96 HRB
Specimen 2	500MPa		96 HRB
Specimen 3	700 MPa		96 HRB
Specimen 4	900 MPa		100 HRB

All tested specimens were noted to have an increase in hardness value. The increase in hardness value is due to the material response to the applied contact stress. The measured hardness values of the test specimens are in good agreement with the predicted material behavior and shakedown map.

98

The same hardness value of ~ 96 HBR for specimens 1, 2, 3 tested at 300, 500, 700 MPa respectively was measured following testing. This observation has possible correlation with the theory as specimen 1 and 2 were tested within the elastic region and specimen 3 was tested within the elastic shakedown region. Specimen 3 would have experienced elastic shakedown during the initial number of rolling cycles, at the completion of the test the test the surface would behave elastically.

It is further noted that the hardness value of specimen 4 is significantly larger than all the other test specimens. This again is a result of the contact stress and resulting material response. Specimen 4 was tested at a contact stress greater than the shakedown limit. The resulting material response is ratcheting and plastic shakedown. Plastic shakedown and ratchetting material response is discussed in section 6.2.3.

10.1.3 Contact width

Plastic deformation at the edges of all test specimens was noted following testing. The plastic deformation had the effect of increasing the contact width. It was also noted that the contact width was increased as the tested contact stress increased.

The plastic deformation was a result of increased stress at the edges of contact. The increased stress had the effect of yielding the edge material which deformed outwards. The material inwards of the edges however experiences the stresses calculated by Hertz contact theory. A discussion of edge contact stresses can be found in Chapter 5.

Figure 10.8 show the microstructure at the edge of test specimen 4 following testing. The yellow dashed line illustrates the position of the machined perpendicular edges prior to testing. It can be seen that after testing the edge has been deformed outwards.
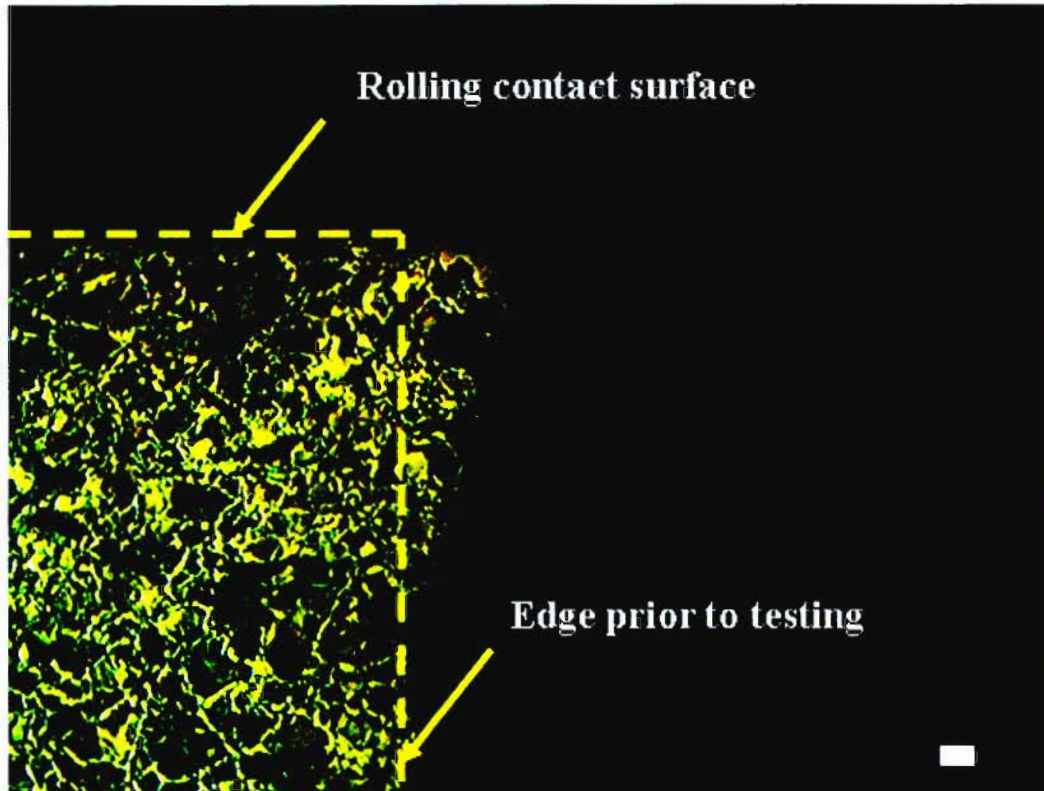
Figure 10. 8 En9 microstructure with edge deformation (scale 50 µm)

In the captions of the Figures (10.9, 10.10, 10.11, 10.12) are photographs of the cross sections of the 4 En 9 specimens tested at separate Hertz contact stresses. The edge of the test specimen adjacent to the line marked Lf is the outer contacting surface of the test specimen. An increase in contact width was noted for all for tested specimens. The higher the contact stress the greater the plastic deformation at the edges of the test specimen and the greater the increase in contact width.

The length marked Lo in the pictures is the original contact width. This is the machined contact width prior to testing. The contact width at this section was unaffected by the plastic deformation at the edges of the contact surface. Length Lo was machined with parallel edges and was a set distance measured prior to testing. Length Lf in the pictures represents an increase in contact width as a result of plastic deformation at the edges of contact.
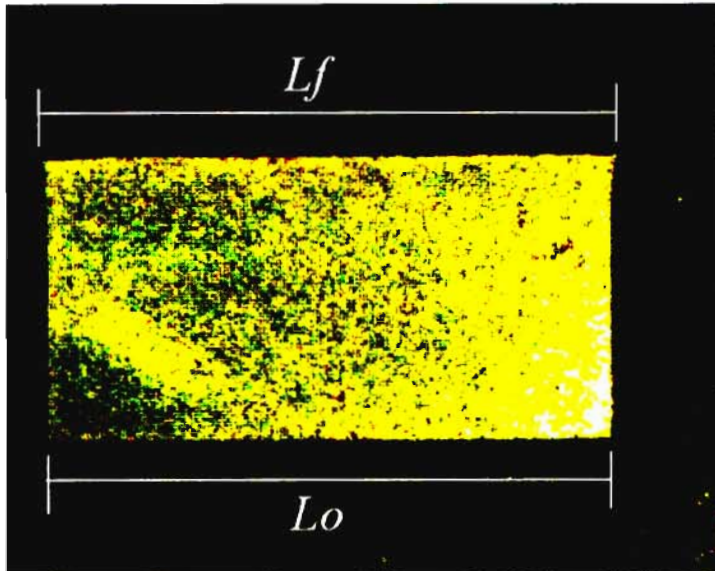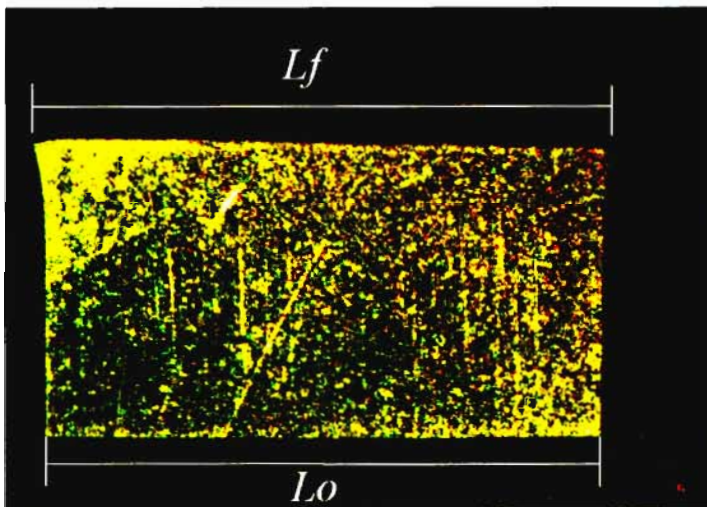
Figure 10. 9 Specimen 1 En9@300MPa

Figure 10. 10 Specimen 2 En9@500MPa
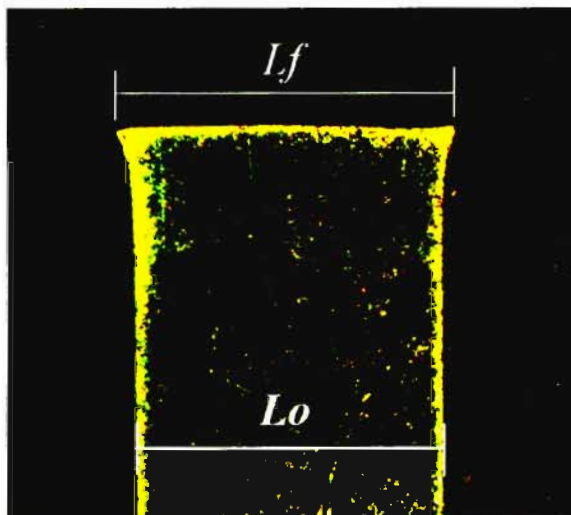
Figure 10. 11 Specimen 3 En9@700MPa
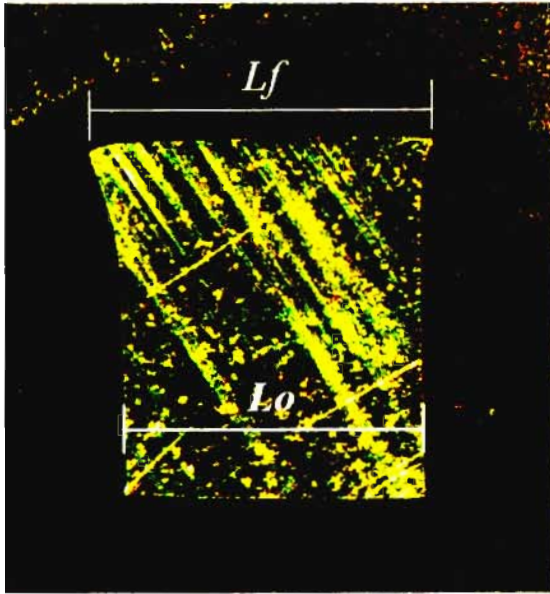
Figure 10. 12 Specimen 4 En9@900MPa

The amount of deformation at the contacting edges of each test specimen was measured. The initial contact width *Lo* was measured prior to testing and deformed length *Lf* was measured after testing. Table 4 illustrates the measured contact width before and after testing. The measurements are stated in millimeters. The values in table 4 were used to plot the graph shown in Figure 10.13.

Table 4 Increase in contact width (En 9 specimens)

Contact width before test *(Lo)* (mm)	10.05	10	5.05	4.95
Contact width after test *(Lf)* (mm)	10.3	10.4	5.5	5.7
% increase in contact width	2.487562	4	8.910891	15.15152
Hertz Contact stress (Po) (MPa)	304	508	706	918.00
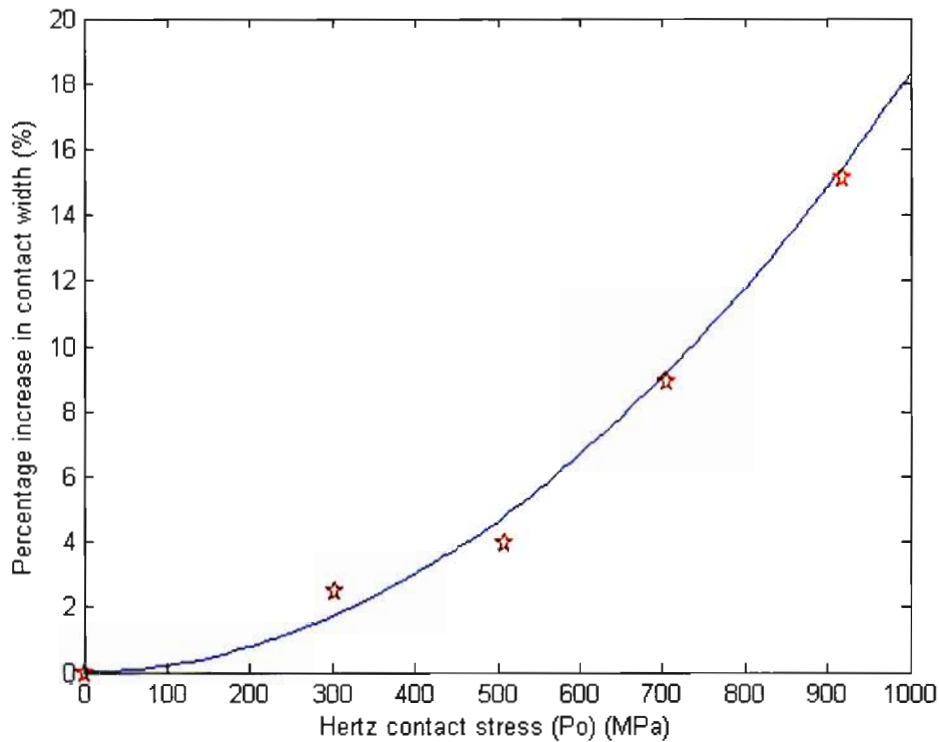
Figure 10. 13 % increase in contact width

The graph in Figure 10.13 illustrates an increase in plastic deformation with increase contact stress. The red stars represent the percentage increase in contact width plotted versus applied hertz contact stress. The percentage increase is calculated using the difference between the contact width prior to testing (*Lo*) and following testing (*Lf*). Four of the stars represent the 4 En 9 test specimens while a 5th data point was added. The reasoning behind adding this point was that at no applied load no contact stress can be generated and therefore no deformation can occur (Po=0, % increase in contact width = 0)

A best fit curve (blue curve in Figure 10.13) for the measured data points was plotted. The equation for the curve is quadratic and is defined by the following equation:

$$\%increase = 1.7989 \times 10^{-5} P_0 + 3.5728 \times 10^{-4} P_0$$

Where Po is the calculated hertz contact stress on the x axis and the left hand side of the equation is the percentage increase in contact width. While the graph appears to fit neatly with the data points represented by the red stars, this is only an observation and to develop an exact equation governing contact width increase with increase in contact pressure would take substantially more empirical data.

10.2 Plasma coating

The plasma coated test specimens were coated at a company situated in Durban called Ceramic Anilox Engravers Pty Ltd. The company is involved in the refurbishment of ink rollers for the printing industry. The refurbishment involves the plasma coating of the rollers followed by the engraving of the hexagonal patterns on the surface of the rollers. The patterns are engraved using a laser. Following the plasma coating process the coating thickness was ground to have a thickness of 100 μm.

The microstructures formed for both powder compositions applied using plasma coating were similar. This is evidence that for plasma spraying, the microstructure of the coating is dependent on the coating process and not on the chemical composition of the coating powder used. The resulting bonding mechanism between coating and substrate is mechanical (no fusing or mixing of coating and substrate material). Figure 10.14 illustrates the mechanical bond at the interface.

The microstructures of both plasma sprayed coating compositions contain small voids and particles of un-melted powder. The nature of the plasma coating is discussed in section 8.1.2. Figure 10.15 illustrates the voids and un-melted powder particles. During the rapid coating and solidification process, air is often not fully evacuated from around un-melted particles resulting in the development air pockets or void spaces [62]. The material in Figure 10.15 occupying the void space is mounting resin which has been polished flat with the specimen prior to inspection.
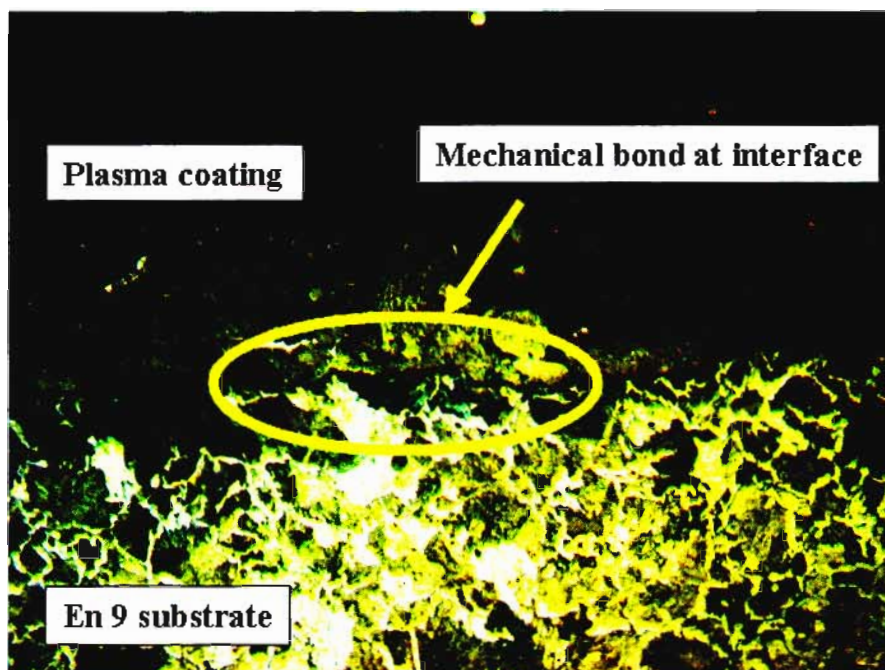

Figure 10. 14 Plasma coating bonding mechanism (composition 1)
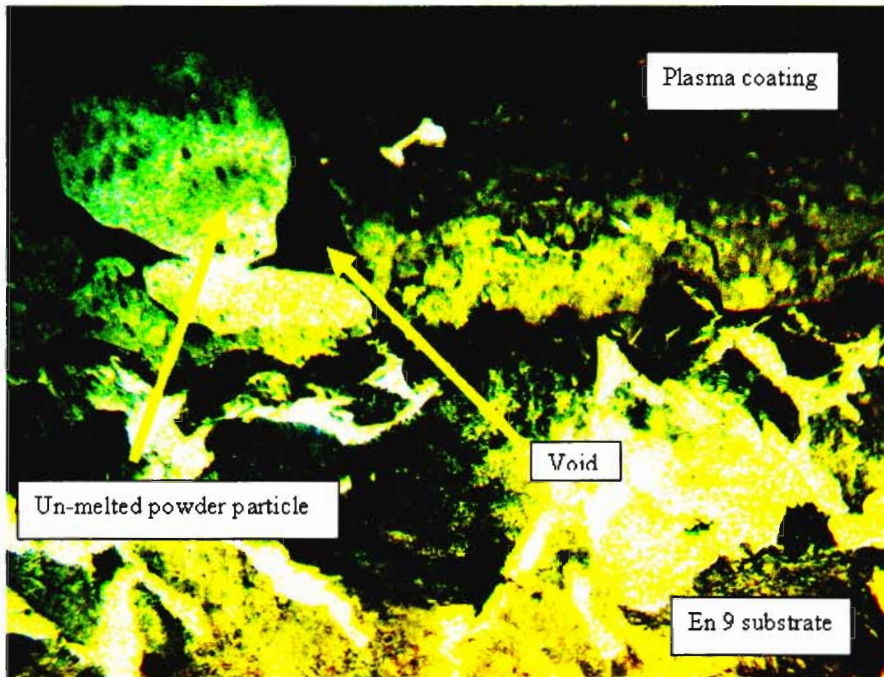
Figure 10. 15 Plasma coating microstructure

All test specimens failed as a result of delamination of the coating from the substrate at the edges of contact. The rolling contact tests were aborted when delamination was observed. Surface wear was not measured as failure occurred prior to any observable wear (diameter change).

The delamination of 3 of the test specimens all appeared the same. Figure 10.17 illustrates the resulting edge delamination. Specimen PC1500 also failed as a result of delamination which caused the coating to fracture and be removed from the complete contact width of the test specimen. The fractured coating is shown in Figure 10.16.

The number of cycles to failure for each test specimen are as follows:

Specimen PC2300   : Failed   at 74122 cycles (delamination)

Specimen PC2500   : Failed   at 51784 cycles (delamination)

Specimen PC1500   : Failed   at 28485 cycles (delamination)

Specimen PC1300   : Failed   at 314146cycles (delamination)
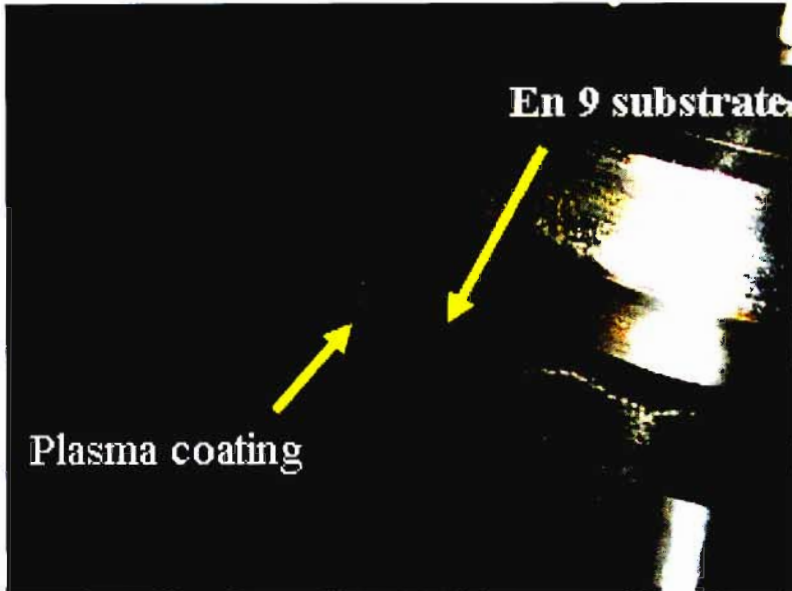
Figure 10. 16 Test specimen PC1500
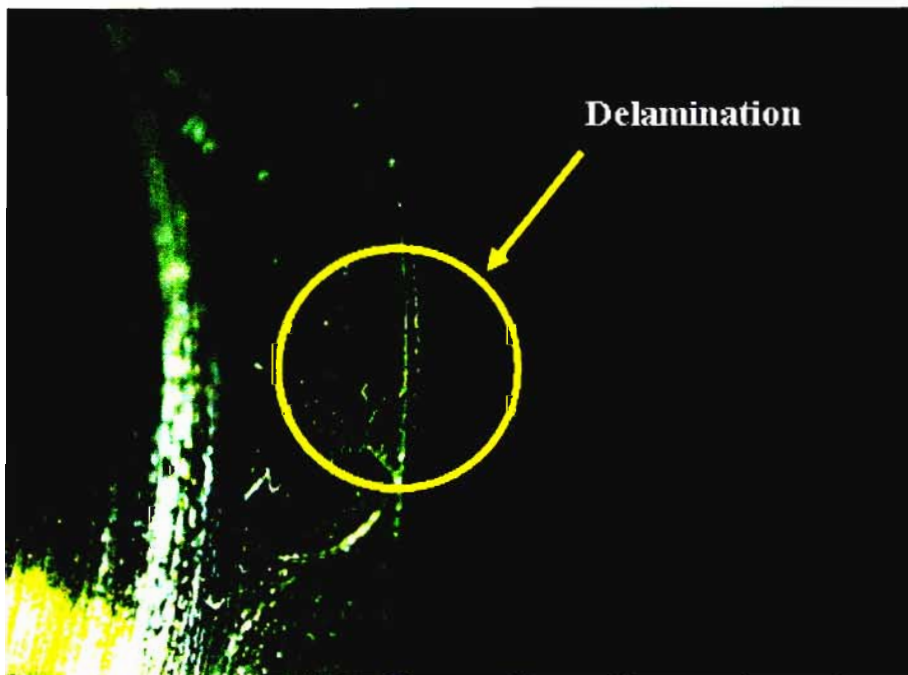
Figure 10. 17 Test specimen PC1300

The failure mechanism for the plasma sprayed test specimens was macroscopic fatigue resulting in the delamination of the coating. The delamination was observed as fracture of the bond between the coating and substrate at the interface between the two. The failures are observed to have occurred at the edges of contact. At this position the contact stresses are greater than the normal contact stress. A discussion regarding the increase in contact stress at the edges of contact is discussed in Chapter 5. The coating may well have been able to operate at the nominal

calculated Hertz contact stress, however the increased stress at the edges resulted in coating delamination.

Plasma coating therefore may prove useful in lower contact stresses applications, however a combination of the increased stress at the edges of contact resulted in failure.

The longer life in rolling cycles for both compositions tested at the lower stress of 300 MPa was observed, this is in line with general fatigue principles that the lower the stress level the longer the life. This is therefore a further indication that the failure mode of the plasma coatings was fatigue at the bonding interface.

The results of the plasma contact tests seem to indicate that the rolling contact life is largely dependent on the interface to substrate bonding strength and not on the compositions of the coating itself. This is evident by the relatively low cycles to failure of the plasma coating and the failure mechanism. Figure 10.18 illustrates the edge delamination between coating and substrate, while Figure 10.19 illustrates at higher magnification the end of the delamination and the crack tip. It is clear to see that the failure is at the interface between the coating and substrate and is therefore result of poor bonding mechanism.
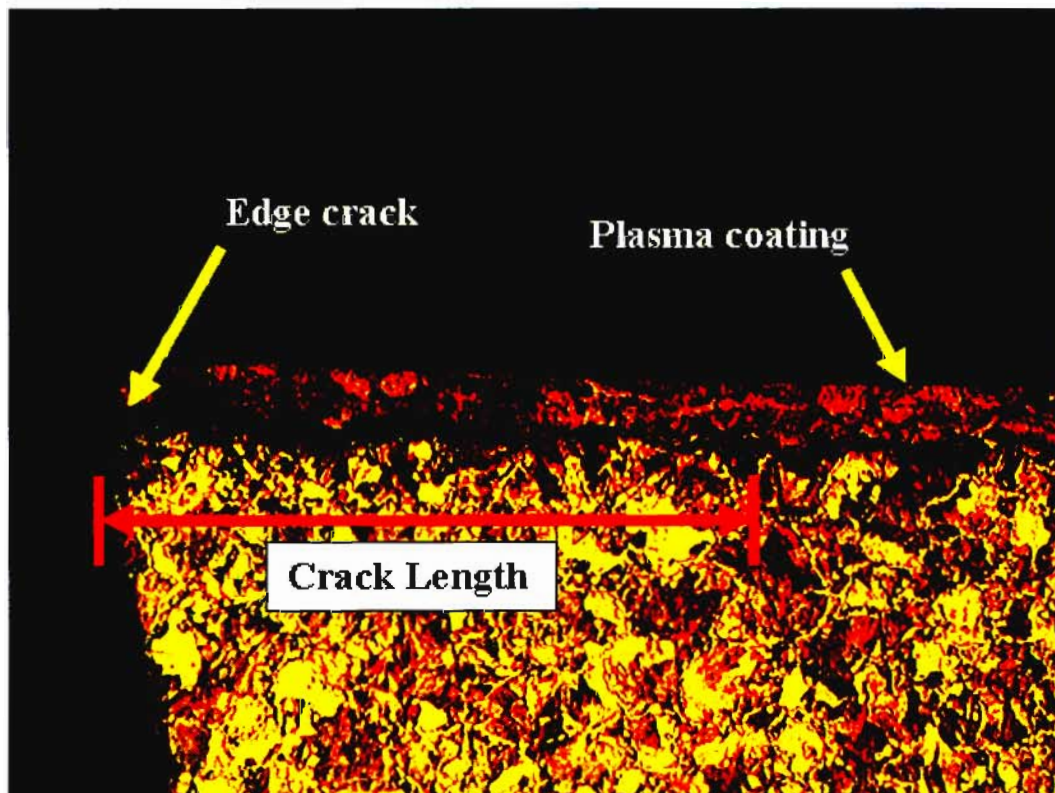

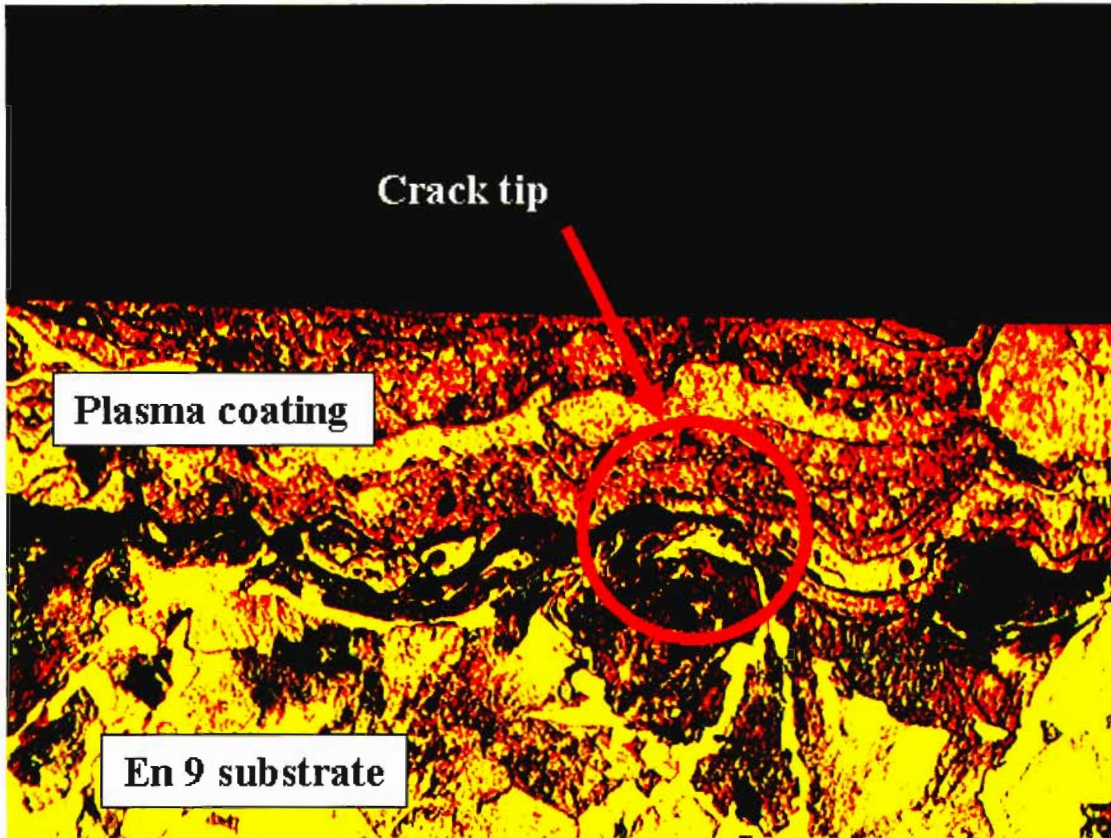**Figure 10. 18 Specimen PC1500 (edge delamination)**

**Figure 10. 19 Edge delamination between coating and substrate**

10.3 Laser Cladding

The cladding of the test specimens was conducted at the National laser Centre (NLC) based at the CSIR (Centre for Scientific and Industrial Research) in Pretoria. Two metal powder compositions were used. The compositions of the two powders are shown in Table 2. The following process parameters were used in the laser cladding process:

Coating thickness (as coated)   ± 1 mm
Bead width   4 mm
Nozzle standoff   15 mm
Laser power   3000 W
Cladding speed   1.2 m/minute
Gas flow rate   Argon at 7 liters / minute
Step over   2mm

Following the cladding process, 4 test specimens were ground to have a coating thickness of 0.2 mm. The 4 test specimens were referenced as LC1500, LC2500, LC1700 and LC2700. An explanation of the referencing is stated in the introduction to the Chapter 9. A general discussion of the laser cladding process and the nature of resulting coating is presented in Chapter 8.2.1; presented here is observations made for coated and tested specimens.

Figures 10.20 and 10.21 are photographs of the coated and ground specimens coated with powder compositions 1 and 2 respectively. The large image in each figure is the as coated specimen surface while the inserted picture is the same specimen after surface grinding. It is noted that composition 2 has visible porosity both before and after grinding while composition 1 shows no surface porosity. As the coating process parameters used in the cladding process were the same for both test specimens the porosity may be a result of differences in the powder compositions.
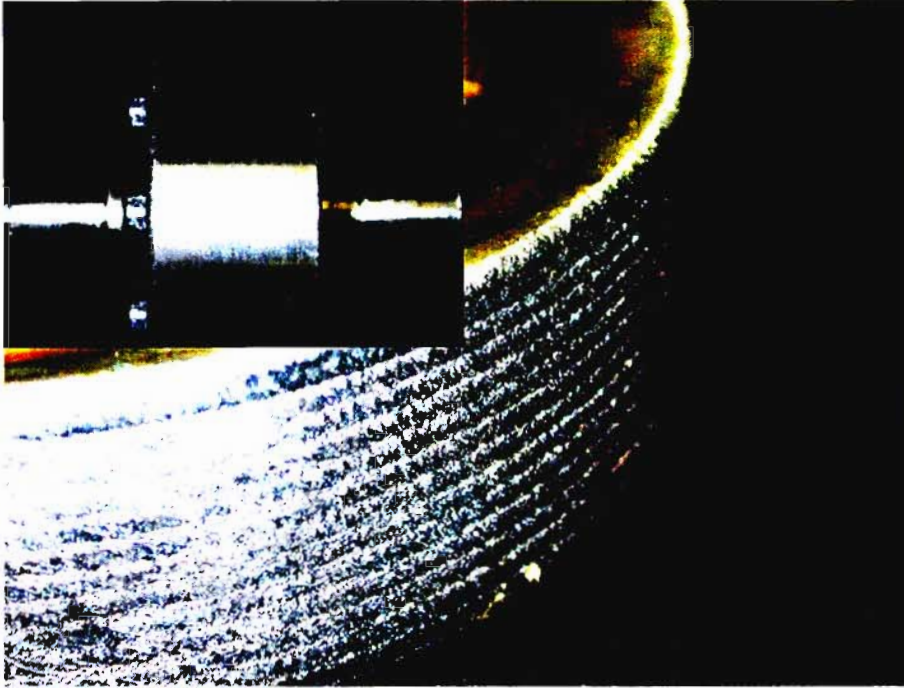
Figure 10. 20 Laser composition 1. As coated surface (main), ground surface (insert)

Visible surface porosity
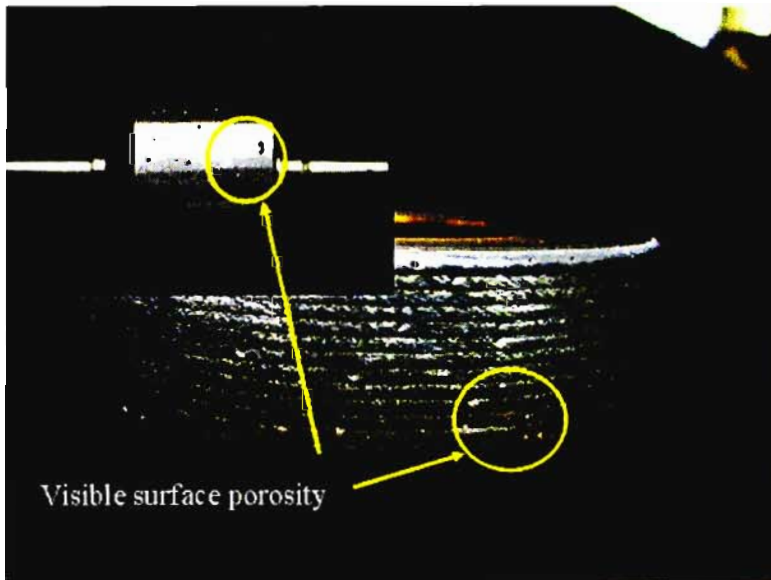
Figure 10. 21 Laser composition 2. As coated surface (main), ground surface (insert)

The hardness values for the laser clad samples were 30 HRC and 34 HRC for compositions 1 and 2 respectively. The hardness values for both coating compositions were harder than that of the En 9 benchmark test specimens. No change in the average hardness value was noticed at the completion of the rolling contact testing. This indicates that the surface material did not experience a change in the mechanical properties as a result of the testing. All hardness measurements were taken in the center of the contact width before and after testing.
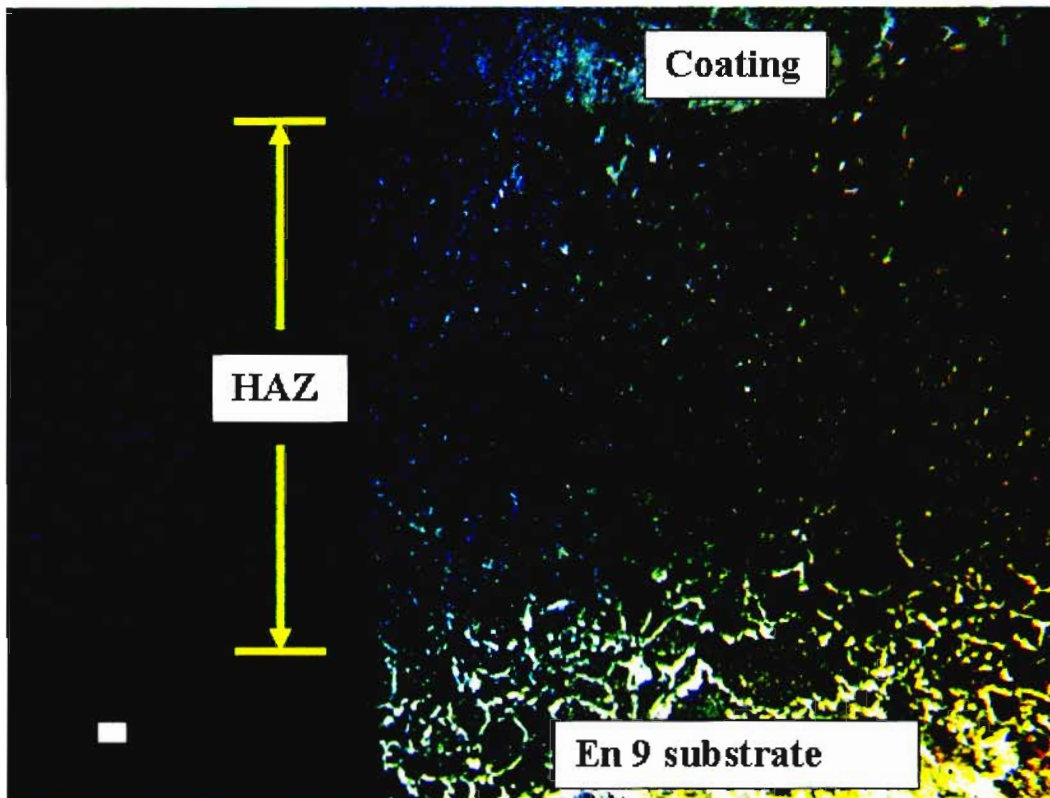
Figure 10. 22 Coating substrate (Heat Affected Zone)

Figure 10.22 illustrates in section, the edge of a laser clad specimen. Laser cladding is a fusion process resulting in the formation of a Heat affected zone (HAZ) between the coated layer and substrate. The HAZ is formed as a result of mixing of the coating and substrate at high temperature resulting in the formation of different microstructures and various compositions with depth below the surface. The composition of the coated layer is that of the powder used in the cladding process while the substrate near the surface has the composition and microstructure of the En9. The composition of the HAZ is a combination of elements from both the substrate and coating, the resulting microstructure is again different from both the substrate and coated layer. Factors affecting properties and characteristics of the HAZ are various cladding process parameters (power input, cladding speed and nozzle standoff).

10.3.1 Fatigue and surface wear

Figures: 10.23, 10.24 and 10.25 represent graphs of changes in diameter against number of rolling cycles completed for test specimens LC1500, LC2500 and LC2 700 respectively. The red indication points in the graphs represent diameter measurements taken at a number of completed cycles. The blue line in each graph represents the best fit linear function for the measured data points. The calculation for the function of the line was calculated using software in the plotting programme. The slope of the line is an indication of the rate of surface wear

111

during testing. The small degree of scatter of the data points may have been a result of either one or a combination of the following: slight surface contamination, temperature differences or increase in surface roughness.

The predominant surface wear mechanism for specimens LC1500, LC2500, and LC2700 is believed to be microscopic fatigue. An explanation of the effects of other wear mechanisms is discussed in Chapter 7.3.2. The type of wear is the same as that of the benchmark En9 test specimens. Other wear mechanisms may have played a small or no role in the measured surface wear. An explanation of effect of other wear mechanisms under the tested rolling contact condition is discussed in 10.1.1.

While 3 of the 4 test specimens experienced surface wear, specimen LC1700 failed as a result of macroscopic fatigue leading to the fracture of the coating. The fracture occurred at 34068 cycles. Due to the early failure of the specimen no diameter measurements were taken as a result no wear graph could be plotted.
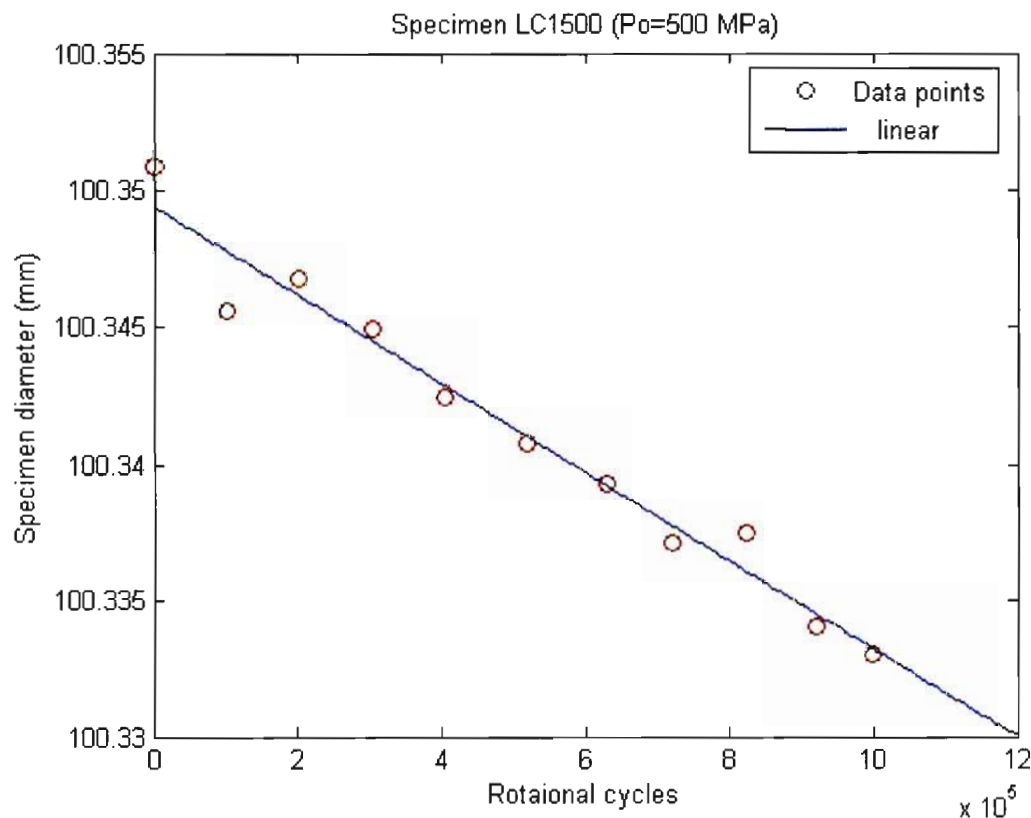

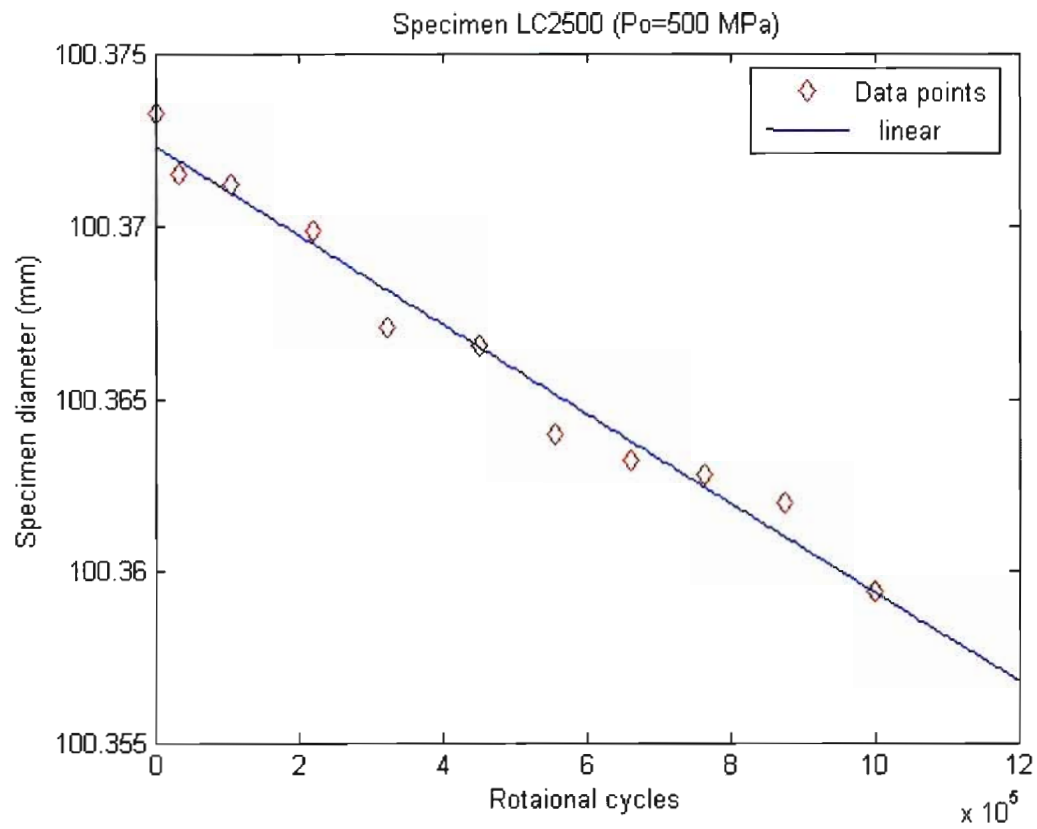**Figure 10. 23 Surface wear of specimen LC1500**

Figure 10. 24 Surface wear of specimen LC2500
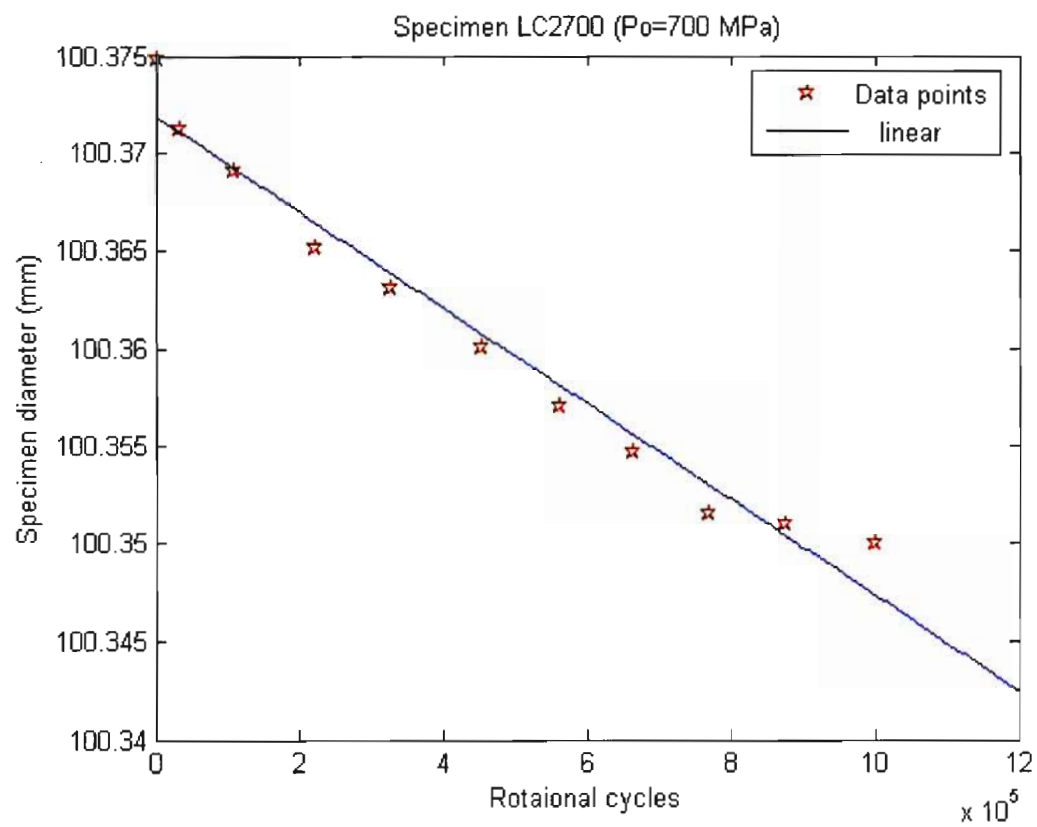
Figure 10. 25 Surface wear of specimen LC2700

113
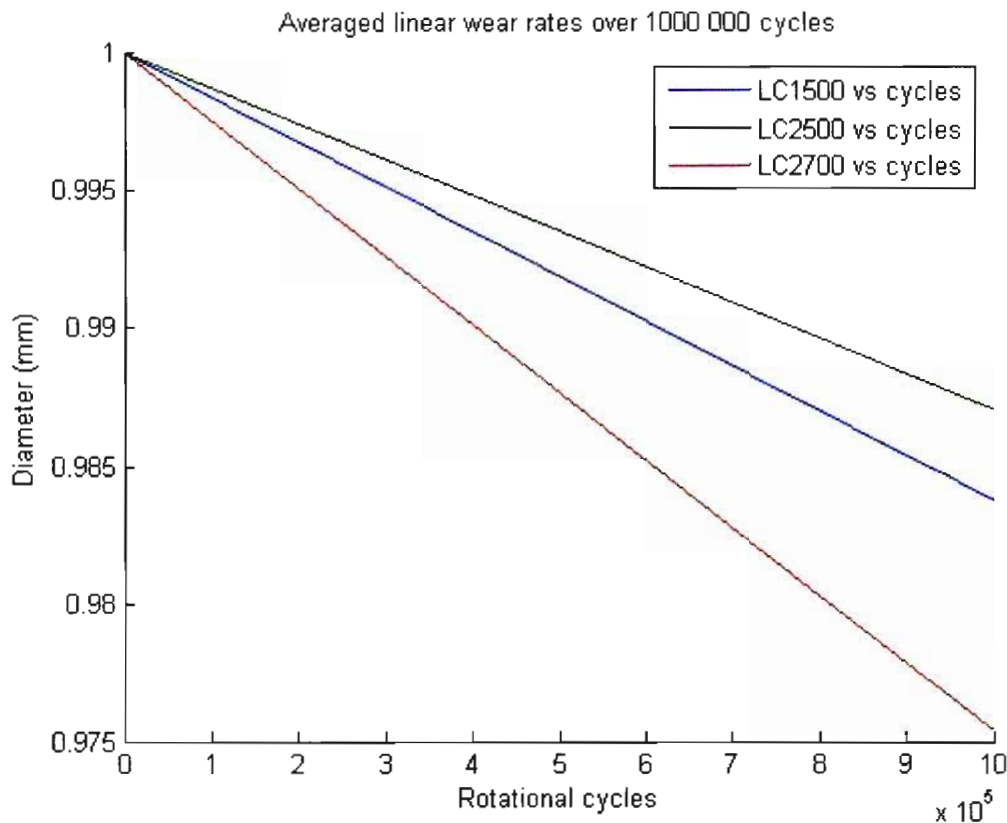
Figure 10. 26 Combined graph of wear rates for laser clad specimens

Two tested specimens were coated with the same composition (LC2500, LC2700) but tested at different contact stresses (500 and 700 MPa respectively). It is noted that the rate of wear for specimen LC2700 is significantly larger. This is an indication that microscopic fatigue was the mechanism of surface wear as a larger wear rate was measured for the specimen tested at a higher contact stress. Figure 10.24 and 10.25 represent the wear graphs for specimen LC2500 and LC2700 respectively. Figure 10.26 illustrates the combined rate of wear for three of the tested specimens. The differences in the rate of wear (Line gradient) between specimens can be observed. As the contact stress on the main rolling body is increased so are the contact stresses between the contacting asperities. The greater the contact stress the more significant the effect of fatigue on contacting asperities leading to a greater rate of wear.

It is noted that specimen LC 1500 experienced a slightly higher rate of wear than specimen LC2500, while both test specimens were tested under the same Hertz contact stress of 500 MPa. The slight difference in wear rate may have been a result of the difference in hardness value obtained for the two separate powder compositions. Specimen LC2500 coated with composition 2 had a hardness value of 34 HRC, while specimen LC1500 was coated with composition 1 and had a hardness value of 30 HRC

Specimen LC1700 failed as a result of rapid coating fracture at only 34068 cycles of rotation. The fracture occurred at the interface between the coated layer and the Heat affected zone (HAZ). Figure 10.27 illustrates the fractured specimen. The failed specimen was cut in section and a closer inspection of the coating / HAZ interface was made.

Small cracks were observed to have had initiated from very small voids formed between the coating and HAZ interface. The cracks appeared to have initiated at the coating imperfection and were propagating toward the surface of contact. Figure 10.28 illustrates one such crack. It is believed that these cracks resulted in the rapid fracture of the coating surface. Imperfections in laser clad coatings are described in Chapter 8.2.2.

Once a fatigue crack has initiated at an imperfection in the coating / HAZ interface, the crack would propagate due to the cyclic stresses at the surface and subsurface. A discussion of the subsurface stresses is presented in Chapter 6.2 while microscopic fatigue is discussed in Chapter 7.3.

Specimens LC1500 and LC1700 were coated using the same powder composition and cladding process parameters. The resulting coatings would be identical in nature both in characteristics and possible imperfections. Therefore for the tested condition, the maximum Hertz contact stress at which only surface wear (microscopic fatigue wear) would occur falls between 500MPa and 700MPa. This is due to the fact that wear was observed for the specimen tested at 500MPa and macroscopic fatigue resulted in the failure (fracture) of the coating at 700MPa

In addition for laser coating composition 1 the test specimen tested at 700MPa failed before the specimen tested at 500MPa contact stress, this is inline with fatigue principles.
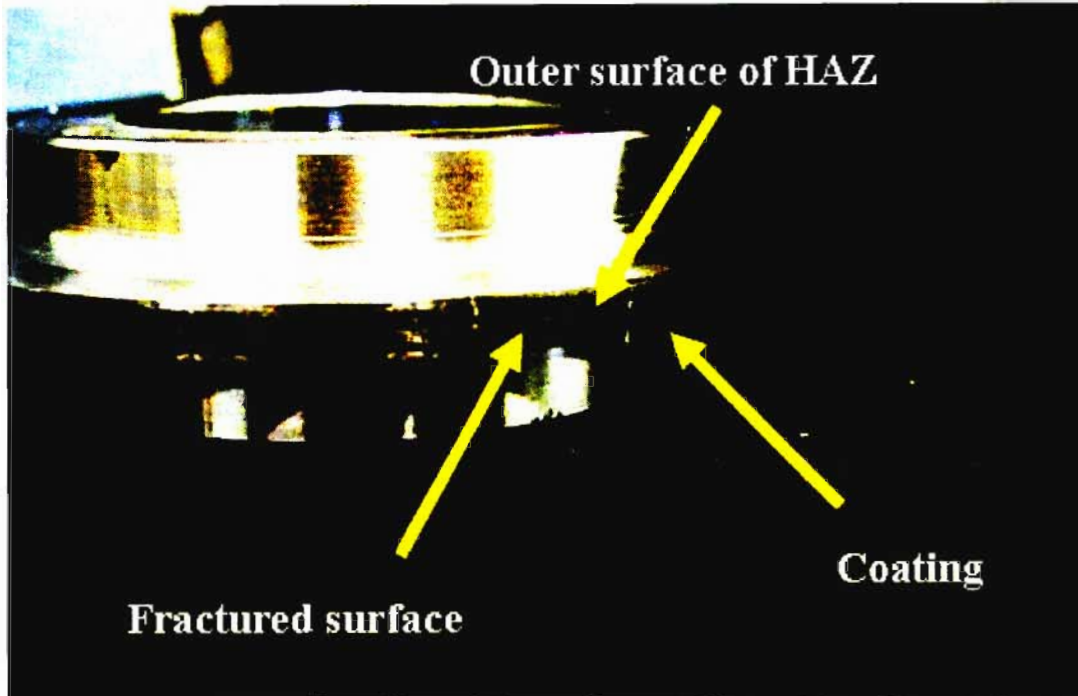
Figure 10. 27 Test specimen LC1700
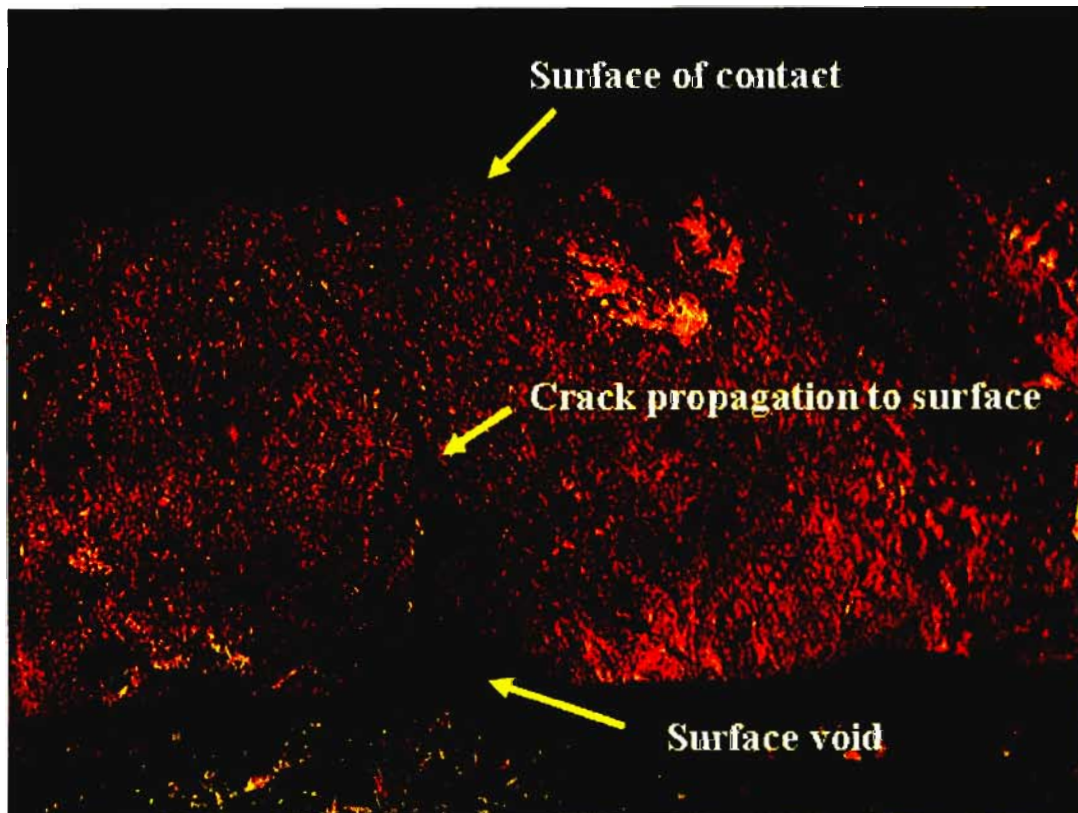
Figure 10. 28 Surface crack in coating of specimen LC1500 following testing

10.3.2 Contact width

The contact widths of the laser clad test specimens were noted to have increased following testing. The increase in contact width was a result of larger contact stresses at the edges of contact. The increase in contact stress was significant enough to allow the material at the edges to plastically deform. The same observation was noted for the En 9 test specimens following the testing. Figure 10.29 illustrates the plastic deformation at the edge of one of the laser clad specimens.
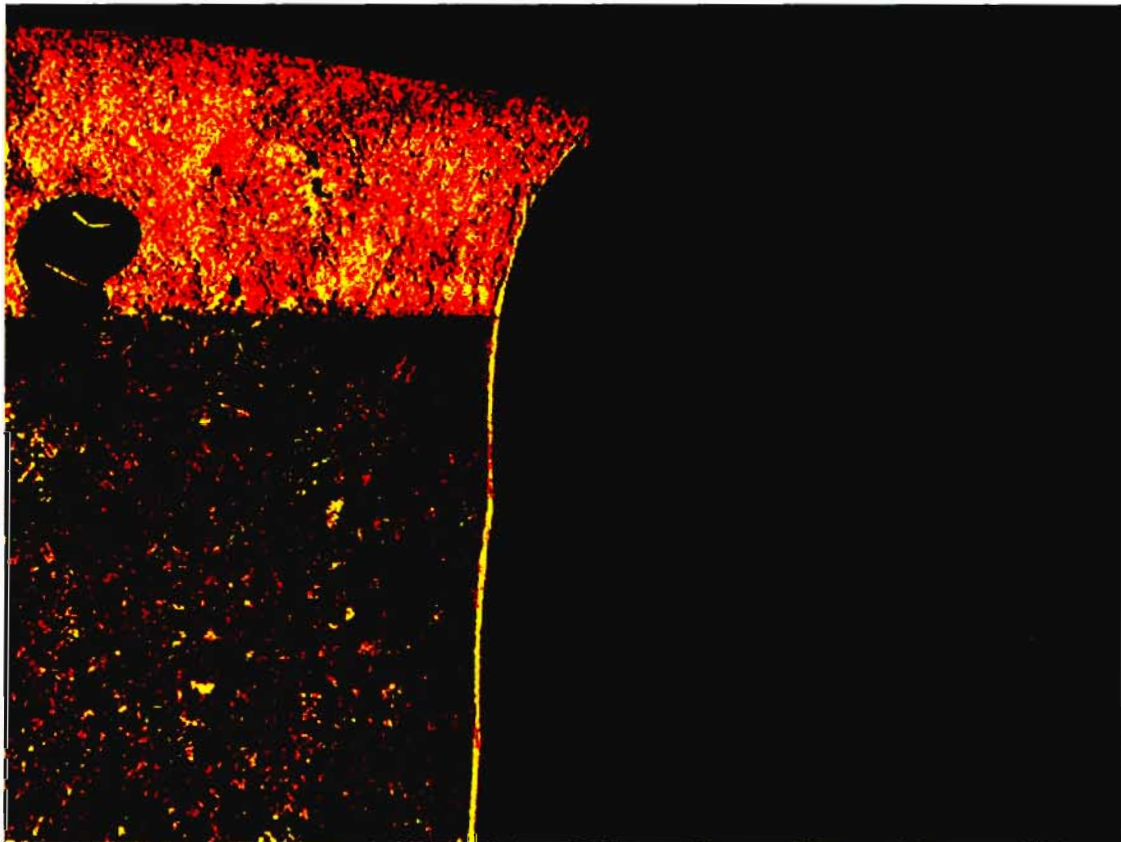
Figure 10. 29 Plastic deformation of laser clad surface

The following table illustrates the calculated increase in contact width. The top row lists the specimen identifications while the following two rows state the measured contact width prior to and following testing. The last row is the calculated percentage increase in contact width.

Table 5 Increase in contact width (Laser specimens)

	LC1500	LC1700	LC2700	LC2500
Contact width before test (mm)	9.9	5.05	5.1	9.95
Contact width after test (mm)	10.05	5.2	5.25	10.05
% increase in contact width	1.515152	2.970297	2.941176	1.005025

Comparing the increase in contact width of specimens LC1500 and LC1700 or LC2500 and LC2700 it is observed that the higher the contact stress for a given coating the greater the plastic edge deformation. This further highlights the fact that the edge deformation is a result of the quantity of applied contact stress.

It is noted that the percentage increase in contact width is greater for the two specimens coated with composition 1 than the specimens coated with composition 2. The difference is noted for any given tested contact stress i.e. comparison between LC1500 and LC2500, Both test specimens were tested at 500 MPa Hertz contact stress.

The difference may be a result of differences in mechanical properties between the two coatings. The specimens coated with composition 2 had a higher hardness value than specimens coated with composition 1. As the hardness value and ultimate tensile strength (UTS) for many metals are related, composition 2 would have a greater UTS and possibly greater yield stress than composition 1. This would mean that specimens coated with composition 1 would experience greater plastic yielding for the same applied contact stress.

11. Conclusion

The aim of the presented research was to investigate the rolling contact performance of two coating processes and two separate powder compositions applied to British standard En 9 steel. En 9 test specimens were manufactured and coated using laser and plasma coating methods. Two different powdered metal compositions were used for each of the coating processes. Rolling contact fatigue tests were performed to obtain comparative results between the coated and uncoated test specimens and between the coating compositions for a given coating process. The tests were conducted under non-lubricated 2 dimensional pure rolling contact conditions, at various Hertz contact stresses. The contact stresses under which the tests were conducted were approximately 300MPa, 500MPa, 700MPa and 900MPa. The resulting relative Hertz contact stress or load factor ratios were then 1.5, 2.5, 3.5 and 4.5 respectively. The En 9 specimens were tested within 3 deformation regimes, while the coated test specimen were tested within only 2 of the regimes.

Using equations from contract theory a program was written (m.file) to plot the complex stress distribution and magnitude of the stresses within the contact region. This was done to allow for and explanation and discussion of the contact stresses generated as a result of cylindrical contact. Under rolling contact, material elements within the contact region respond differently depending on the magnitude and position of these contact stresses. The material responses and resulting deformation regimes were explained and discussed using plots of the mathematical equations and model for the contact stresses. The contact stresses under which all the test specimens were tested were calculated using this Matlab program. Further files were also created using this software to plot the measured diameter changes of the test specimens and establish surface wear rates for the specific tested specimens.

All the rolling contact fatigue tests conducted in the present research were performed using a specifically designed and manufactured test machine. The test machine was designed with symmetry allowing for the testing of Two test specimens to be conducted simultaneously. The tests could be conducted at different stress levels due to the separate loading arm design.

The En9 benchmark test specimens were tested at all four contact stresses. The plasma specimens were tested at 300 and 500MPa while the laser specimens were tested at 500 and 700 MPa. As a result the consistent contact stress between all three sets of specimens was approximately 500MPa. During the testing of all test specimens, diameter measurements were taken to identify the rate of surface wear. Changes in specimen diameter were plotted against

the number of rolling cycles. Prior to and following testing the contact width of the test specimens were measured to observe the effect of the contact stress at the edges of contact. Table 11.1 illustrates the experimental data measured and calculated quantities for the 3 sets of specimens (Uncoated EN9, Plasma and laser) including the 2 compositions used for both laser and plasma specimens.

For all En 9 specimens tested, increases in surface hardness, contact widths and surface wear were noted to be affected by the magnitude of the contact stress for a given test.

Small increases in surface hardness were noted for all test specimens, however specimen 4 tested at 900 MPa ($Po/k = 4.5$) contact stress showed the most significant increase in surface hardness. All the test specimens experienced some degree of surface hardening; while specimen 4 tested within the ratcheting and plastic material shakedown deformation regime experienced more significant surface hardening. The observed surface hardening is in line with the theoretical material response.

The rolling contact widths of all test specimens were measured to have increased following testing. The percentage increase in contact width was more significant the greater the Hertz contact stress tested. The observation is in line with theory: the increase in contact width is a result of the stress concentration at the edges of contact. The increased stress at the edges of contact causes material to plastically deform, extruding material outwards thereby increasing the original contact width.

All the En 9 specimens experienced surface wear during the testing process. The surface wear is a result of microscopic fatigue wear acting on surface asperities. The surface asperities are a result of the specimen's surface roughness. The specimens tested at higher contact stresses experienced a greater rate of wear, this is an indication that the effect of fatigue of the contacting asperities is increased with increased contact stress, again this is in line with general fatigue theory and a further indication that surface wear was a result of fatigue and not other wear mechanisms such as adhesion or abrasion. No cracks were noted to have initiated at the end of the 1000 000 cycles of testing, indicating that macroscopic fatigue did not play a significant role in either surface failure or wear.

Figure 11.1 Experimental results

	En 9 (Benchmark)				Plasma coating				Laser cladding			
Specimen reference	1	2	3	4	PC1500	PC1300	PC2500	PC2300	LC1500	LC1700	LC2700	LC2500
Specimen diameter before coating	99.939	99.916	99.927	99.893	99.968	100.022	100.004	100.022	99.986	99.991	99.981	99.999
Specimen diameter after grinding	~	~	~	~	100.158	100.209	100.196	100.222	100.3508	100.381	100.3748	100.373
Hardness value before testing	95 HRB	95 HRB	95 HRB	95 HRB	~	~	~	~	30HRC	30HRC	34HRC	34HRC
Hardness value following testing	96 HRB	96 HRB	96 HRB	100 HRB	~	~	~	~	30HRC	30HRC	34HRC	34HRC
Coating thickness	~	~	~	~	0.095	0.0935	0.096	0.1	0.182	0.195	0.197	0.187
Number of cycles completed	999793	976457	999573	5024	~	~	~	~	1000643	34068	1001051	1000390
Number of cycles to failure	~	~	~	~	28485	314146	51784	74122	~	~	~	~
Diameter of test specimen after test	99.893	99.813	99.781	~	~	~	~	~	100.3331	N/A	100.35	100.3594
Change in diameter	0.046	0.103	0.146	~	~	~	~	~	0.01773	~	0.0248	0.01357
Contact width before test	10.05	10	5.05	4.95	10.1	10.15	10.05	10.15	9.9	5.05	5.1	9.95
Contact width after test	10.3	10.4	5.5	5.7	N/A	N/A	N/A	N/A	10.05	5.2	5.25	10.05
% increase in contact width	2.487562	4	8.910891	15.15152	N/A	N/A	N/A	N/A	1.515152	2.970297	2.941176	1.005025
Hertz Contact stress (Po)	304	508	706	918.00	505	303	507	303	506	710	710	506
Half the contact length (a) (mm)	2.12E-04	3.54E-04	4.92E-04	6.40E-04	3.52E-04	2.11E-04	3.53E-04	2.11E-04	3.53E-04	4.95E-04	3.53E-04	4.95E-04
Type of surface failure	Wear	Wear	Wear	Wear	Fatigue	Fatigue	Fatigue	Fatigue	Wear	Fatigue	Wear	Wear

~   Not applicable for test specimen

N/A   Measurement not taken as the coating was removed from the surface

All the tested plasma coated specimens coatings failed as a result of delamination. The delamination occurred at the interface between the coating and substrate; and occurred at the edges of contact where the contact stress was increased due to the stress concentration. The increased stress resulted in interfacial fatigue between coating and substrate. Fatigue is believed to be the failure mechanism for three reasons. Firstly, the coating at the edges of contact did not delaminate immediately at the commencement of testing. Secondly, failure occurred at the position of maximum contact stress. Thirdly, the specimens tested at 500 MPa contact stress (PC1500 and PC2500) experienced slightly more rolling cycles before delamiation occurred when compared to the same specimen compositions tested at 700 MPa (PC1700 and PC2700). As general fatigue theory states that the greater the stress the shorter the life to failure in fatigue this is a further indication that the fatigue mechanism resulted in the delamination between coating and substrate.

No significant differences were noted in the number of rolling cycles to failure for either of the compositions used in the plasma coatings process. The delamination as a result of fatigue was affected by the bonding mechanism (Mechanical bond) of the plasma coating process and not the differences in chemical composition of the powder used for the coating or the structure of the coating.

An increase in contact width and surface wear for the laser clad test specimens was noted, both measured quantities increased with increased contact stress. The predominant mechanism of coating failure was surface wear, however one specimen (LC1700) did fail as a result of fracture, cracks propagated from imperfections between the coating and substrate resulted in final fracture. No changes to the surface hardness of the laser clad test specimens were noted following testing. The change in diameter or overall wear was measured to be less for the specimen coated with composition 2 (LC2500) then with composition 1 (LC1500) tested at 500 MPa contact stress. The surface wear mechanism is believed to be microscopic fatigue. In comparing the two test specimens coated using composition 2 (LC2700 and LC2500) the specimen tested at the higher contact stress (LC2500) experienced greater wear and wear rate.

The effect of the increase in contact stress affected all the tested specimens coated and uncoated. Many of the coating failures were as a result of the increased contact stress at the edges of the test specimen. The result of the increased contact stress had the effect of increasing the effect of fatigue at the edges of the test specimens. The increased contact stress caused the rolling contact width to increase for both the laser and benchmark specimens, while the edges of contact for the plasma coated specimens experienced delamination.

The plasma coatings proved to be ineffective under the tested conditions when compared with either the benchmark or the laser clad specimens. The specimens delaminated very early on in the testing process due the increase in stress at the edges of contact. The life of the plasma coating may be increased if the stress concentration is reduced by changing the edge contact geometry (rounding or filleting the edges). Plasma coating may prove to be more effective under applications where the contact stresses are lower than the tested values. A possible reason for the better rolling contact performance of the laser coated test specimens over the plasma coated specimens is the bonding mechanism. Laser clad coatings obtain a metallurgical bond while plasma spraying results in a mechanical bond between coating and substrate.

Laser cladding offers greater wear resistance compared to the benchmark En 9 specimens for the same tested contact stress. This is possibly due to the higher surface hardness of the laser clad coatings.

The differences in the wear rates of the En 9 specimens are also greater then the laser clad specimens overall. The slope of the wear graph is much steeper than that of the laser clad samples indicating a greater loss of material for a given number of rolling contact cycles.

For the laser coated specimens, the test specimens coated using composition 2 were measured to have a higher hardness value than the specimens coated with composition 1. The laser cladding process parameters were the same for all clad specimens.

Specimens coated with composition 2 showed less overall wear (change in diameter) than specimens coated with composition 1. Specimens coated with composition 2, showed visible porosity after coating compared to specimens coated with composition 1. However, composition 2 showed the lower wear rate and both specimens lasted for the full test period of approximately 1000 000 cycles. The visible porosity of the specimens coated using composition 2 may be able to be illuminated by adjusting the process parameters in further research in the laser cladding process.

It can therefore be concluded that laser cladding is a good surface modification process for En9 under rolling contact, while composition 2 offers the greater wear resistance of the two compositions used.

12. References

1.   A. P. Boresi & O. M Sidebottom *Advanced mechanics of materials 4th edition*, John Wiley & Sons, Inc (1985) pg 37,134,693,695,716,718,720

2.   H. Fessler, E. Ollerton, *Contact stresses in toroids under radial loads,* British Journal of Applied Physics (1957) pg 387, 392

3.   J.W. Harris, H. Stocker, *Handbook of mathematics and computational science*, Springer-Verlag New York, pg 93

4.   J.J Kalker, *Wheel rail rolling contact theory*, Wear 144 (1991) pg 243, 245

5.   J.A. Greenwood, *Analysis of elliptical Hertzian contacts,* Tribology International (1997) Vol. 30. No. 3 235-237. pg 236

6.   M. Pau, F. Aymerich, F. Ginesu, *Distribution of contact pressure in wheel-rail contact area,* Wear 253 (2002) pg 265,271,273,

7.   M.B. Marshall, R. Lewis, R.S. Dwyer-Joyce, O. Olofsson, *Measuring wheel/rail contact stresses using ultrasound,* Paper from the 14th International Wheelset Congress. 7 pg 23

8.   A. Kapoor, F. Franklin, S. Wong, M. Ishida, *Surface roughness and plastic flow in rail wheel contact,* Wear 253 (2002) pg 257.

9.   K.L Johnson, *Contact Mechanics*, Cambridge University Press (1985) pg 90,91,99,100,102,132,133,154,284,285,288,189

10.   R.C. Juvinall, *Fundamentals of machine design 3rd edition*, John Wiley & Sons, Inc (2000) pg 246.

11.   M. Sraml, J. Flasker, I. Potrc, *Numerical procedure for predicting the rolling contact fatigue crack initiation,* International journal of fatigue 25 (2003) 585-595. pg 587

12.   W.J Palm , *Introduction to Matlab 6 for engineers*, McGraw-Hill International (2001) pg 229

13.   R.D. Arnrel, P.B. Davis, J. Halling, T.L. Whomes, *Tribology: Principles and design applications*, MacMillian Education Ltd. (1991) pg 13,73,74

14.   W.R Tyfour, J.H Beynon, A Kapoor, *The steady state wear behaviour of pearlitic rail steel under dry rolling-sliding contact conditions,* Wear 180 (1995) pg 85,.

15.   B. Xu, Y. Jiang, *Elastic-Plastic finite element analysis of partial slip rolling contact,* Journal of Tribology (2002) pg 20,21

16.   J.R. Berber, M. Ciavarella, *Contact mechanics,* International Journal of Solids and Structures 37 (2000) 29-43. pg 31

17. J. Halling, *Principles of Tribology,* The Macmillan press Ltd. (1975), pg 52,53,94,178,179,184-190

18. A.Nakajimi, T. Mawatari, M. Yoshida, K. Tani, A. Nakahira, *Effects of coating thickness and slip ratio on durability of thermally sprayed WC cermet coating in rolling/sliding contact.* Wear 241 (2000) pg 172,167

19. Y. Jiang, B. Xu, H. Sehitoglu, *Three-dimensional elastic-plastic stress analysis of rolling contact,* Journal of Tribology (2002) pg 699,704

20. R.C. Hibbeler, *Engineering Mechanics 4th edition,* Macmillan publishing company, (1983) pg 440.

21. V. Bhargava, G. T Hahn, C.A. Rubin, *An elastic-plastic finite element model of rolling contact Part 1: Analysis of single contacts ,* Journal of Applied Mechanics Vol. 52 (1985) pg 67

22. A.D Hearle, K.L Johnson, *Cumulative plastic flow in rolling and sliding line contact,* Journal of applied Mechanics vol. 54 (1987) pg 1,2,3

23. Y. Jiang, H. Sehitoglu, *An analytical approach to elastic plastic stress analysis of rolling contact,* Journal of Tribology Vol. 116 (1994) pg 584, 586, 585

24. Y. Jiang, H. Sehitoglu, *Rolling contact stress analysis with the application of a new plasticity model,* Wear 191 (1996) pg 39

25. Y. Jiang, H. Sehitoglu, *Modeling of cyclic ratcheting plasticity ,Part 1: Development of constitutive relations,* Journal of Applied Mechanics Vol. 63 (1996) pg 720,722

26. Y. Jiang, H. Sehitoglu, *Modeling of cyclic ratcheting plasticity ,Part 2: Comparison of model simulations with experiments,* Journal of Applied Mechanics Vol. 63 (1996) pg 720-725

27. W.R Tyfour, J.H Beynon, A Kapoor, *Deterioration of rolling contact fatigue life of pearlitic rail steel due to dry-wet rolling-sliding line contact,* Wear 197 (1996) pg 255,256

28. V. Bhargava, G. T Hahn, C.A. Rubin, *An elastic-plastic finite element model of rolling contact Part2:Analysis of repeated contacts,* Journal of Applied Mechanics Vol. 52 (1985) pg 81

29. X. Su, P. Clayton, *Ratchetting strain experiments with a pearlitic steel under rolling/sliding contact,* Wear 205 (1997) pg 137, 141

30. P.P Benham, R.J Crawford, *Mechanics of engineering materials,* John Wiley & sons (1987)

31. J.A Collins, *Failure of materials in mechanical design, Analysis, Prediction, Prevention 2nd edition,* John Wiley & Sons, Inc (1993) pg 31,144,145,151 612,618,610,611,616

32. J. W. Ringsberg, M. Loo-Morrey, B. L. Josefson, A. Kapoor, J. H. Beynon, *Prediction of fatigue crack initiation for rolling contact fatigue,* International journal of fatigue 22 (2000) pg 209

33. R. Amed, M. Hadfield, *Failure modes of plasma sprayed WC-15% Co coated rolling elements,* Wear 230 (1999) pg 41,50,51,54

34. R. Ahmed, *Contact fatigue failure modes of HVOF coatings,* Wear 253 (2002) pg 475, 479, 480, 484, 465

35. R. Nieinen, P. Vuoristo, K. Niemi, G. Barbezat, *Rolling contact fatigue failure mechanisms in plasma and HVOF sprayed WC-Co coatings,* Wear 212 (1997) 66-77 pg 67, 68

36. B.Y Sarma, M.M. Mayuram, *Some studies on the life prediction of thermal sprayed coatings under rolling contact conditions,* Journal of Tribology July (2000), vol. 122 pg 504, 506

37. H.Gao, C. Chiu, J. Lee, *Elastic contact versus indentation modeling of multi-layered materials,* International Journal of Solids and Structures Vol. 29, No. 20 (1992) pg 2473

38. J. W. Ringsberg, *Life prediction of contact fatigue crack initiation,* International Journal of Fatigue 23 (2003) pg 575-586.

39. Y. Jiang, H. Sehitoglu, *A model for rolling contact failure,* Wear 224 (1999) pg 41.

40. T.E. Tallian, *Simplified contact fatigue life prediction model- Part 1: Review of published models,* Journal of Tribology Vol. 114 (1992) pg 207

41. T.E. Tallian, *Simplified contact fatigue life prediction model- Part 2: New model,* Journal of Tribology Vol. 114 (1992) pg 214

42. P. Clayton, X. Su, *Surface initiated fatigue of pearlitic and bainitic steels under water lubricated rolling/ sliding contact,* Wear 200 (1996) pg 67, 70

43. L. Afferrante, M. Ciavarella, G. Demelio, *A re-examination of rolling contact fatigue experiments by Clayton and Su with suggestions for surface durability calculations,* Wear 256 (2004) pg 329

44. J. Neubrand, H. Weiss,*Dry rolling wear of different materials induced by a non-uniform hertzian pressure distribution,* Surface and Coating technology 76-77 (1995) pg 462, 466

45. P.Clayton, N. Jin, *Unlubricated sliding and rolling/sliding wear behaviour of continuous cooled, Low/medium carbon bainitic steels,* Wear 200 (1996) pg 74, 80

46. Q.Y. Liu, RZ. Zhou, *Effect of tangential force on the wear behavior of steels in reciprocating rolling and rolling-sliding contact,* Wear 250 (2001) pg 357,360.

47. R. Amed, M. Hadfield, *Rolling contact fatigue behaviour of thermally sprayed rolling elements,* Surface coating technology 82 (1996) pg 176

48. J. Halling, *Introduction to tribology,* The wykeham engineering and technology series. (1976) pg 68,76

49. D. F Moore, *Principles and Applications of Tribology,* Pergamon Press Ltd (1975) pg 185,186,319

50. K. L. Johnson, *Mechanics of adhesion,* Tribology International (1998) vol. 31, No. 8 pg 413-418

51. A. Giannakopoulos, T. Venkatesh, T. Lindey, S. Suresh, *The role of adhesion in contact fatigue,* Acta mater. (1999) Vol. 47 No. 18 pg 4653-4664.

52. Y.Kimura, M. Sekizawa, A. Nitanai,*Wear and fatigue in rolling contact*, Wear 253 (2002) pg 9,10,16

53. M. Ciavarella, F. Monno, G. Demelio, *On the Dang Van fatigue limit in rolling contact fatigue,* International Journal of Fatigue (2006) pg 1-12 *Article in press.*

54. G. Donzella, M. Faccoli, A. Ghidini, A. Mazzu, *The competitive role of wear and RCF in rail steels*, Engineering fracture mechanics 72 (2005) pg 287, 298

55. Theodore Baumeister, *Marks' Mechanical engineers handbook 6th edition*, McGraw-Hill Book company, Inc (1958) pg 5-10

56. Ev.A. Shur, N.Ya Bychkova, S.M. Trushevsky, *Physical metallurgy aspects of rolling contact fatigue of rail steels,* Wear 258 (2005) pg 1169, 1170.

57. M. ueda, K. Uchino, A. Kobayashi, *Effect of carbon content on the wear property in pearlitic steels*, Wear 253 (2002) pg112

58. S. Stewart R. Ahmed, *Rolling contact fatigue of surface coatings-a review,* Wear 253 (2002) pg 108,109.

59. Sulzer Metco: www.sulzermetco.com

   http://www.sulzermetco.com/en/desktopdefault.aspx/tabid-1741//3381_read-5289/

60. R. Suryanarayanan, *Plasma spraying: Theory and Applications*, World scientific publishing co. Pty. Ltd. (1993) pg 4,197,198

61. M. Schneider, Laser cladding with powder, Doctorate of philosophy thesis, University of Twente, Enschede, The Netherlands (1998) pg 22,23,27,28,32,34,35

62. Gordonengland www.gordonengland.co.uk

   http://www.gordonengland.co.uk/tsc.htm
   http://www.gordonengland.co.uk/ps.htm

63.   Flame spray technologies www.fst.nl

       http://www.fst.nl/en/page00043.asp
       http://www.fst.nl/en/page00044.asp

64.   Air products www.airproducts.com

       http://www.airproducts.com/Products/CylinderGases/MAXX/ThermalSpraying/thermal
       spraying_techpaper.htm

65.   Swanson industries www.swansonindustries.com

       http://www.swansonindustries.com/lasercladding.php

66.   Gremada industries inc www.gremada.com

       http://www.gremada.com/lasercladding.html

67.   The Irish scientist www.irishscientist.ie

       http://www.irishscientist.ie/p91.htm

68.   J. Woolman, R.A Mottram, *The mechanical and physical properties of the
       British standard EN steels,* Vol. 1, Pergamon Press (1964) pg 129

69.   *Grinding and polishing, Metalog guide* published by *Struers* (1992) pg 23

70.   Scrooby's Laboratory services cc. Spectrographical and chemical analysis of
       materials.

Appendix

```
% Applied load on test specimen (N)
%P1= (0:1:15000)';
P1= 2815.47
%Length of contact between rollers (m)
L = 0.0051
%Load per unit length (N/m)
P= P1/L
%Piosons ratios for bodies 1 and 2
v1=0.3
v2=0.3
% Radius of curvature of Roller 1 and Roller 2
R1 = 0.050
R2 = 0.175
%Equivalent Ratius of curvature
R =((1/R1)+(1/R2)).^(-1)
% Modulas of elasticity of body 1 and 2
E1=135e9
E2=200e9
% Equilivant modulas of elasticity
E= (((1-(v1.^2))/E1)+((1-(v2.^2))/E2)).^(-1)
%Half width of contact patch in X direection
a=((4*P*R)/(pi*E)).^0.5
% Hertz contact stress
Po= ((P*E)/(pi*R)).^0.5

%Modeling of stresses in contact area
%z= (0:0.00001:708.38e-6)';
    z= 0.473350374*a
%z= (0:a/1000:2*a)';
    %z1 = z/a
    x= (0:a/1000:a)';
%x= 0
    x1 = x/a

    m=(0.5*(((((a.^2)-(x.^2)+(z.^2)).^2)+(4.*(x.^2).*(z.^2))).^0.5)+((a.^2)-(x.^2)+(z.^2)))).^0.5;
    n=(0.5*(((((a.^2)-(x.^2)+(z.^2)).^2)+(4.*(x.^2).*(z.^2))).^0.5)-((a.^2)-(x.^2)+(z.^2)))).^0.5;
    %Sx=(((Po*((m.*(1+(((z.^2)+(n.^2))./((m.^2)+(n.^2)))))-(z.*2)))./a))/-Po
```

130

```
    %Sz=(((Po*((m.*(1-(((z.^2)+(n.^2))./((m.^2)+(n.^2)))))))./a))/-Po
    SSxz=(((((m.^2)-(z.^2))./((m.^2)+(n.^2))).*n)*(Po/a))/Po
%SS= (-0.5*(Sx-Sz))

    %Sy = ((0.3)*(Sx+Sz))

    %Sp1= (0.5*(Sx+Sz))   + ( 0.5*(( ((Sx-Sz).^2) + (4*((SSxz).^2)) ).^0.5))

    %Sp2= (0.5*(Sx+Sz))   - ( 0.5*(( ((Sx-Sz).^2) + (4*((SSxz).^2)) ).^0.5))

    %Sp3= 0.3* (Sx+Sz)
%Sp3= 0
%Tresca yeild criteria

    %Tyc= Sp1-Sp2

%Von misies yeild criteria
    %VMYC= (1/6)*(((Sp1-Sp2).^2)   + ((Sp2-Sp3).^2)   + ((Sp3-Sp1).^2))

%Reduced stress criteria
%S = (Sp1 + Sp2 + Sp3)/3
%RSC = (Sp1-S)

%Shear stress
    %SS= 0.5*(Sp1-Sp2)
```

131

```
%Numer of rolling cycles
%Specimen 1 (300 Mpa, 10.05 mm, LS) [specimen 1]
cycles1 = [0 30560 61046 100000 207677 310777 398252 506738 607002 709051 814829 920602 999793],
Diameter1 = [99.939 99.938 99.935 99.933 99.92931 99.916 99.912 99.910 99.907 99.906 99.904 99.9 99.893],

%Number of rolling cycles
%Specimen 2 (500MPa, 10 mm, RS) [specimen 2]
cycles2 = [0 30000 61094 91116 186785 277901 373570 465070 574191 672172 775218 875348 976457],
Diameter2 = [99.916 99.906 99.899 99.898 99.881 99.889 99.881 99.861 99.837 99.842 99.827 99.807 99.813],

%Numer of rolling cycles
%Specimen 3 (710 Mpa, 5.05 mm, LS) [specimen 3]
cycles3 = [0 30432 60594 100762 202362 298567 399002 494204 588199 696757 794229 896748 999573],
Diameter3 = [99.927 99.887 99.869 99.8567 99.8393 99.8413 99.842 99.837 99.814 99.807 99.795 99.792 99.781],

%Benchmark En 9 test specimens
cycles = [1:100:1000000],
%Graph for specimen 1 (300MPa)
y1 = - 4.3604e-8*cycles +1
y2 = - 1.0728e-7*cycles +1
y3 = - 1.1017e-7*cycles +1
```

132

```
%Numer of rolling cycles (Laser coating)
%Specimen 56 (LC1500) (500 Mpa, 10 mm, LS)(Composition 1)
cyclesLC1500 = [0 101253 203153 303918 404858 519760 631496 721988 826420 923450 1000643  ],
DiameterLC1500 = [100.350875 100.34558 100.34675 100.34492 100.3425 100.340818 100.33933 100.337133 100.3375 100.33406 100.33307
],

%Numer of rolling cycles (Laser coating)
%Specimen 45 (LC2500)(500 Mpa, 10 mm, LS) (composition 2)
cyclesLC2500 = [0 31368 105557 219860 321846 450895 556755 660678 764765 875369 1000390 ],
DiameterLC2500 = [100.3733 100.3715 100.3712 100.3699 100.3671 100.36656 100.364 100.3632 100.362785 100.362 100.35943 ],

%Numer of rolling cycles (Laser coating)
%Specimen 47 (LC2700) (700 Mpa, 5 mm, LS)(Composition 2)
cyclesLC2700 = [0 31556 106209 221214 323839 453705 560230 664811 769549 876030 1001051 ],
DiameterLC2700 = [100.3748 100.3713 100.369133 100.3652 100.36315 100.36012 100.357 100.354666 100.3515 100.351 100.350],

%Benchmark En 9 test specimens
cycles = [1:100:1000000],
%Graph for specimen 1 (300MPa)
LC1500= - 1.6168e-8*cycles +1
LC2500= - 1.2925e-8*cycles +1
LC2700= - 2.4554e-8*cycles +1
```